



저작자표시-비영리-변경금지 2.0 대한민국

이용자는 아래의 조건을 따르는 경우에 한하여 자유롭게

- 이 저작물을 복제, 배포, 전송, 전시, 공연 및 방송할 수 있습니다.

다음과 같은 조건을 따라야 합니다:



저작자표시. 귀하는 원저작자를 표시하여야 합니다.



비영리. 귀하는 이 저작물을 영리 목적으로 이용할 수 없습니다.



변경금지. 귀하는 이 저작물을 개작, 변형 또는 가공할 수 없습니다.

- 귀하는, 이 저작물의 재이용이나 배포의 경우, 이 저작물에 적용된 이용허락조건을 명확하게 나타내어야 합니다.
- 저작권자로부터 별도의 허가를 받으면 이러한 조건들은 적용되지 않습니다.

저작권법에 따른 이용자의 권리는 위의 내용에 의하여 영향을 받지 않습니다.

이것은 [이용허락규약\(Legal Code\)](#)을 이해하기 쉽게 요약한 것입니다.

[Disclaimer](#)

공학박사 학위논문

Designed Synthesis of Carbon- Based Nanocomposites for Li-Ion Batteries

리튬이온이차전지용
탄소 나노복합재료의 제조

2014년 8월

서울대학교 융합과학기술대학원

나노융합학과

장 병 철

Designed Synthesis of Carbon-Based Nanocomposites for Li-Ion Batteries

지도 교수 박 원 철

이 논문을 공학박사 학위논문으로 제출함
2014년 4월

서울대학교 융합과학기술대학원
나노융합학과
장 병 철

장병철의 공학박사 학위논문을 인준함
2014년 6월

위 원 장 _____ (인)

부위원장 _____ (인)

위 원 _____ (인)

위 원 _____ (인)

위 원 _____ (인)

Abstract

Designed Synthesis of Carbon-Based Nanocomposites for Li-Ion Batteries

Byungchul Jang

Department of Nano Science and Technology

Graduate School of Convergence Science & Technology

Seoul National University

Over the past decade, the control of elemental composition, size and shape of nanostructures has been major research topic in chemistry of nanostructures. Various designed synthetic methods of carbon-based nanocomposites have been investigated for electrochemical applications including batteries, fuel cells and supercapacitors. These carbon-based nanocomposites have been widely used as electrode materials due to their low cost, wide potential window, good electrical conductivity, high

electrochemical stability, and electrocatalytic activity. Recently, carbon-based nanocomposites with graphene, metal, and metal oxide, have been extensively investigated in order to further improve the intrinsic electrochemical properties.

In this work, facile synthetic methods for carbon-based nanocomposites and their electrochemical application for Li-ion battery anode were reported. Firstly, a new and simple synthetic method of hollow carbon nanospheres was introduced. Monodispersed silica nanoparticles were used as templates and various metallic surfactants were used as carbon sources. Different shaped carbonaceous nanomaterials were obtained through the carbonization of metallic surfactant precursors. Next, two dimensional (2-D) nanomaterials composed of highly monodisperse metal oxide nanoparticles and carbon were synthesized via simple heat treatment process using salt powder as template. Metal oleate complex was used as the precursor for both metal oxide and carbon. Lastly, a metal-oxide/graphene nanocomposite was directly obtained by heat treatment of a mixture of metal-oleate and graphene. The generated metal oxide nanoparticles were homogeneously embedded in the graphene layers, and they acted as mutual spacers in the nanocomposite to prevent the restacking of the graphene layers and the

aggregation of nanoparticles.

These carbon-based nanocomposites were shown to be excellent anode materials for Li-ion batteries with high capacity, good rate performance and stable durability.

Keywords: Carbonaceous nanomaterials, metal oxide nanoparticles, Graphene, nanocomposites, Li-ion battery anode

Student Number: 2010-31263

Contents

Chapter 1. Introduction: Carbon-Based Nanomaterials for Li-Ion Batteries and Dissertation Overview

1.1. Introduction.....	25
1.2. Carbonaceous Nanomaterials for Electrode in Electrochemical Applications	29
1.2.1. Graphitic Carbons: graphene	32
1.2.2. Amorphous Carbons	34
1.2.3. Carbon-Based Nanocomposites.....	37
1.2.4. Various Methods for the Fabrication of Carbon-Based Nanocomposites	38
1.3. Application of Nanomaterials for Li-Ion Batteries	43
1.3.1. Li-Ion Batteries	43
1.3.2. Anode Materials for Li-Ion Batteries	50
1.3.2.1. Insertion reaction mechanism: graphite and titanium oxide.....	53
1.3.2.2. Alloying reaction mechanism: tin and silicon.....	57
1.3.2.3. Conversion reaction mechanism: transition metal	

oxide.....	61
1.3.2.4. Carbon based metal or metal oxide nanocomposites.....	64
1.4. Dissertation Overview	68
1.5. References	70

Chapter 2. Thin-Layered Hollow Carbon Nanostructures by the Direct Pyrolysis of Surfactants

2.1. Introduction.....	78
2.2. Experimental Section.....	79
2.2.1. Chemicals	79
2.2.2. Characterization methods	79
2.2.3. Preparation of SDS coated PS nanoparticle solutions.	80
2.2.4. Preparation of SDS coated SiO ₂ nanoparticle solutions	80
2.2.5. Synthesis of HCNS using SDS-coated template nanoparticles.....	80
2.2.6. Synthesis of thin layered carbon materials using non- metallic surfactants.....	81
2.2.7. Heat treatment experiments of metallic surfactants	82

2.3. Results and Discussion	84
2.4. Conclusion	100
2.5. References	102

Chapter 3. Self-assembled Ferrite/Carbon Hybrid Nanosheets for Lithium-Ion Battery Anodes

3.1. Introduction.....	106
3.2. Experimental Section.....	110
3.2.1. Chemicals	110
3.2.2. Characterization methods	110
3.2.3. Preparation of 16-nm iron-oxide/carbon hybrid nanosheets	110
3.2.4. Preparation of 30-nm iron-oxide/carbon nanosheets	111
3.2.5. Preparation of 3-D nanocomposites	111
3.2.6. Preparation of 10-nm manganese-ferrite/carbon nanosheets	112
3.2.7. Preparation of electrodes for LIBs	112
3.3. Results and Discussion	115
3.4. Conclusion	144
3.5. References	145

Chapter 4. γ -Fe₂O₃/Graphene Nanocomposite for Lithium-Ion Battery Anodes

4.1. Introduction.....	151
4.2. Experimental Section.....	154
4.2.1. Chemicals	154
4.2.2. Characterization methods	154
4.2.3. Preparation of graphene	154
4.2.4. Preparation of iron-oxide nanoparticles/graphene composite	155
4.2.5. Preparation of iron-oxide nanoparticles	155
4.2.6. Preparation of electrodes for LIBs	155
4.3. Results and Discussion	158
4.4. Conclusion	172
4.5. References	173

Chapter 5. Conclusion and Future Works

5.1. Conclusion	179
5.2. Future Works	181
5.3. References	184

Bibliography 185

국문 초록 (Abstract in Korean) 195

List of Figures

- Figure 1.1.** Alternative energy sources and their conversion and storage devices. 27
- Figure 1.2.** Various allotropes of carbon. 31
- Figure 1.3.** Preparation of various carbon nanostructures via template method. (from Ref. 32. Hyeon et al., *Adv. Mater.* **2006**, 18, 2073.)..... 36
- Figure 1.4.** Schematic illustration of the procedure for the synthesis of uniform and water-dispersible iron oxide nanocapsules. (from Ref. 46. Piao et al., *Nat. Mater.* **2008**, 7, 242.)..... 40
- Figure 1.5.** Schematic illustration of mix–bake–wash (MBW) process and subsequent dextran coating. (from Ref. 47. Hyeon et al., *J. Mater. Chem.* **2011**, 21, 11472.)..... 41
- Figure 1.6.** Energy density of various secondary batteries (Volumetric

energy density vs. gravimetric energy density). (from Ref. 1. Winter et al., *Chem. Rev.* **2004**, 104, 4245.)..... 44

Figure 1.7. Schematic representation of Li-ion battery. Anode (graphite), electrolyte, and cathode (LiCoO₂). (from Ref. 55. Etacheri et al., *Energy Environ. Sci.* **2011**, 4, 3243.) 48

Figure 1.8. Plot of reversible capacity vs. heat treatment temperature for variety carbonaceous materials. (from Ref. 57. Dahn et al., *Science* **1995**, 270, 590.) 49

Figure 1.9. Voltage vs. capacity for electrode materials in Li-ion batteries. (from Ref. 51. Tarascon et al., *Nature* **2001**, 414, 359.)..... 52

Figure 1.10. Lithium binding configurations on a metallic SWCNT (top) and a semiconducting SWCNT (bottom) at 50% and 25% lithium coverage. (from Ref. 62. Hersam et al., *ACS Nano* **2014**, 8, 2399.)..... 55

Figure 1.11. Cycle performance of $\text{Li}_4\text{Ti}_5\text{O}_{12}$ intercalation electrode at a rate of C/5. (from Ref. 63. Thackeray et al., *J. Electrochem. Soc.* **1994**, 141, L147.)..... 56

Figure 1.12. Effects of particle size during the cycling (from Ref. 65. Besenhard et al., *Electrochim. Acta* **1999**, 45, 31.)..... 58

Figure 1.13. Schematic of the fabrication process for DWSiNTs. Polymer nanofibres (green) were first made by electrospinning. The polymer fibres were then carbonized and coated with silicon (blue) using a CVD method. By heating the sample in air at 500 °C, the inner carbon templates (black) were selectively removed, leaving continuous silicon tubes with a SiO_x mechanical constraining layer (red) (from Ref. 72. Cui et al., *Nat. Nanotechnol.* **2012**, 7, 310.) 60

Figure 1.14. Schematic of the reaction mechanism for insertion and conversion reaction of anode materials (from Ref. 2. Armand et al., *Nature* **2008**, 451, 652.) 62

Figure 1.15. Cycling performance of transition metal oxide electrodes during the charge/discharge. (from Ref. 7. Tarascon et al., *Nature* **2000**, 407, 496.)..... 63

Figure 1.16. Schematic representation of the different reaction mechanisms observed in electrode materials for lithium batteries. Black circles: voids in the crystal structure, blue circles: metal, yellow circles: lithium. (from Ref. 77. Palacín et al., *Chem. Soc. Rev.* **2009**, 38, 2565.) 65

Figure 1.17. Schematic of the fabrication process for silicon pomegranates (from Ref. 78. Cui et al., *Nat. Nanotechnol.* **2014**, 9, 187.)..... 67

Figure 2.1. Schematic of the direct carbonization of surfactants by a template method. (a) Hollow carbon nanospheres from metallic surfactants and (b) hollow nanocube from non-metallic surfactants. 83

Figure 2.2. Electron microscope images of the template nanoparticles

and the carbon materials from metallic surfactants. (a) The as-synthesized SDS-coated PS, (b) SDS-coated SiO₂ nanoparticles, (c) FESEM image of HCNS from SDS-coated PS and (d) TEM image of HCNS from SDS-coated SiO₂. (Inset: High magnification image) 85

Figure 2.3. Low and high magnification TEM images of HCNS obtained from SDS-coated PS nanoparticles. 87

Figure 2.4. (a) TGA diagrams of various surfactants and (b) optical images after heat treatment. SEM images of carbon materials from pure (c) SDS and (d) SO. 89

Figure 2.5. SEM images of the carbon nanomaterials from (a and b) SO-coated PS and (c and d) SO-coated SiO₂ template. (Inset: High magnification TEM image) 90

Figure 2.6. Electron microscope images of thin layered carbon materials from (a) Oleic acid/NaCl, (b) CTAB/NaCl and (c) CTAB/Na₂SO₄. (d) Optical image of as-heat treated samples

without washing process. (Inset: High magnification TEM image). 92

Figure 2.7. Raman spectra of thin layered carbon materials from non-metallic surfactants. 93

Figure 2.8. Photo images of (a) SDS, (b) SO, (c) SDS coated PS and (d) purified PS polymer in round bottle flasks during the heat treatment from room temperature to 350 °C under N₂ atmosphere. SDS was carbonized at 240 °C, while SO and PS were melted at 350 °C..... 96

Figure 2.9. Ar isotherms (at 87 K) of the obtained nanostructured carbon materials obtained by direct carbonization of (a) SDS and (b) SO. 97

Figure 3.1. (a) Schematic representation of the preparation of ferrite/carbon nanosheets by salt-template process. (b) FESEM image and (c-d) TEM images of the 16-nm iron-oxide/carbon nanosheets. The inset shows a HRTEM image

demonstrating the highly crystalline nature of the nanosheets..... 114

Figure 3.2. SEM images of (a,b) Na₂SO₄ salt, (c) 16-nm iron oxide/carbon nanosheet on Na₂SO₄ salt, and (d) 16-nm iron oxide/carbon nanosheet after removal of sodium sulfate salt powder. 116

Figure 3.3. High magnification TEM image of the 16-nm iron-oxide/carbon nanosheet. The inset figure represents electron diffraction patterns of the 16 nm iron oxide nanoparticles..... 119

Figure 3.4. (a) FESEM image and (b) TEM image of the 30-nm iron-oxide/carbon nanosheets, (c) FESEM image and (d) TEM image of the 10-nm manganese-ferrite/carbon nanosheets. 120

Figure 3.5. TEM images of 30-nm iron-oxide/carbon nanosheet prepared at the heating rates of (a) 20 °C min⁻¹, (b) 10 °C

min⁻¹, (c) 5 °C min⁻¹, and (d) 2.5 °C min⁻¹. Annealing temperature was fixed at 600 °C. 121

Figure 3.6. Size distributions of the iron oxide nanocrystals measured on TEM images in Figure 3.5..... 122

Figure 3.7. TEM images of the iron-oxide/carbon hybrid nanosheets prepared at different annealing temperature of (a), (d) 250 °C, (b), (e) 300 °C, and (c), (f) 600 °C. Heating rate was fixed at 5 °C min⁻¹. 123

Figure 3.8. Large scale synthesis of 30-nm iron-oxide/carbon nanosheet. (a) A photograph showing ~1.3 g of the synthesized 30-nm iron-oxide/carbon nanosheet nanosheets. (b) TEM image of 30-nm iron-oxide/carbon nanosheet in large-scale..... 125

Figure 3.9. (a) Mn to Fe ratio in manganese ferrite from was determined by inductively coupled plasma auger electron spectrometry (ICP-AES). (b-e) TEM images of manganese-ferrite/carbon nanosheets synthesized using various ratios of manganese(II) and iron(III) chlorides in the oleate synthesis step. 126

Figure 3.10. XRD patterns of the ferrite/carbon hybrid nanosheets. ..	128
Figure 3.11. (a) Schematic representation of the preparation of the carbon nanofoams. (b-c) TEM images of the carbon nanofoam after removal of the 16 nm iron oxide nanocrystals from the nanosheets.....	131
Figure 3.12. (a,b) FESEM and (c,d) TEM images of 3-D nanocomposite	132
Figure 3.13. TEM images of iron-oxide/carbon composites by using (a) iron caprylate and (b) iron laurate as the precursors.	133
Figure 3.14. Raman spectrum of 30-nm iron-oxide/carbon nanosheets.....	134
Figure 3.15. Galvanostatic discharge (lithiation, downward) and charge (de-lithiation, upward) voltage profiles	139
Figure 3.16. (a) Lithiation/de-lithiation capacities, and (b) rate	

performance according to the cycle number of the ferrite/carbon nanosheet electrodes. 140

Figure 3.17. TEM images of (a, b) 16-nm iron-oxide/carbon nanosheets, and (c, d) 10-nm manganese-ferrite/carbon nanosheets after 10th charge/discharge cycling at a rate of 100 mA g⁻¹. . 143

Figure 4.1. Schematic representation of the preparation of iron-oxide/graphene nanocomposites and iron oxide nanoparticles 157

Figure 4.2. (a) XRD patterns of iron-oxide/graphene nanocomposite, iron oxide nanoparticle and graphene. (b) N₂ isotherms at 77 K and (c) XPS spectra of as-prepared graphene 160

Figure 4.3. (a) FESEM image of as-prepared graphene, (b) FESEM image and (c) TEM image of iron-oxide/graphene nanocomposite and (d) SEM image of iron oxide nanoparticle. The inset figure represents high resolution TEM image of iron oxide nanoparticle. 161

Figure 4.4. (a) Low and (b) high magnification FESEM image and (c) Low and (d) high magnification TEM image of iron-oxide/graphene nanocomposite. 162

Figure 4.5. TGA result of iron-oxide/graphene nanocomposite 163

Figure 4.6. Galvanostatic discharge (lithiation, downward) and charge (delithiation, upward) voltage profiles of (a) iron oxide nanoparticle, (b) graphene and (c) iron-oxide/graphene nanocomposite. (d) Lithiation/delithiation capacities according to the cycle number of iron-oxide/graphene nanocomposite, iron oxide nanoparticle and graphene; Efficiency of iron-oxide/graphene nanocomposite. (e) Rate performance and efficiency of iron-oxide/graphene nanocomposite. (f) AC impedance spectra (Nyquist plot) obtained with the iron oxide nanoparticle and iron-oxide/graphene nanocomposite at fully lithiation state .. 166

Figure 4.7. TEM images of iron-oxide/graphene nanocomposite after 50th charge/discharge cycling at a rate of 100 mA g^{-1} . The

inset figure represents high resolution TEM image of the pulverized iron oxide nanoparticle 171

Figure 5.1. Schematic image of SEI formation on the surface of high capacity materials including nano-sized metal or metal oxides particles. 183

List of Tables

Table 1.1. Mechanical, electrical, and optical properties of carbon allotropes	33
Table 2.1. Specific surface area and pore volume of carbon materials from metallic surfactants.	99
Table 3.1. Ferrite and carbon contents of ferrite/carbon hybrid nanosheets based on CHN analysis	135
Table 3.2. Ferrite and carbon contents of ferrite/carbon composites using (a) iron caprylate and (b) iron laurate as the precursors	136

**Chapter 1. Introduction: Carbon-Based Nanomaterials for Li-Ion
Batteries and Dissertation Overview**

1.1. Introduction

Nowadays, increasing world energy consumption is serious worldwide problem not only from the view of fossil fuels shortage but also that of environment problems. There are many alternative energy sources such as solar energy, wind energy, geothermal energy, bioenergy, and ocean energy. Since most of these alternative energy sources have less environmental impact and produce energy permanently, great attentions have been made on the development of energy conversion and storage devices such as batteries, fuel cells and supercapacitors with improved performances. As shown in Figure 1.1, the energy comes from alternative energy sources and it is converted into electrical energy by energy conversion and harvesting devices. The generated electrical energy is usually stored in the battery.

A battery is an energy storage device consisting of electrochemical cell that converts chemical energy into electric energy. This is done by the transfer of electrons from one material to another through an electric circuit. This transfer results in the oxidation of the anode and the reduction of the cathode, a process called oxidation-reduction or redox reaction. The electrolytes allow ions to move between the electrodes.

Primary batteries are used one-time and discarded because the electrode materials are irreversibly changed during discharge. The alkaline battery is used once and discarded which is used for portable devices. Rechargeable batteries are called secondary batteries, they can be recharged multiple times because the electrode materials are reversibly changed during charge/discharge. For examples, the lead-acid battery is used in vehicles and lithium ion battery is used for portable devices.

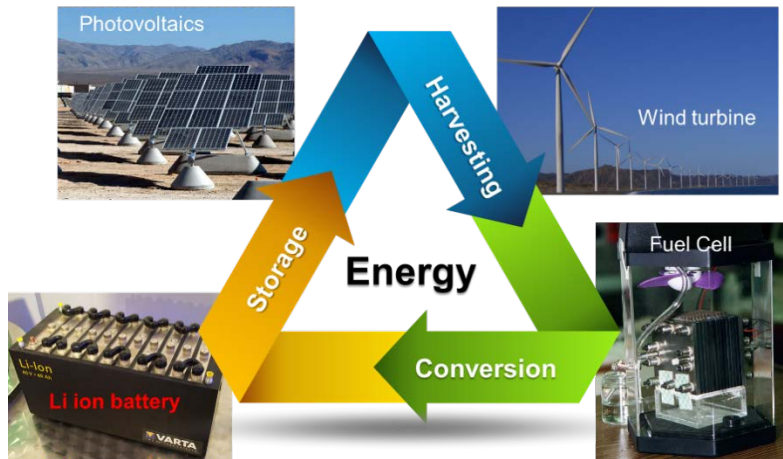


Figure 1.1. Alternative energy sources and their conversion and storage devices.

These days, rechargeable Li-ion battery (LIB) is one of the most important power sources for portable electronic devices [1–6]. LIBs are one of the most popular types of rechargeable battery for portable electronics, with high energy densities, no memory effect, and a slow charge loss when not in use. LIBs have replaced the lead acid batteries that was used for vehicles. A battery cell prefer the use of lightweight lithium and carbon electrodes instead of heavy lead plates and toxic acid electrolyte.

Recently, many critical issues have been widely discussed such as high energy density, durability, and economical efficiency in LIBs [7-10]. In order to develop new electrode materials with higher energy density and improved cycling stability for LIB, nanostructured materials including nanoparticle, nano fiber, nanotube and their composites were extensively investigated [11-14]. These nano-sized (1-100 nm) materials have the intrinsic properties than bulk materials.

In this chapter, I would like to introduce the carbonaceous nanomaterials and carbon-based nanomaterials for the electrode in LIBs. In following section, Li-ion batteries and anode materials as Li-ion batteries are introduced. And then the thesis is overviewed.

1.2. Carbonaceous nanomaterials for electrode in electrochemical applications

There are many allotropes of carbon (Figure 1.2). Graphite, diamond, and amorphous carbon are the well-known as carbon allotropes. These carbon allotropes have been widely used as electrodes due to their low cost, wide potential window, good electrical conductivity, high electrochemical stability and electrocatalytic activity [15-18].

The well-known allotropes of carbon such as graphite, diamond, and fullerenes have different electrochemical properties. Graphite is multi-layers of graphene sheet which is composed of sp^2 -bonded carbon atoms with one carbon atomic thickness with a C-C bond length of 1.42 Å and interplanar spacing of 3.354 Å. Diamond is composed of all sp^3 -bonded carbon atoms with a C-C bond length of 1.54 Å. Diamond could also be used as an electrode by doping because of the insufficient conductivity for electrochemistry. The most common fullerene is carbon nanotube which is cylindrical nanostructure of single or multi layers of graphene sheet.

Properties of the carbonaceous materials vary greatly for different forms of the allotrope (Table 1.1). For examples, graphite is opaque,

while diamond is highly transparent; graphite is soft material, while diamond is the hardest material; graphite has a good electrical conductivity, while diamond has a very low electrical conductivity. Most carbon allotropes have high thermal conductivity under normal conditions.

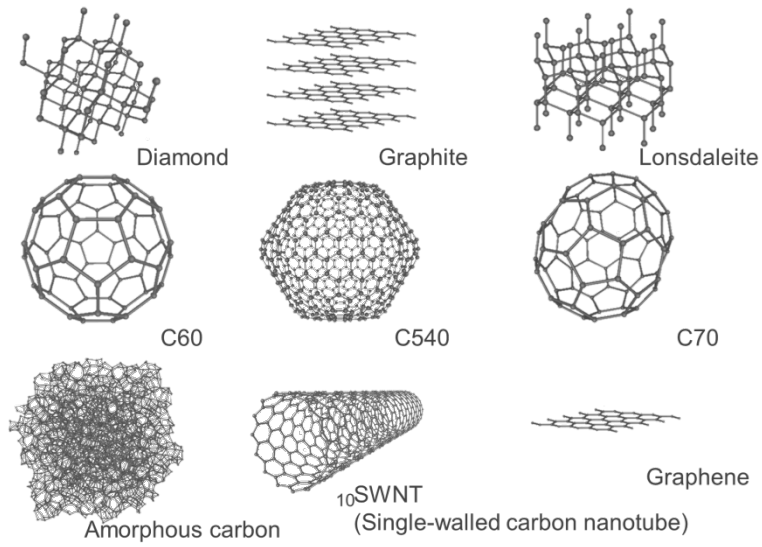


Figure 1.2. Various allotropes of carbon.

1.2.1. Graphitic carbon: graphene

Graphene is a two dimensional carbon sheet composed of sp^2 -bonded carbon atoms with one carbon atomic thickness. It is the basic building block of other allotropes including graphite, nanotubes, and fullerenes. Graphene is widely used and investigated due to its high surface area (theoretical value $2630 \text{ m}^2 \text{ g}^{-1}$), great electronic conductivity, mechanical stability, and so on. These properties make graphene very promising electrode material for batteries, supercapacitors, nanoelectronics and sensors [19-22]. Especially, as anode materials for LIBs, graphenes exhibit high capacity of $\sim 1264 \text{ mAh g}^{-1}$ at low charge/discharge rates. However, its performance is rapidly decreased during the repeated cycling at high charge/discharge rate due to their structural deformation and re-stacking to the graphite. So, the graphene based composite materials with spacer materials including polymer, carbon and inorganic nanoparticle have been reported as anode materials [23-28].

Diamond	Graphite	Graphene
sp^3 forms	sp^2 forms	sp^2 forms
Hardest materials	Softest materials	Hardest materials
Ultimate abrasive	Good lubricant	Good lubricant
Excellent electrical insulator	Excellent electrical conductor	Excellent electrical conductor
Thermal conductor	Thermal insulator	Thermal conductor
Highly transparent	Opaque	Highly transparent
Cubic crystal structure	Hexagonal crystal structure	Hexagonal crystal structure

Table 1.1. Mechanical, electrical, and optical properties of carbon allotropes.

1.2.2. Amorphous carbon

Amorphous carbon has the mixed sp^3/sp^2 -bonded carbon atoms and has no crystal structure. Amorphous carbon materials may be stabilized by π bonds with hydrogen. Glassy carbon is a non-graphitic carbon that combines the properties of ceramic and glass. The most important feature of glassy carbon is impermeability to liquid and gas, high temperature resistance, low density, low electrical resistance, low friction, low thermal resistance, good chemical resistance, and hardness. Glassy carbon is partly used for crucible and electrode, and can be fabricated as different shape and size.

Porous carbon materials are used extensively as electrode materials for batteries, fuel cells, and supercapacitors, and support materials for many important catalytic process due to their superior physical and chemical properties, such as high electric conductivity, thermal conductivity, chemical stability, and low density. Porous carbon materials can be classified according to their pore diameters as microporous (pore size < 2 nm), mesoporous (2 nm $<$ pore size < 50 nm), and macroporous (pore size > 50 nm). Porous carbon materials are usually synthesized by physical or chemical activation process or heat treatment of organic precursors [29–32]. Usually, these carbon materials

have a relatively broad pore size distribution in both micropore and mesopore ranges. Conventional porous carbon materials including activated carbon have been produced in large quantities, and are used widely in adsorption, separation, and catalysis applications.

Figure 1.3 depicts the overall concept of the template synthesis. The various porous carbon nanostructures are synthesized using various templates such as poly styrene nanoparticles, silica nanoparticles, zeolites, anodic alumina membranes, and mesoporous silica materials. Firstly, the carbon precursors are homogeneously coated on the template. And then, porous carbon nanostructures are prepared after carbonization and removal of the template.

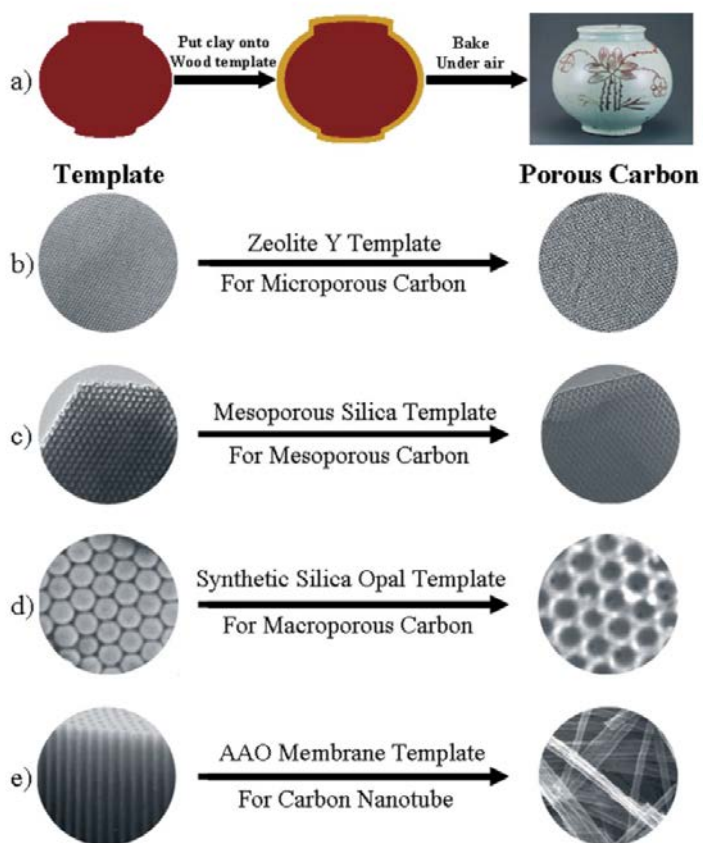


Figure 1.3. Preparation of various carbon nanostructures via template method. (from Ref. 32. Hyeon et al., *Adv. Mater.* **2006**, 18, 2073.)

1.2.3. Carbon-based nanocomposites

The electrochemical applications of nanostructured materials have attracted great research interests. For example, metal oxide nanoparticles were considered as promising candidate materials due to their high theoretical capacity ($\sim 1000 \text{ mAh g}^{-1}$) [33-35]. Also, their dimension-restricted structures give nanomaterials shorter path lengths for electron and Li ion transport, yielding higher conductivity and faster charge/discharge rates in LIBs [36-41]. However, undesirable side reactions can happen easily on their surfaces, including electrolyte degradation due to the high surface-to-volume ratio and high surface free energy of the nanoparticles. Furthermore, low electronic conductivity and high volume change of these metal oxide nanoparticles during the charge/discharge reaction were critical barriers for their LIBs applications.

Accordingly, to overcome these limits, intensive researches were made on the carbon-based nanocomposites. For example, coating a carbon layer on the surface of metal oxide nanoparticles can reduce the surface energy and side reactions on the surface of metal oxide nanoparticles. Moreover, good electrical conductivity of carbon can complement the low conductivity of metal oxide nanoparticles.

1.2.4. Various methods for the fabrication of carbon-based nanocomposites

Recently, a number of fabrication methods for the carbon-based nanocomposites with metal or metal oxide nanoparticles have been reported. It was reported that heating a mixture of metal salt and carbon precursors including sucrose led to the formation of metal-oxide/carbon nanocomposites [42,43]. In those processes, carbonization of organic precursors and the formation of metal oxide nanocrystals take place simultaneously. Although those methods are simple and reliable, the products were usually in poor quality in terms of both the uniformity and the homogeneity of the composite structure. In 2008, Zhang et al. reported on the preparation of carbon-coated iron oxide nanoparticles in good uniformity [44]. However, their synthetic procedure consisted of two sequential thermal reactions using autoclaves, which lowers its productivity compared to other single-step processes.

In the nanocomposite electrodes, the size of active materials determines the path length of the charge transport. That is, their size distribution strongly affects charge/discharge response of the electrode. Also, homogeneous composite structure is desirable for higher volumetric energy density. Unfortunately, inorganic nanocrystals are

thermally unstable due to lower melting points than their bulk counterparts [45]. During the heat treatment for carbonization, they easily fuse together loose their nanostructures. For this reason, single-step methods for the fabrication of metal oxide-carbon nanocomposites often lead to poor size uniformity of metal oxide nanoparticles, whose sizes range from tenths to hundreds of nanometers, and uneven mixture distribution of carbon and metal oxide.

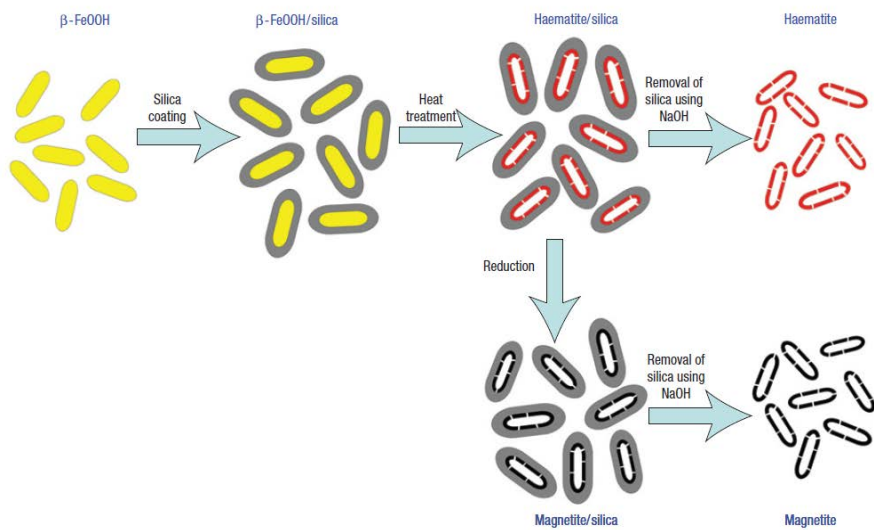


Figure 1.4. Schematic illustration of the procedure for the synthesis of uniform and water-dispersible iron oxide nanocapsules. (from Ref. 46. Piao et al., *Nat. Mater.* **2008**, 7, 242.)

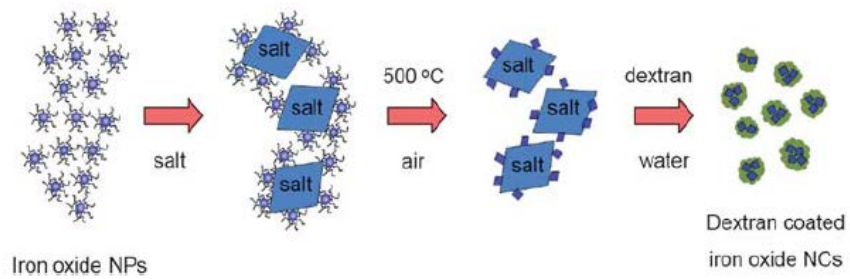


Figure 1.5. Schematic illustration of mix–bake–wash (MBW) process and subsequent dextran coating. (from Ref. 47. Hyeon et al., *J. Mater. Chem.* **2011**, 21, 11472.)

In recent years, Piao et al. have been engaged in the development of thermal treatment methods while preserving the size and shape of the nanocrystals. In 2008, a novel wrap-bake-peel (WBP) process is introduced [46]. Thermal treatment of nanomaterials generally accompany by side results such as aggregation and sintering of nanoparticles. In the WBP process (Figure 1.4), nanocrystals are coated with silica before thermal treatment, which protects the nanoparticles from deformation and aggregation. In 2011, a mix-bake-wash (MBW) process is also introduced [47]. As shown in Figure 1.5, the organic surfactants coated on the nanoparticles are removed by the MBW process without any aggregation or sintering of the nanoparticles. The nanoparticles adsorbed on the surface of salt particles are well separated from each other during the thermal treatment [48]. Liu et al. also utilized the similar process for phase transformation of FePt nanocrystals without the size change [49,50].

1.3. Application of Nanomaterials for Li-Ion Batteries

1.3.1. Li-ion batteries

Due to the rapid development of various types of mobile devices including smart phone, pad and laptop, the need to increase the energy density and specific energy of secondary battery has become more and more urgent. Li-Ion Batteries (LIBs) have been used in a wide variety of portable electronic devices due to their high energy density (Figure 1.6). LIBs have also been considered as the most promising power source for electric vehicles, including hybrid vehicles and a next generation plug-in electric vehicles [51]. Although LIBs are commercially successful, the performance of current LIBs using LiCoO_2 cathode, graphite anode, and electrolyte materials was reached the limit. The development of the new electrode materials with higher performance is essential to further improve the properties of LIBs.

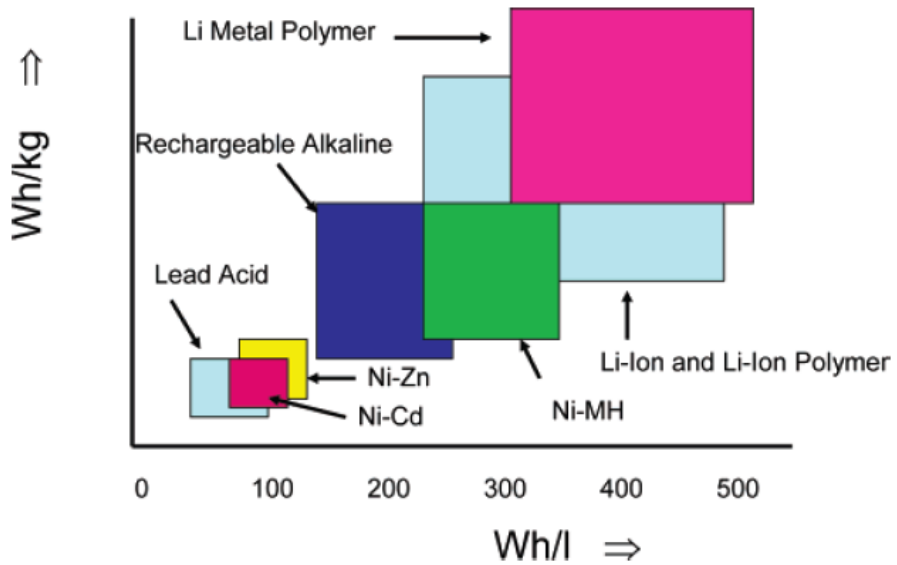


Figure 1.6. Energy density of various secondary batteries (Volumetric energy density vs. gravimetric energy density). (from Ref.1. Winter et al., *Chem. Rev.* **2004**, 104, 4245.)

The LIBs do not contain lithium metal. It is a lithium-ion device, comprising a LiCoO_2 cathode, carbon anode, and organic electrolyte of lithium hexafluorophosphate (LiPF_6) salt with ethylene carbonate-organic solvent mixture [52-54]. The fundamental physics and chemistry of the Li-ion rechargeable battery are based on a process known as “intercalation/deintercalation”; the reversible insertion of guest atoms (like lithium) into solid hosts (the battery electrode materials). The electrochemical reactions at an anode and a cathode during the charge/discharge are the following:

Anode:



Cathode:



Figure 1.7 depicts a schematic representation of Li-ion battery. Lithium ions pass across the electrolyte from the LiCoO_2 cathode to the graphite anode during charge, and vice versa during discharge. The electrons pass around the external circuit. In LIBs, the lithium ion movement between host lattices is because of an electrical oxidation-reduction reaction at the cathode and anode. There are various kinds of reactive compounds with Li^+ , which are candidate electrodes in LIBs [55,56].

First generation LIBs are composed of active materials containing micro-sized particles, and the electrolyte inside the micro-sized separator pores. Although the batteries have a high energy density, they have poor charge/discharge rate performance because of the intrinsic low diffusivity of the lithium ion in the solid electrodes. However, enhanced charge/discharge rate performance of lithium-ion batteries is required to meet the huge demands of hybrid electric vehicles and clean energy storage.

The rate of lithium reaction with electrodes during the charge/discharge have been increased by the reduced dimensions of electrode materials because of the short pathways for lithium ion transport within the particles. The diffusion time (t) is described by $t =$

L^2/D , where L is the diffusion length and D is the diffusion constant. The diffusion time of lithium during the intercalation decreases with square of the dimension size of particles. Electrons transport rate within the particles are also enhanced by the decrease the size of electrode particles. There are additional advantages using the nanoelectrodes in LIBs include improving the cycle life due to better accommodation of the strain of lithium reaction with electrodes, new possible reaction ways with electrodes, and higher reactive area leading to higher charge/discharge rates [9].

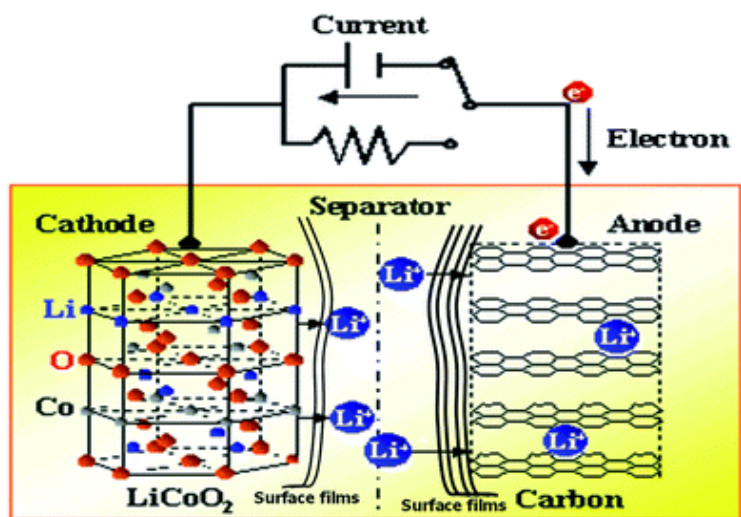


Figure 1.7. Schematic representation of Li-ion battery. Anode (graphite), electrolyte, and cathode (LiCoO₂). (from Ref. 55. Etacheri et al., *Energy Environ. Sci.* **2011**, 4, 3243.)

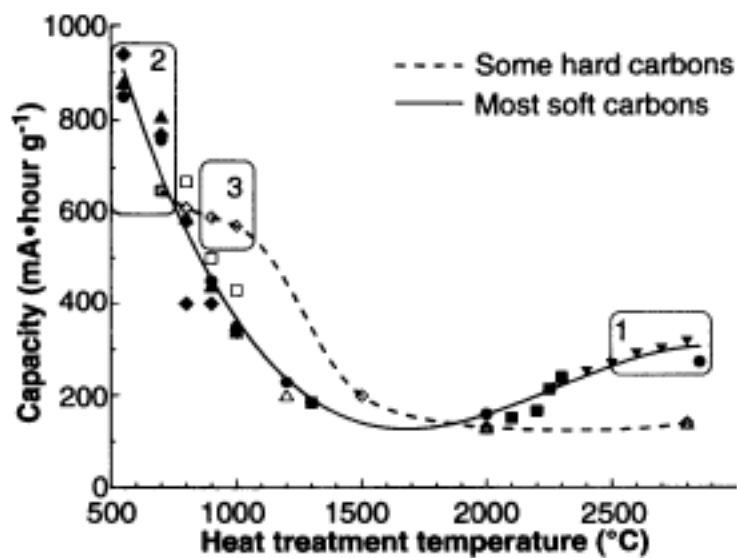


Figure 1.8. Plot of reversible capacity vs. heat treatment temperature for variety carbonaceous materials. (from Ref. 57. Dahn et al., *Science* **1995**, 270, 590.)

1.3.2. Anode materials for Li-ion batteries

Most carbonaceous materials can react with Li and be used as anode in LIBs. The intercalation process is strongly influenced by their surface area, morphology, crystallinity and orientation of the crystallites [57]. Figure 1.8 shows the maximum reversible capacity of carbonaceous materials as a function of the heat treatment temperature of organic precursors. Although highly disordered carbons have higher capacity values, they were not used due to their poorer reversibility. So, graphitic carbon has been mostly used in commercial batteries.

As an anode material, lithium is the most attractive material due to its light weight and the greatest electrochemical potential ($E_0 = -3.045$ V) that provides very high energy and power density in batteries. Unfortunately, lithium metal shows poor cycleability and safety in repeated charge/discharge cycles, which limit its direct application as anode in lithium batteries. In addition, the highly reactive lithium metal is not stable in the usual organic solvent electrolytes. Therefore, carbonaceous materials have been used as an anode material in LIBs due to its excellent cycleability and stability instead of lithium metal. Various types of carbons are obtained from organic precursors by changing the conditions of heat treatment. Generally, carbon electrode materials are

devided into graphitic and amorphous carbon. Typically, graphitic carbon has been used because stable charge/discharge profile. The theoretical capacity of the graphite is 372 mAh g^{-1} , which is calculated based on the charged state of C_6Li . Some amorphous carbon materials show higher specific capacity than graphite. These amorphous carbon materials are usually synthesized at a low temperature, and their specific capacities are varied from 400 to 2000 mAh g^{-1} . Amorphous carbon materials have additional sites to accomodate lithium ion due to the large defects and structural irregularity. However, these high capacities of amorphous carbon materials usually decay rapidly during the charge/discharge cycling.

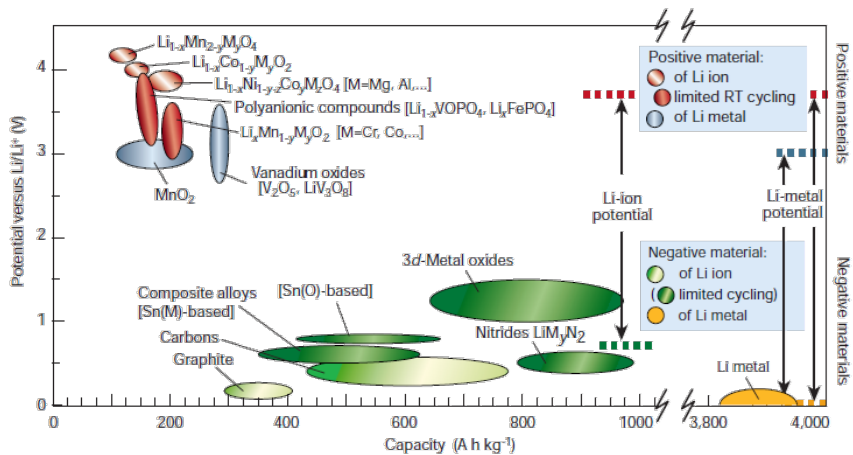


Figure 1.9. Voltage vs. capacity for electrode materials in Li-ion batteries. (from Ref. 51. Tarascon et al., *Nature* **2001**, 414, 359.)

1.3.2.1. Insertion reaction mechanism: graphite and titanium oxide

As shown in Figure 1.9, there are many alternative anode materials to replace the graphite anode in LIBs. The reaction mechanism is different for each material. In order to the development of new anode materials, the understanding of the reaction mechanism is essential.

Micro-sized particles of graphite have been used as anode for LIBs for many years. Nano-sized graphite particles could enhance the charge/discharge rate performance of LIBs. The solid electrolyte interface (SEI) layer is formed on the graphite surface by reduction of electrolyte at a potential less than 1 V versus Li^+/Li [58–60]. The SEI layer is essential for nano-sized graphite electrodes, because it inhibits the exfoliation of graphite. However, the formation of the SEI layer results in energy loss.

Several investigations have been reported on the fullerene, including the carbon nanotubes and C_{60} as electrodes [61,62]. Although carbon nanotubes have the twice lithium storage capacity compared with graphite, problems of safety and SEI layer formation are still remained. Hersam et al. have reported about Single-walled carbon nanotubes (SWCNTs) that could enhance their energy density and cycle durability [63]. They found that metallic SWCNTs accommodate lithium much

more efficiently than their semiconducting SWCNTs (Figure 1.10)

Recently, titanium oxide has also much attention as a promising intercalation host for lithium ion due to their safety and stable cycle property. Figure 1.11 shows the excellent cycle life capability of the defect spinel $\text{Li}_4\text{Ti}_5\text{O}_{12}$ electrode which is cheap and non-toxic [64,65]. However, the capacity is 150 mAh g^{-1} that is too low value as anode materials in LIBs.

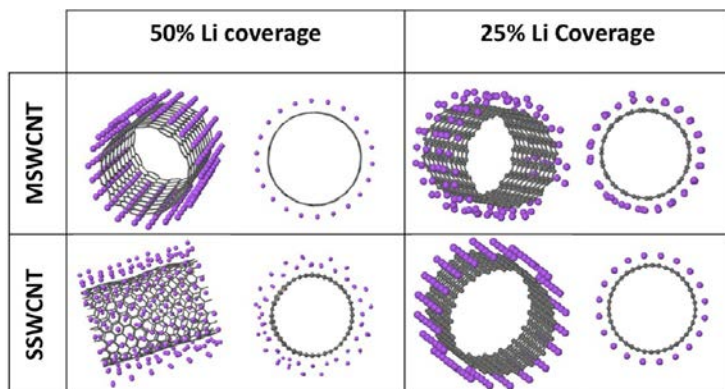


Figure 1.10. Lithium binding configurations on a metallic SWCNT (top) and a semiconducting SWCNT (bottom) at 50% and 25% lithium coverage. (from Ref. 63. Hersam et al., *ACS Nano* **2014**, 8, 2399.)

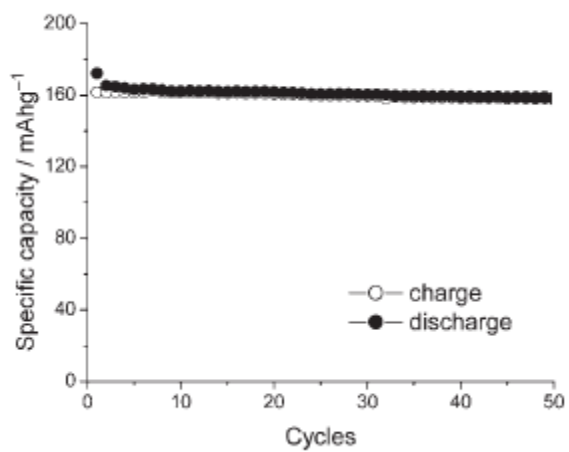


Figure 1.11. Cycle performance of $\text{Li}_4\text{Ti}_5\text{O}_{12}$ intercalation electrode at a rate of C/5. (from Ref. 64. Thackeray et al., *J. Electrochem. Soc.* **1994**, 141, L147.)

1.3.2.2. Alloying reaction mechanism: tin and silicon

Lithium metal alloys, Li_xM_y , have great interest as high capacity anode materials in LIBs. The alloys have high specific capacities which exceed that of the conventional graphite anode. For example, capacity of $\text{Li}_{4.4}\text{Sn}$ and $\text{Li}_{4.4}\text{Si}$ is 993 mAh g^{-1} and 4200 mAh g^{-1} , respectively, compare with 372 mAh g^{-1} for graphite. Unfortunately, the formation of the alloy is accompanied by large volume changes. These changes lead rapid degradation of the electrode, thus limiting its cycle life to only a few times. Significant research effort has been reported to overcome this problem. One of the earliest approaches involved replacing bulk material with nanostructured alloys [66]. As shown in Figure 1.12, a smaller particle or smaller grain size morphology of alloy electrode inhibits the volume changes of the reactive phase. Hollow tin dioxide microsphere has been reported as negative electrode that exhibit high energy density and stable cycle performance [67]. The smaller particle size and the hollow spherical structure reduced structural stress from the volume expansion and contraction during the charge/discharge cycling.

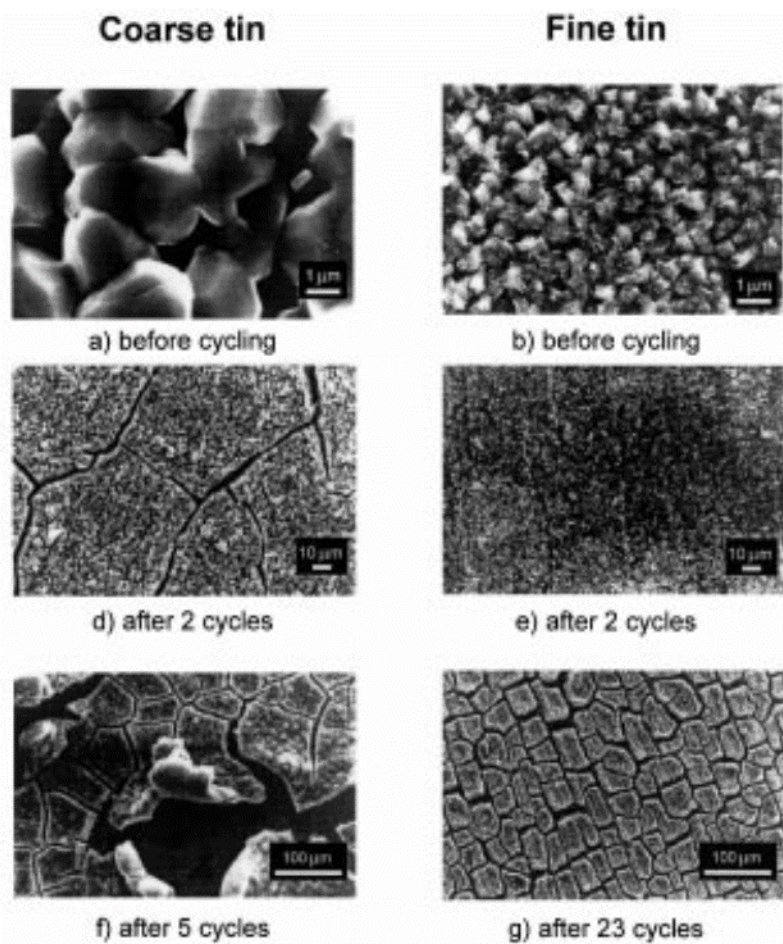


Figure 1.12. Effects of particle size during the cycling (from Ref. 66. Besenhard et al., *Electrochim. Acta* **1999**, 45, 31.)

Silicon is one of the attractive materials with high capacity as LIBs anode, but pulverization problem during cycling and an unstable SEI formation has the limited cycle performance [68-72]. Cui et al. show that anodes consisting of n silicon nanotube surrounded by a silicon oxide shell can cycle over 6,000 times in half cells while retaining more than 85% of their initial capacity [73]. Schematic of the fabrication process for double-walled silicon nanotubes (DWSiNTs) are shown in Figure 1.13. The silicon nanotube is prevented from expansion by the oxide shell, and the expanding inner surface is not exposed to the electrolyte, resulting in a stable SEI. Batteries containing these double-walled silicon nanotube anodes exhibit charge capacities approximately eight times larger than conventional carbon anodes and charging rates of up to 20C.

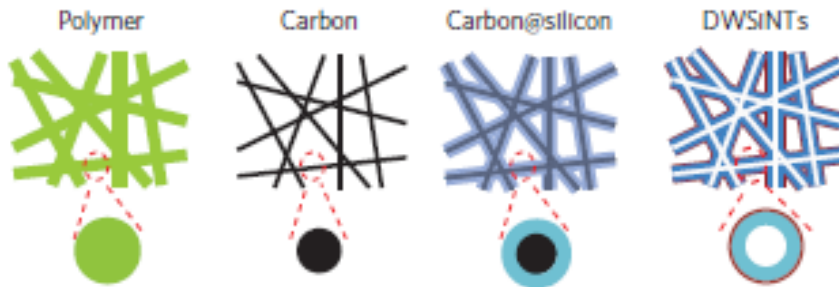


Figure 1.13. Schematic of the fabrication process for DWSiNTs. Polymer nanofibres (green) were first made by electrospinning. The polymer fibres were then carbonized and coated with silicon (blue) using a CVD method. By heating the sample in air at 500 °C, the inner carbon templates (black) were selectively removed, leaving continuous silicon tubes with a SiO_x mechanical constraining layer (red) (from Ref. 73. Cui et al., *Nat. Nanotechnol.* **2012**, 7, 310.)

1.3.2.3. Conversion reaction mechanism: transition metal oxide

Transition-metal oxides can react with Lithium ion by a conversion reaction. The transition metal oxides have no free voids to host lithium and metals do not form alloys with lithium. However, they can react reversibly with lithium according to the general reaction $MO + 2Li^+ + 2e^- = Li_2O + M^0$ [7]. Their full reduction leads to composite materials consisting of nano-sized metal particles (2–8 nm) dispersed in an amorphous Li_2O matrix (Figure 1.14). This conversion reactions were highly reversible, providing four times capacity to store lithium compare with that of graphite materials and these capacities can be retained for hundreds of cycles (Figure 1.15).

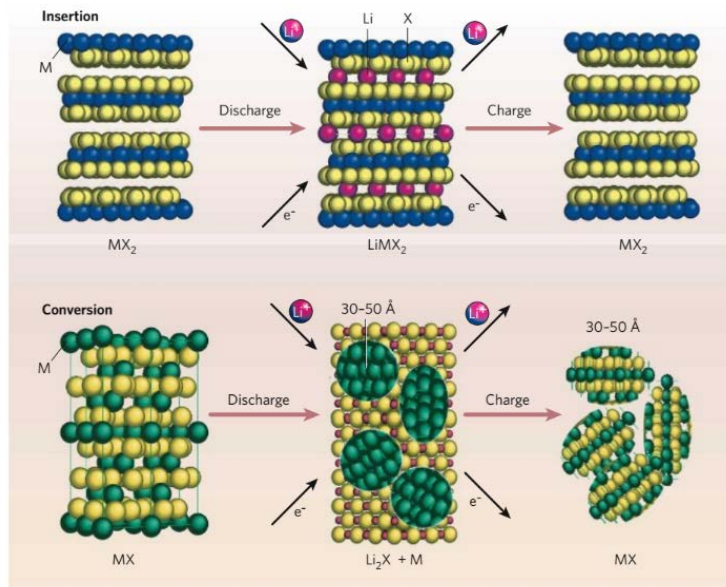


Figure 1.14. Schematic of the reaction mechanism for insertion and conversion reaction of anode materials (from Ref. 2. Armand et al., *Nature* **2008**, 451, 652.)

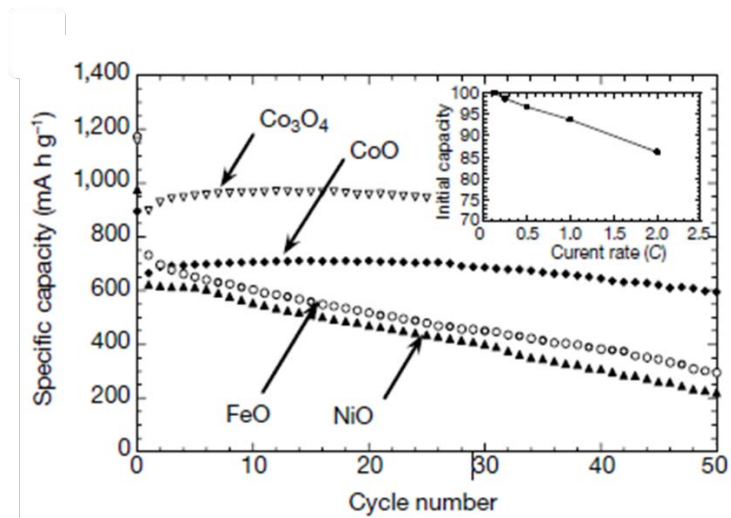


Figure 1.15. Cycling performance of transition metal oxide electrodes during the charge/discharge. (from Ref. 7. Tarascon et al., *Nature* **2000**, 407, 496.)

1.3.2.4. Carbon based metal or metal oxide nanocomposites

Metal, metal based alloy, and metal oxide materials are promising candidates of anode due to the extremely high capacity and low cost [74-77]. Despite the high energy density, metal or metal oxides have low electrical conductivity and poor durability as an anode in LIBs. During charging/discharging of metal or metal oxide anodes, reversible intercalation/deintercalation of Li ions occurs between the lattices of metal oxide [78]. This alloying or conversion reaction process causes considerable volume change and reduced crystallinity of the anode material with prolonged cycling, degrading the anode performance (Figure 1.16). Consequently, metal or metal oxide anode research has been focused on improving the charge transport and mechanical durability. For example, coating with a carbon layer on the surface of metal oxide nanoparticles can reduce the strain stress and the side reactions at the interface between metal oxide and electrolyte. Moreover, carbon's good electrical conductivity can complement the low conductivity of metal oxide.

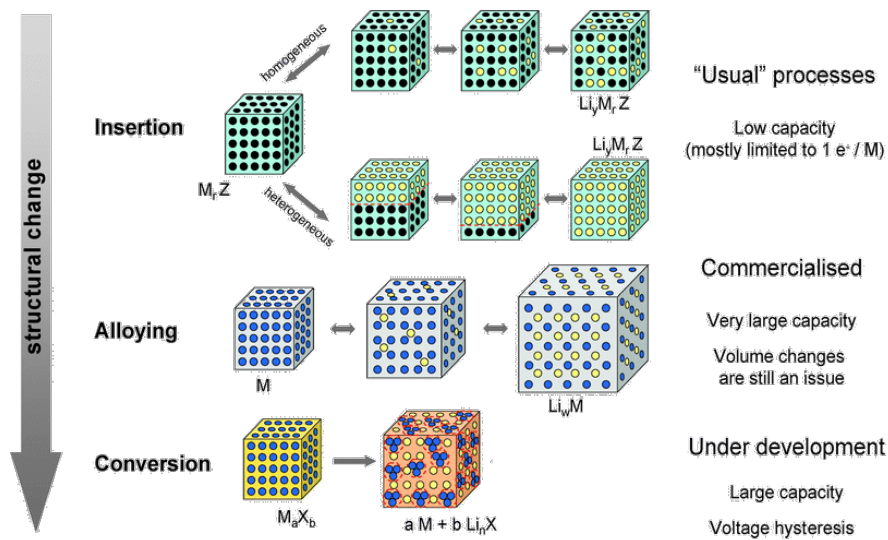


Figure 1.16. A schematic representation of the different reaction mechanisms observed in electrode materials for lithium batteries. Black circles: voids in the crystal structure, blue circles: metal, yellow circles: lithium. (from Ref. 78. Palacín et al., *Chem. Soc. Rev.* **2009**, 38, 2565.)

Very recently, Cui et al. have discovered that using a new nanostructured electrode with a silicon [79]. They place the silicon nanoparticles in yolk shells made from carbon, with enough spare room inside for them to swell and shrink without causing damage. As shown in figure 1.17, single silicon nanoparticles are encapsulated by a conductive carbon layer that leaves enough room for expansion and contraction following lithiation and delithiation.

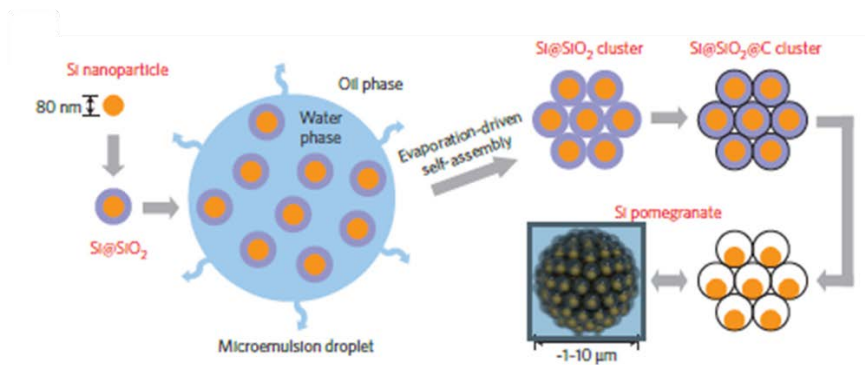


Figure 1.17. Schematic of the fabrication process for silicon pomegranates (from Ref. 79. Cui et al., *Nat. Nanotechnol.* **2014**, 9, 187.)

1.4. Dissertation Overview

Various designed synthetic methods of carbon-based nanomaterials have been investigated for electrochemical applications. Using various synthetic methods, different kinds of carbon-based materials have been obtained from the organic precursors such as surfactants and fatty acid.

Initially, a new and simple synthetic method of hollow carbon nanospheres was introduced. Monodispersed silica nanoparticles were used as templates and various metallic surfactants were used as carbon sources. Different shaped carbonaceous nanomaterials were obtained through the carbonization of metallic surfactant precursors.

Next, two dimensional (2-D) nanomaterials composed of highly monodisperse metal oxide nanoparticles and carbon were synthesized via simple heat treatment process using salt powder as template. The iron oleate complex was prepared by “Heating-up” method. 2-D nanostructure of the nanocomposite was created by using sodium sulfate salt powder as template. Initially, highly ordered 2-D assembly of iron oxide nanoparticles embedded in carbon matrix was formed on the surface of salt particles during the heat treatment. Subsequently, the nanocomposite was easily separated by dissolving salt in water.

Crystalline structure and particle size of iron oxide nanoparticles could be controlled by the heating rate and temperature of heat treatment.

Finally, the iron-oxide/graphene nanocomposite was directly obtained by heat treatment of a mixture of iron-oleate and graphene. The experimental results showed that uniform sized $\gamma\text{-Fe}_2\text{O}_3$ nanoparticles were homogeneously embedded in the graphene layers, and they acted as mutual spacers in the nanocomposite to prevent the restacking of the graphene layers and the nanoparticle's aggregation.

These carbon-based nanocomposites were shown to be excellent anode materials for Li-ion batteries with high capacity, good rate performance and stable durability.

1.5. References

- [1] M. Winter, R. J. Brodd., *Chem. Rev.* **2004**, 104, 4245.
- [2] M. Armand, J.-M. Tarascon, *Nature* **2008**, 451, 652.
- [3] C.-M. Park, J.-H. Kim, H. Kim, H.-J. Sohn, *Chem. Soc. Rev.* **2010**, 39, 3115.
- [4] A. S. Arico, P. Bruce, B. Scrosati, J.-M. Tarascon, W. V. Schalkwijk, *Nat. Mater.* **2005**, 4, 366.
- [5] P. G. Bruce, B. Scrosati, J.-M. Tarascon, *Angew. Chem. Int. Ed.* **2008**, 47, 2930.
- [6] Z. Yang, J. Zhang, M. C. W. Kintner-Meyer, X. Lu, D. Choi, J. P. Lemmon, J. Liu, *Chem. Rev.* **2011**, 111, 3577.
- [7] P. Poizot, S. Laruelle, S. Grugeon, L. Dupont, J.-M. Tarascon, *Nature* **2000**, 407, 496.
- [8] Y.-S. Hu, R. Demir-Cakan, M.-M. Titirici, J.-O. Müller, R. Schlögl, M. Antonietti, J. Maier, *Angew. Chem. Int. Ed.* **2008**, 47, 1645.
- [9] G. Ceder, *MRS Bull.* **2010**, 35, 693.
- [10] K. Kang, Y. S. Meng, J. Bréger, C. P. Grey, G. Ceder, *Science* **2006**, 311, 977.
- [11] S. Zeng, K. Tang, T. Li, Z. Liang, D. Wang, Y. Wang, Y. Qi, W. Zhou, *J. Phys. Chem. C* **2008**, 112, 4836.

- [12] M. V. Reddy, T. Yu, C.-H. Sow, Z. X. Shen, C. T. Lim, G. V. S. Rao, B. V. R. Chowdari, *Adv. Funct. Mater.* **2007**, 17, 2792.
- [13] P. L. Taberna, S. Mitra, P. Poizot, P. Simon, J.-M. Tarascon, *Nat. Mater.* **2006**, 5, 567.
- [14] X. W. Lou, D. Deng, J. Y. Lee, J. Feng, L. A. Archer, *Adv. Mater.* **2008**, 20, 258.
- [15] R. L. McCreery, *Chem. Rev.* **2008**, 108, 2646.
- [16] R. W. Cahn, B. Harris, *Nature* **1969**, 221, 132.
- [17] T.-Y. Ma, L. Liu, Z.-Y. Yuan, *Chem. Soc. Rev.* **2013**, 42, 3977.
- [18] F. Clifford, U. B. Marvin, *Nature* **1967**, 214, 587.
- [19] A. K. Geim, *Science* **2009**, 324, 1530.
- [20] S. Stankovich, D. A. Dikin, G. H. B. Dommett, K. M. Kohlhaas, E. J. Zimney, E. A. Stach, R. D. Piner, S. T. Nguyen, R. S. Ruoff, *Nature* **2006**, 442, 282.
- [21] C. N. R. Rao, A. K. Sood, K. S. Subrahmanyam, A. Govindaraj, *Angew. Chem. Int. Ed.* **2009**, 48, 7752.
- [22] J. R. Miller, R. A. Outlaw, B. C. Holloway, *Science* **2010**, 329, 1637.
- [23] P. Lian, X. Zhu, S. Liang, Z. Li, W. Yang, Wang, *Electrochim. Acta* **2010**, 55, 3909.
- [24] M. A. Worsley, P. J. Pauzauskie, T. Y. Olson, J. Biener, J. H. Satcher, T. F.

- Baumann, *J. Am. Chem. Soc.* **2010**, 132, 14067.
- [25] W. Chen, S. Li, C. Chen, L. Yan, *Adv. Mater.* **2011**, 23, 5679.
- [26] X. Zhu, Y. Zhu, S. Murali, M. D. Stoller, R. S. Ruoff, *ACS Nano* **2011**, 5, 3333.
- [27] Z. Zhu, T. Zhu, X. Zhou, Y. Zhang, X. W. Lou, X. Chen, H. Zhang, H. H. Hng, Q. Yan, *Nanoscale* **2011**, 3, 1084.
- [28] B. Jang, M. Park, O. B. Chae, S. Park, Y. Kim, S. M. Oh, Y. Piao, T. Hyeon, *J. Am. Chem. Soc.* **2012**, 134, 15010.
- [29] C. T. Kresge, M. E. Leonowicz, W. J. Roth, J. C. Vartuli, J. S. Beck, *Nature* **1992**, 359, 710.
- [30] Q. Zhang, E. Uchaker, S. L. Candelaria, G. Cao, *Chem. Soc. Rev.* **2013**, 42, 3127.
- [31] V. Valtchev, L. Tosheva, *Chem. Rev.* **2013**, 113, 6734.
- [32] J. Lee, J. Kim, T. Hyeon, *Adv. Mater.* **2006**, 18, 2073.
- [33] S. K. Behera, *J. Power Sources* **2011**, 196, 8669.
- [34] Z.-M. Cui, L.-Y. Jiang, W.-G. Song, Y.-G. Guo, *Chem. Mater.* **2009**, 21, 1162.
- [35] H. B. Wu, J. S. Chen, H. H. Hng, X. W. Lou, *Nanoscale* **2012**, 4, 2526.
- [36] Y.-S. Hu, R. Demir-Cakan, M.-M. Titirici, J.-O. Müller, R. Schlögl, M. Antonietti, J. Maier, *Angew. Chem. Int. Ed.* **2008**, 47, 1645.

- [37] H. Kim, J. Cho, *Nano Lett.* **2008**, 8, 3688.
- [38] X. W. Lou, C. M. Li, L. A. Archer, *Adv. Mater.* **2009**, 21, 2536.
- [39] X.-L. Wu, L.-Y. Jiang, F.-F. Cao, Y.-G. Guo, L.-J. Wan, *Adv. Mater.* **2009**, 21, 2710.
- [40] Y. Piao, H. S. Kim, Y.-E. Sung, T. Hyeon, *Chem. Commun.* **2010**, 46, 118.
- [41] C. Ban, Z. Wu,; D. T. Gillaspie, L. Chen, Y. Yan, J. L. Blackburn, A. C. Dillon, *Adv. Mater.* **2010**, 22, E145.
- [42] B. T. Hang, I. Watanabe, T. Doi, S. Okada, J.-I. Yamaki, *J. Power Sources* **2006**, 161, 1281.
- [43] S. A. Needham, G. X. Wang, K. Konstantinov, Y. Tournayre, Z. Lao, H. K. Liu, *Electrochem. Solid-State Lett.* **2006**, 9, A315.
- [44] W.-M. Zhang, X.-L. Wu, J.-S. Hu, Y.-G. Guo, L.-J. Wan, *Adv. Funct. Mater.* **2008**, 18, 3941.
- [45] A. N. Goldstein, C. M. Echer, A. P. Alivisatos, *Science* **1992**, 256, 1425.
- [46] Y. Piao, J. Kim, H. B. Na, D. Kim, J. S. Baek, M. K. Ko, J. H. Lee, M. Shokouhimehr, T. Hyeon, *Nat. Mater.* **2008**, 7, 242.
- [47] Y. I. Park, Y. Piao, N. Lee, B. Yoo, B. H. Kim, S. H. Choi, T. Hyeon, *J. Mater. Chem.* **2011**, 21, 11472.
- [48] Y. C. Han, H. G. Cha, C. W. Kim, Y. H. Kim, Y. S. Kang, *J. Phys. Chem. C* **2007**, 111, 6275.

- [49] C.-B. Rong, N. Poudyal, G. S. Chaubey, V. Nandwana, Y. Liu, Y. Q. Wu, M. J. Kramer, M. E. Kozlov, R. H. Baughman, J. P. Liu, *J. Appl. Phys.* **2008**, 103, 07E131.
- [50] D. Li, N. Poudyal, V. Nandwana, Z. Jin, K. Elkins, J. P. Liu, *J. Appl. Phys.* **2006**, 99, 08E911.
- [51] J.-M. Tarascon, M. Armand, *Nature* **2001**, 414, 359.
- [52] K. Mizushima, P. C. Jones, P. J. Wiseman, J. B. Goodenough, *Mater. Res. Bull.* **1980**, 15, 783.
- [53] M. M. Thackeray, W. I. F. David, P. G. Bruce, J. B. Goodenough, *Mater. Res. Bull.* **1983**, 18, 461.
- [54] M. Mohri, N. Yanagisawa, Y. Tajima, H. Tanaka, T. Mitate, S. Nakajima, M. oshida, Y. Yoshimoto, T. Suzuki, H. Wada, *J. Power Sources* **1989**, 26, 545.
- [55] V. Etacheri, R. Marom, R. Elazari, G. Salitra, D. Aurbach, *Energy Environ. Sci.* **2011**, 4, 3243.
- [56] M. S. Whittingham, *Chem. Rev.* **2004**, 104, 4271.
- [57] J. R. Dahn, T. Zheng, Y. H. Liu, J. S. Xue, *Science* **1995**, 270, 590.
- [58] R. Fong, V. V. Schen, J. R. Aohn, *J. Electrochem. Soc.* **1990**, 137, 2009.
- [59] R. Hanno, Y. Kawamdo, *J. Electrochem. Soc.* **1992**, 139, 3397.
- [60] E. Peled, *J. Electrochem. Soc.* **1979**, 126, 40.

- [61] R. S. Morris, B. G. Dixon, T. Gennett, R. Raffaele, M. J. Heben, *J. Power Sources* **2004**, 138, 277.
- [62] Z. Zhou, J. J. Zhao, X. P. Gao, Z. F. Chen, J. Yan, P. V. Schiever, M. Morinaga, *Chem. Mater.* **2005**, 17, 992.
- [63] L. Jaber-Ansari, H. Iddir, L. A. Curtiss, M. C. Hersam, *ACS Nano* **2014**, 8, 2399.
- [64] E. Ferg, R. J. Gummow, A. Dekock, M. M. Thackeray, *J. Electrochem. Soc.* 1994, 141, L147.
- [65] A. N. Jansen, A. J. Kahalan, K. D. Kepler, P. A. Nelson, K. Amine, D.W. Dees, D. R. Vissers, M. M. Thackeray, *J. Power Sources* **1999**, 81, 902.
- [66] M. Winter, J. O. Besenhard, *Electrochim. Acta* **1999**, 45, 31.
- [67] S. Han, B. Jang, T. Kim, S. M. Oh, T. Hyeon, *Adv. Funct. Mater.* **2005**, 15, 1845.
- [68] L. Y. Beaulieu, K.W. Eberman, R. L. Turner, L. J. Krause, J. R. Dahn, *Electrochem. Solid State Lett.* **2001**, 4, A137.
- [69] J. O. Besenhard, J. Yang, M. Winter, *J. Power Sources* **1997**, 68, 87.
- [70] T. D. Hatchard, J. R. Dahn, *J. Electrochem. Soc.* **2004**, 151, A838.
- [71] W. J. Weydanz, M. Wohlfahrt-Mehrens, R. A. Huggins, *J. Power Sources* **1999**, 81, 237.
- [72] X.-W. Zhang, P. K. Patil, C. Wang, A. J. Appleby, F. E. Little, D. L. Cocke,

- J. Power Sources* **2004**, 125, 206.
- [73] H. Wu, G. Chan, J. W. Choi, I. Ryu, Y. Yao, M. T. McDowell, S. W. Lee, A. Jackson, Y. Yang, L. Hu, Y. Cui, *Nat. Nanotechnol.* **2012**, 7, 310.
- [74] J. Cabana, L. Monconduit, D. Larcher, M. R. Palacín, *Adv. Mater.* **2010**, 22, E170.
- [75] M. G. Kim, J. Cho, *Adv. Funct. Mater.* **2009**, 19, 1497.
- [76] C. K. Chan, X. F. Zhang, Y. Cui, *Nano Lett.* **2008**, 8, 307.
- [77] W.-J. Zhang, *J. Power Sources* **2011**, 196, 13.
- [78] M. R. Palacín, *Chem. Soc. Rev.* **2009**, 38, 2565.
- [79] N. Liu, Z. Lu, J. Zhao, M. T. McDowell, H.-W. Lee, W. Zhao, Y. Cui, *Nat. Nanotechnol.* **2014**, 9, 187.

Chapter 2. Thin-Layered Hollow Carbon Nanostructures by the Direct Pyrolysis of Surfactants

2.1. Introduction

Hollow carbon nanostructures (HCNS), along with activated carbon, nanotubes, graphene, and other carbon-based materials, have received considerable attention due to their interesting characteristics such as large voids, spherical shape, low density, large surface area, and good stability. HCNS have found use in various areas, e.g., as catalyst supporting materials, anode material for Li-ion secondary batteries, electrode material for supercapacitors and as drug delivery vehicles [1-4]. Various methods, such as the most commonly used template synthesis approach, have been developed to synthesize HCNS [5-9]. However, most of the template synthesis methods involve multiple processing steps, including an additional treatment step for the cross-linking or polymerization of organic substances within the template as well as for the final removal of the template [10,11]. Recently, He et al. introduced a relatively simple method for the fabrication of nanofibers, nanoporous materials, and beads using a bubble electrospinning and blown bubble spinning technique [12]. In this chapter, a new and simple template synthesis method for the generation of HCNS by direct carbonization of metallic surfactants was introduced. This approach simplifies previous

complicated template synthesis.

2.2. Experimental Section

2.2.1. Chemicals

A styrene monomer was purchased from Aldrich Chemical Co. and the inhibitor in the styrene monomer was removed by a 1 M NaOH aqueous solution. Sodium dodecyl sulfate (SDS), potassium peroxydisulfate (KPS), sodium bisulfate and tetraethyl orthosilicate (TEOS) were purchased from Aldrich Chemical Co.. Sodium oleate and potassium oleate were purchased from TCI.

2.2.2. Characterization methods

The transmission electron microscopy (TEM) was performed using a JEOL EM-2010 microscope at an acceleration voltage of 200 kV. The field-emission scanning electron microscopic (FE-SEM) images were obtained using a S-4800 (Hitachi) microscope. The Brunauer-Emmett-Teller (BET) method was used to confirm the specific surface area and volume using a BELSORP-mini II (BEL JAPAN) nitrogen absorption analyzer. The thermogravimetric analysis (TGA) was conducted to

confirm Figure the carbonization and decomposition temperature using a Mettler TG-50. Raman spectrum was obtained by using MonoRa500i.

2.2.3 Preparation of SDS coated PS nanoparticle solutions [13,14].

PS nanoparticles were prepared via emulsion polymerization method. In a typical synthesis, 0.594 g SDS was dissolved in 58 ml D.I. water and heated up to 85 °C with stirring. Then, 15 ml styrene monomer was added to the solution. Polymerization of PS was started by injection of 0.046 g of KPS and same amount of sodium bisulfate dissolved in 2 ml D.I. water. After 12 h, the polymerization was completed and white opaque dispersion of SDS coated PS nanoparticles in water was obtained.

2.2.4 Preparation of SDS coated SiO₂ nanoparticle solutions [15].

In a typical synthesis, 0.5 ml TEOS and 2.5 ml ammonia solutions were added to a mixture of 10 ml D.I. water and 90 ml ethanol with vigorous stirring. The mixture solution was further stirred for 24 h at room temperature. SDS was added to the SiO₂ nanoparticles solution and stirred for 1h to prepare the SDS coated SiO₂.

2.2.5. Synthesis of HCNS using SDS-coated template nanoparticles.

The typical HCNS synthesis procedure is shown in Figure 1. In the polystyrene (PS) template synthesis, sodium dodecyl sulfate (SDS)-coated PS nanoparticle powder was prepared by drying the as-synthesized PS solution at 85 °C in a convection oven for 6 h. The resulting material was subsequently heat treated at 600 °C under a N₂ atmosphere for 3 h. Black HCNS powder was produced by the carbonization of SDS and the decomposition of PS template. In the SiO₂ template synthesis, the as-synthesized SiO₂ nanoparticles solution was dried at 85 °C in a convection oven for 6 h, and the resulting material was then heat treated at 600 °C under a N₂ atmosphere for 3 h. A carbon-coated SiO₂ black powder was produced according to the carbonization process of SDS. The SiO₂ nanoparticle template was then etched by using a 6 M NaOH solution at 85 °C for 3 h. The HCNS powder was finally obtained after washing with D.I. water and drying at 100 °C in a convection oven for 6 h.

2.2.6. Synthesis of Thin Layered Carbon Materials Using Non-metallic Surfactants.

The typical synthesis procedure was described in Figure 2.1b. CTAB 1 g or oleic acid 1 ml and NaCl 10 g or Na₂SO₄ 10 g were mechanically

mixed until became a homogeneous mixture. The resulting material was subsequently heat treated at 600 °C under a N₂ atmosphere for 3 h. A black powder of carbon coated salts was produced. The thin layered carbon materials were produced after washing with D.I water for the removal of salts.

2.2.7. Heat treatment experiments of metallic surfactants.

Typical experiments were conducted to observe the thermal transformations of the metallic surfactants. 1 g of each metallic surfactant was placed in a 100 ml round-bottomed flask and maintained under a N₂ flow at room temperature for 10 min. Subsequently, each sample was heated up to 350 °C at the increasing rate of 10 °C min⁻¹.

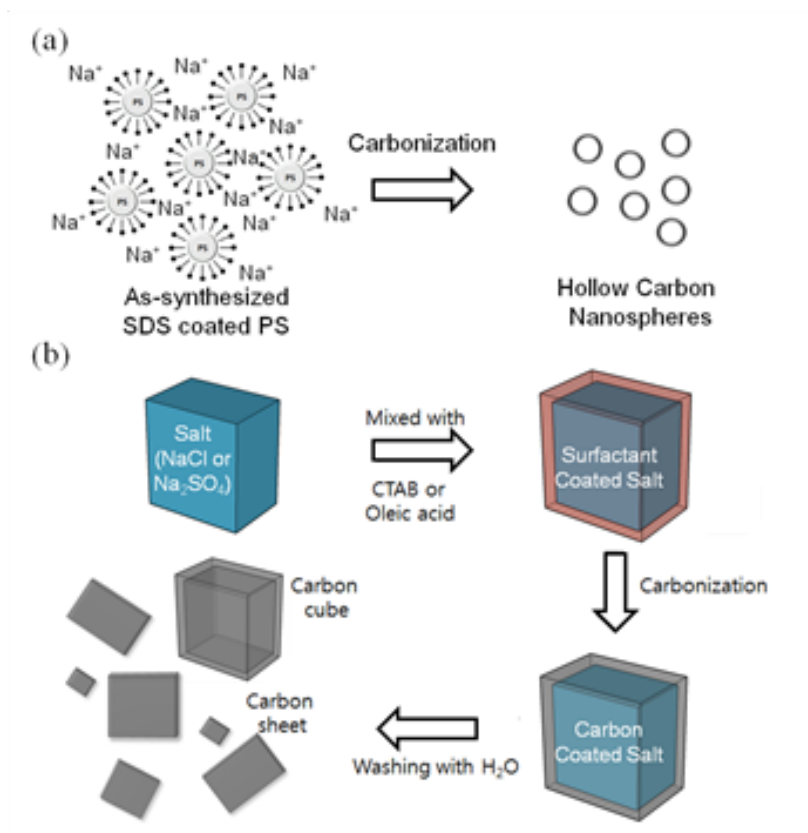


Figure 2.1. Schematic of the direct carbonization of surfactants by a template method. (a) Hollow carbon nanospheres from metallic surfactants and (b) hollow nanocube from non-metallic surfactants.

2.3. Results and Discussion

Figure 2.1a shows the direct carbonization in the template synthesis method using metallic surfactants. PS and SiO₂ nanoparticles were used as templates for the synthesis of HCNS. Two kinds of metallic surfactants - sodium dodecyl sulfate (SDS) and sodium oleate (SO) - were used as carbon sources for the HCNS. These metallic surfactants coated onto PS and SiO₂ nanoparticles were directly carbonized and transformed into HCNS via heat treatment.

In 2002, Jang et al. described the preparation of carbon nanocapsules and MCFs using multiple processes [16]. In their work, the metallic surfactant, SDS, was used as a stabilizer. However, in this experiment, SDS was converted to nanostructured carbon material during the heat treatment. Although there are many reports related to the catalytic effect of metal cation during the transformation of an organic compound to a carbon nanostructured material, the mechanism of the carbonization of SDS is yet to be clearly defined [17-19]. Mochida et al. investigated the carbonization of aromatic hydrocarbons catalyzed by alkali metal cations [20].

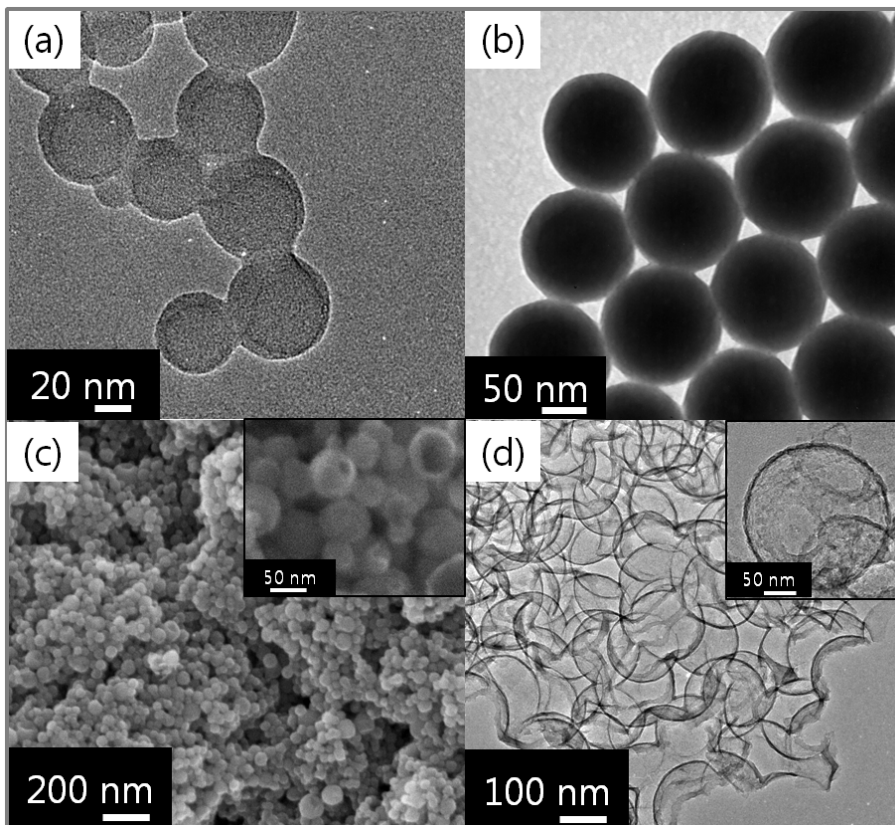


Figure 2.2. Electron microscope images of the template nanoparticles and the carbon materials from metallic surfactants. (a) The as-synthesized SDS-coated PS, (b) SDS-coated SiO₂ nanoparticles, (c) FESEM image of HCNS from SDS-coated PS and (d) TEM image of HCNS from SDS-coated SiO₂. (Inset: High magnification image).

TEM images of SDS-coated PS and SiO₂ nanoparticles are shown in Figs. 2.2a and 2.2b, respectively. The SDS-coated PS directly transformed into a hollow spherical structure after heat treatment at 600 °C under a N₂ atmosphere (Figure 2.2c). The high magnification TEM image (Figure 2.3) revealed that the carbon nanosphere had a hollow inner space with thin wall. The average diameter and wall thickness of the HCNS from the SDS-coated PS was about 30 nm and 2.5 nm, respectively. HCNS was also generated by using SiO₂ as a hard template (Figure 2.2d), but in this case, the synthesis procedure was slightly more complicated, as an additional NaOH etching process was needed. The wall of HCNS was extremely thin compared to the previously reported HCNS, due to the absence of additional carbon source.

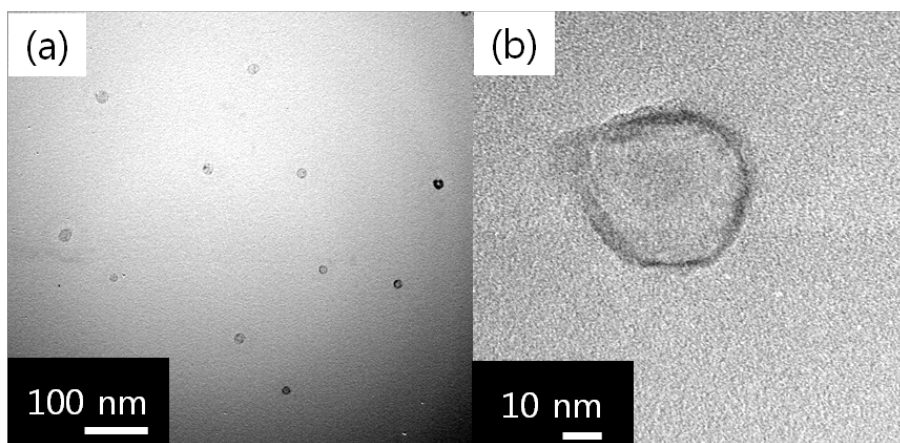


Figure 2.3. Low and high magnification TEM images of HCNS obtained from SDS-coated PS nanoparticles.

The structure of an inorganic template should not undergo any change during the carbonization process, whereas an organic template can be allowed to melt or decompose. Hence, the decomposition temperature (T_d) and melting point (T_m) of an organic template are critical factors in the production of a specific carbon nanostructure. In particular, for a PS template with $T_m = 240\text{ }^\circ\text{C}$, the thermo gravimetric analysis (TGA) result confirmed that PS began to decompose at $400\text{ }^\circ\text{C}$ (T_d) (Figure 2.4a). The experimental results showed that, in order to generate HCNS, the carbonization temperature (T_c) of a metallic surfactant must be lower than the T_m or T_d of the organic template. If the T_c value of the metallic surfactant is higher than the T_m or T_d values of the organic template, a hollow structure will not be created due to deformation of the organic template. Thus, the SO-coated PS nanoparticles did not generate a hollow structure as the T_c value of SO was higher than the T_d value of PS. The PS nanoparticles therefore could not sustain their spherical structure before the carbonization of SO, resulting in the formation of non-hollow carbon material (Figure 2.5). Non-metallic surfactants, such as oleic acid and cetyltrimethylammonium bromide (CTAB), were completely decomposed without any residue after heat treatment under a N_2 atmosphere due to the absence of any catalytic metal cation.

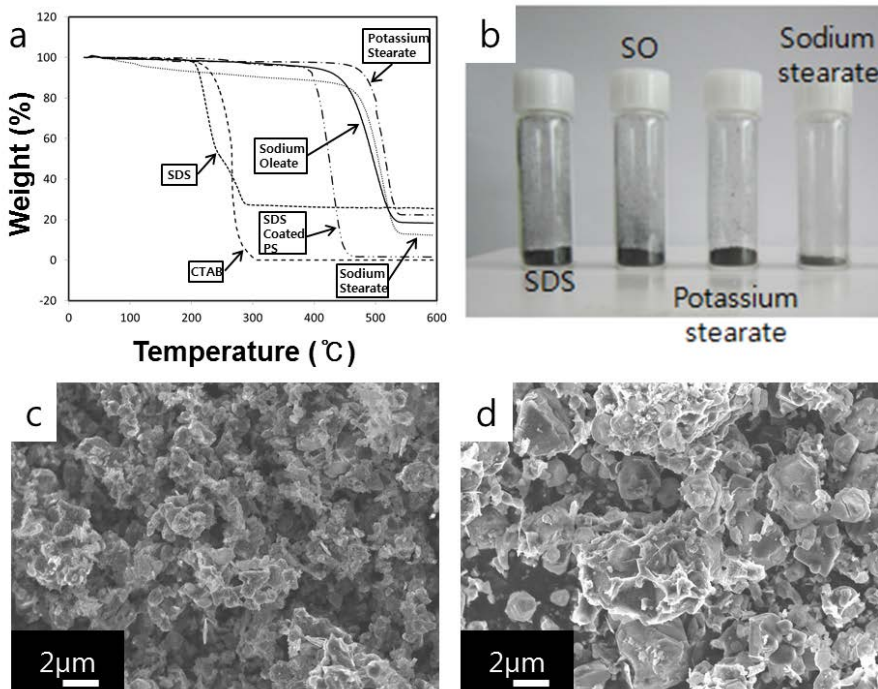


Figure 2.4. (a) TGA diagrams of various surfactants and (b) optical images after heat treatment. SEM images of carbon materials from pure (c) SDS and (d) SO.

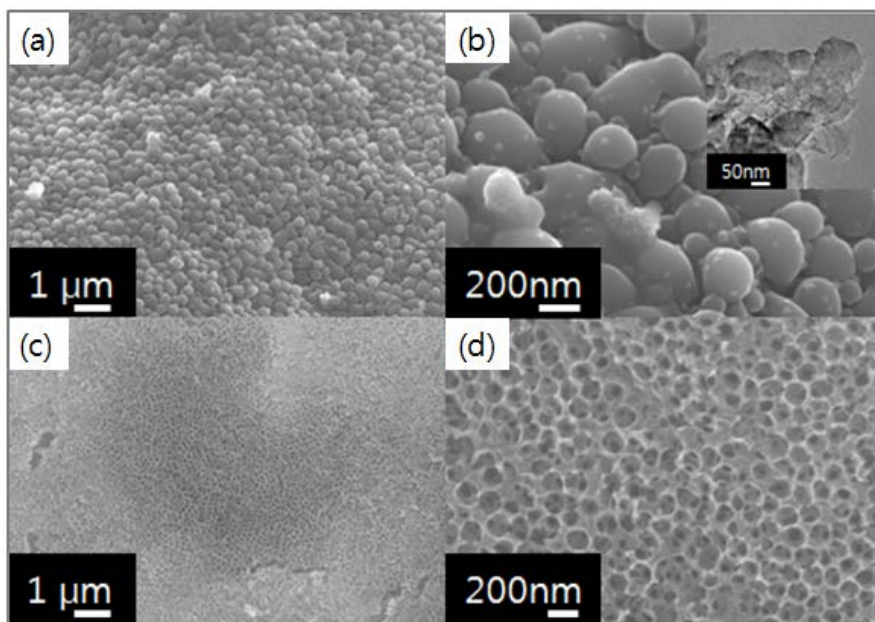


Figure 2.5. SEM images of the carbon nanomaterials from (a and b) SO-coated PS and (c and d) SO-coated SiO₂ template. (Inset: High magnification TEM image).

In the case of non-metallic surfactants such as oleic acid and cetyltrimethylammonium bromide (CTAB), they were completely decomposed without any residue after the heat treatment under a N₂ atmosphere due to the absence of catalytic alkali metal. In order to generate carbon materials from non-metallic surfactants, alkali metal salts such as NaCl and Na₂SO₄ were used as a catalyst and a template. Figure 2.1b depicts a schematic of the synthesis of thin layered carbon materials from non-metallic surfactants using sodium based salts. Electron microscope images (Figure 2.6) and Raman spectra (Figure 2.7) of obtained materials showed that they had thin layered carbon structures which were similar to the graphene. The Raman spectra showed two distinguishable peaks at around 1335 cm⁻¹ (D band) and 1605 cm⁻¹ (G band), indicating that the obtained carbon materials were disordered nanocrystalline graphite [21,22]. As it happened, hollow carbon cube was generated when NaCl was used as a template. It was obvious that NaCl acted as a template and a carbonization catalyst for the generation of thin layered carbon structures.

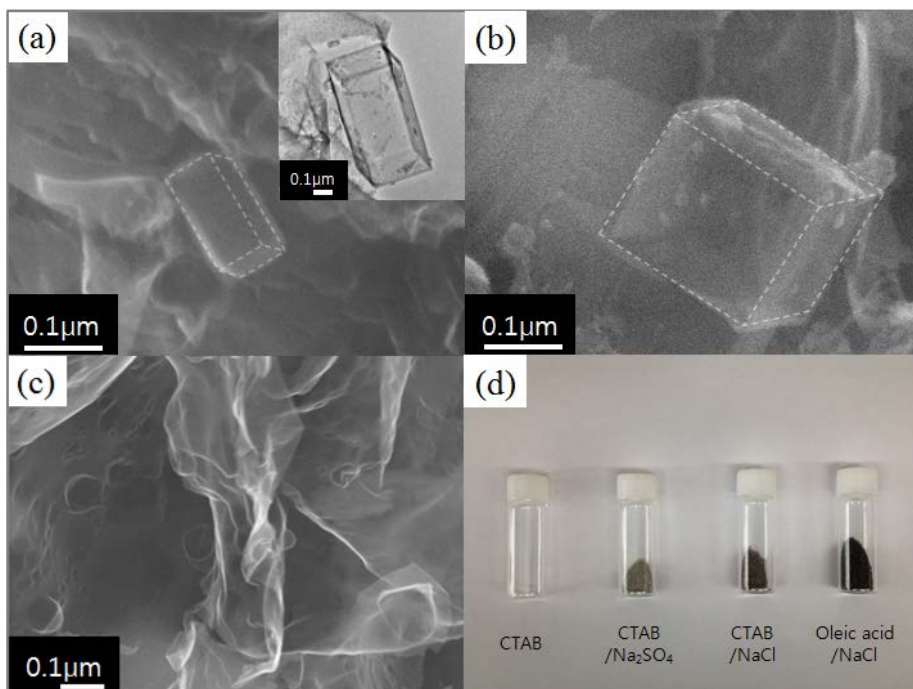


Figure 2.6. Electron microscope images of thin layered carbon materials from (a) Oleic acid/NaCl, (b) CTAB/NaCl and (c) CTAB/Na₂SO₄. (d) Optical image of as-heat treated samples without washing process. (Inset: High magnification TEM image).

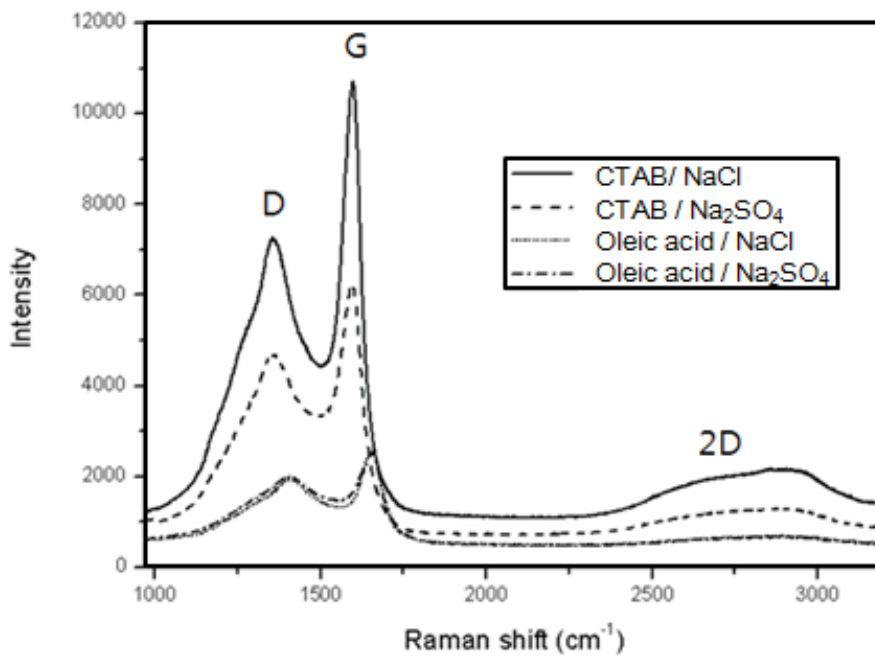


Figure 2.7. Raman spectra of thin layered carbon materials from non-metallic surfactants.

To investigate the carbonization phenomena during the direct carbonization of metallic surfactants, a visual observation and TGA were conducted, and it was observed that the transformation of the organic compound precursors to carbon materials were occurred during the heat treatment (Figure 2.8). SDS powder was heated in a round-bottomed flask to 350 °C under nitrogen flow. The white SDS powder instantaneously became a black carbonaceous powder at around 220 °C without melting (Figure 2.8a). The TGA result of the SDS showed that the weight began to drop rapidly at 200–290 °C (Figure 2.4a). According to our observations, the T_c value of the SDS was strongly related to the weight decrease in the TGA result. Thus, the weight loss during the carbonization of SDS was essentially due to the volatilization of the organic compounds [23]. Similarly, SO powder, heated in a round bottom flask, melted at about 280 °C, and it could not transform into a carbonaceous material until 350 °C was reached (Figure 2.8b). The TGA result of the SO provided evidence of reduction in weight at temperatures of 400–520 °C. Moreover, after heat treatment at 600 °C, SO transformed into a carbonaceous powder. It was thus clear that SO melted and was subsequently carbonized above a temperature of 400 °C. Thus, as SDS was carbonized near 220 °C and SO was carbonized near 400 °C under

a N₂ atmosphere, due to its low T_c, SDS was more favorable metallic surfactant than SO, for generating carbon nanostructures in the organic template method. In order to confirm the general applicability of the current direct carbonization process, sodium stearate and potassium stearate were also used as precursors to prepare nanostructured carbon under the same experimental conditions. Both of the two surfactants were directly carbonized to generate carbonaceous materials (Figure 2.4b).

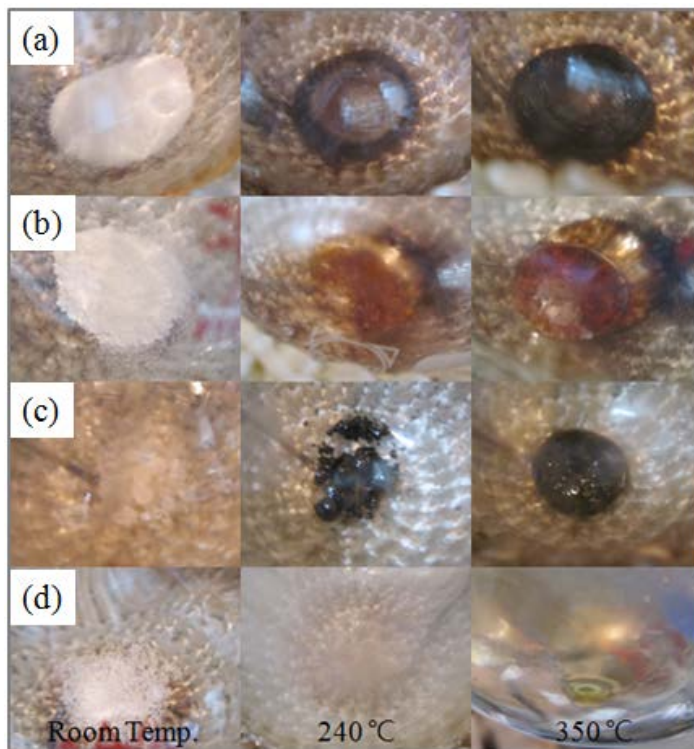


Figure 2.8. Photo images of (a) SDS, (b) SO, (c) SDS coated PS and (d) purified PS polymer in round bottle flasks during the heat treatment from room temperature to 350 °C under N₂ atmosphere. SDS was carbonized at 240 °C, while SO and PS were melted at 350 °C.

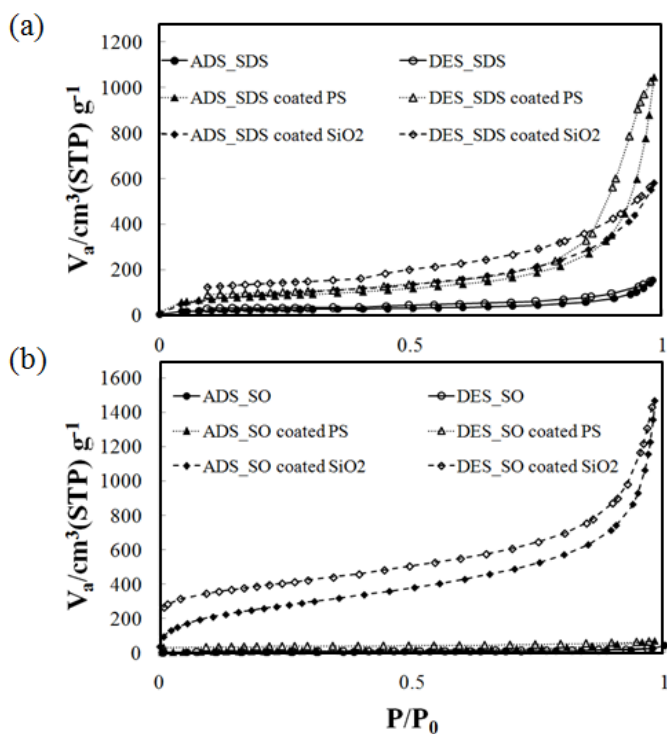


Figure 2.9. Ar isotherms (at 87 K) of the obtained nanostructured carbon materials obtained by direct carbonization of (a) SDS and (b) SO.

The specific surface area and pore volume of the obtained carbonaceous materials from metallic surfactants were measured by the Brunauer-Emmett-Teller method (Figure 2.9). The carbonaceous materials from metallic surfactants using a template synthesis had a higher specific surface area and pore volume compare to that without a template owing to their ordered and hollow structure. The specific area ($429.19 \text{ m}^2/\text{g}$) of the carbon from the SDS coated PS was higher than the carbon from the pure SDS ($122.43 \text{ m}^2/\text{g}$). The HCNS also had a larger surface area and pore volume than the carbon from the pure metallic surfactant (Table 2.1).

Table 2.1. Specific surface area and pore volume of carbonaceous materials from metallic surfactants.

Sample	SDS	SDS coated PS	SDS coated SiO ₂	SO	SO coated PS	SO coated SiO ₂
S _{BET_Ar} [m ² /g]	122.43	429.19	788.38	14.16	36.91	973.31
V _{pore} [cm ³ /g]	0.247	1.507	1.349	0.050	0.087	1.87

2.4. Conclusion

Over the past decade, the control of elemental composition, size and shape of nanostructures has been major research topics in the chemistry of nanostructures. Surfactant is an organic material that is amphiphilic and begins to form micelle at the critical micelle concentration (CMC) to reduce the surface tension. For this unique property, it is widely used as a detergent, wetting agent, emulsifier, foaming agent, and dispersant in many fields. Especially in nanochemistry, surfactant plays an important role such as nano-reactor, capping agent, self assembly monolayer (SAM) and so on. Surfactant can be classified by the group in its head [24-26]. In particular, anionic surfactant has negative charge group in its head such as sulfate, sulfonate, phosphate and carboxylate. Negative charge group of anionic surfactant is normally conjugated with alkaline, alkaline earth and transition metal cation. When surfactant is used as a dispersant or stabilizer in nanochemistry, it is considered as an impurity so that subsequently removed by purification process with organic solvent or heat treatment.

Various carbon structured materials including the HCNS and 3-dimensional ordered mesoporous (3-DOM) structure were generated by

direct carbonization of metallic surfactants using template synthesis. PS nanoparticles are used as the organic template. SDS-coated PS nanoparticles are directly carbonized to generate HCNS by heat treatment. SO is also directly carbonized, but it does not generate hollow structures due to its thermal property. In the case of non-metallic surfactants, they are not carbonized themselves but carbonized by aid of the alkali metal salts. Thin layered carbon materials are generated from non-metallic surfactants using the alkali metal salts as a catalyst and a template. These synthetic methods simplify the complicated synthetic procedure of template method because additional processes were not necessary such as addition of catalyst or carbon source. Our approach will provide the easy synthesis route for the generation of carbon based nanocomposites with inorganic materials, including the catalyst, active electrode materials for diverse electrochemical applications.

2.5. References

- [1] C. Burda, X. Chen, R. Narayanan, M. A. El-Sayed, *Chem. Rev.* **2005**, 105, 1025.
- [2] Y. Wang, F. Su, J. Y. Lee, X. S. Zhao, *Chem. Mater.* **2006**, 18, 1347.
- [3] W.M. Zhang, J.S. Hu, Y.G. Guo, S.F. Zheng, L.S. Zhong, W.G. Song, L.J. Wan, *Adv. Mater.* **2008**, 20, 1160.
- [4] J. Lee, S. Yoon, T. Hyeon, S. M. Oh, K. B. Kim, *Chem. Commun.* **1999**, 21, 2177.
- [5] Y. Jing, Y. Zhu, X. Yang, J. Shen, C. Li, *Langmuir* **2011**, 27, 1175.
- [6] S. B. Yoon, K. Sohn, J. Y. Kim, C.-H. Shin, J.-S. Yu, T. Hyeon, *Adv. Mater.* **2002**, 14, 19.
- [7] N. A. Katcho, E. Urones-Garrote, D. Ávila-Brandé, A. Gómez-Herrero, S. Urbonaite, S. Csillag, E. Lomba, F. Agulló-Rueda, A. R. Landa-Cánovas, L. C. Otero-Díaz, *Chem. Mater.* **2007**, 19, 2304.
- [8] C. Yin, Q. Huang, B. Liu, X. Wang, Y. Xie, L. He, M. Zhang, X. Yang, *Mater. Lett.* **2007**, 61, 4015.
- [9] F. Su, X. S. Zhao, Y. Wang, L. Wang, J. Y. Lee, *J. Mater. Chem.* **2006**, 16, 4413.
- [10] P. Valle-Vigón, M. Sevilla, A. B. Fuerte, *Chem. Mater.* **2010**, 22, 2526.

- [11] Q. Shi, H. Liang, D. Feng, J. Wang, G. D. Stucky, *J. Am. Chem. Soc.* **2008**, 130, 5034.
- [12] J.H. He, H.Y. Kong, R.R. Yang, H. DOU, N. Faraz, L. Wang, C. Feng. *Therm. Sci.* **2012**, 16, 1363.
- [13] K. Tauer, H. Müller, *Colloid Polym. Sci.* **2003**, 281, 52.
- [14] K. Tauer, S. Kosmella, *Polym. Int.* **1993**, 30, 253.
- [15] W. Stöber, A. Fink, *J. Colloid Interface Sci.* **1968**, 26, 62.
- [16] J. Jang, B. Lim, *Adv. Mater.* **2002**, 14, 1390.
- [17] J. P. Zhai, Z. K. Tang, Z. M. Li, I. L. Li, F. Y. Jiang, P. Sheng, X. Hu, *Chem. Mater.* **2006**, 18, 1505.
- [18] M. Choucair, P. Thordarson, J. A. Stride, *Nat. Nanotechnol.* **2009**, 4, 30.
- [19] F. Beguin, R. Setton, *Carbon* **1972**, 10, 539.
- [20] I. Mochida, E. Nakamura, K. Maeda, K. Takeshita, *Carbon* **1976**, 14, 123.
- [21] A. C. Ferrari, J. Robertson, *Phys. Rev. B* **2000**, 61, 14095.
- [22] A. Sadezkya, H. Muckenhuberb, H. Grotheb, R. Niessnera, U. Pöschl, *Carbon* **2005**, 43, 1731.
- [23] P. Ehrburger, A. Addoun, F. Addoun, J.-B. Donnet, *Fuel* **1986**, 65, 1447.
- [24] J. S. Beck, J. C. Vartuli, G. J. Kennedy, C. T. Kresge, W. J. Roth, S. E. Schrammt, *Chem. Mater.* **1994**, 6, 1816.
- [25] R. M. de Silva, V. Palshin, K. M. N. de Silva, L. L. Henry, C. S. S. R.

Kumar, *J. Mater. Chem.* **2008**, 18, 738.

[26] A. Ulman, *Chem. Rev.* **1996**, 96, 1533.

**Chapter 3. Self-assembled Ferrite/Carbon Hybrid Nanosheets for
Lithium-Ion Battery Anodes**

3.1. Introduction

Rapidly growing demand for energy storage devices for portable electronic devices and electric vehicles will require high performance rechargeable batteries. Among the various rechargeable batteries, the lithium-ion battery (LIB) has been most intensively used for its outstanding energy and power density performance [1–3]. Although LIBs have been widely used in a variety of applications, many issues including their energy density, durability, and economic efficiency are still being intensively studied for further improvement. In particular, the development of noble electrode materials with high energy density and cycling stability is one of the hottest topics in the LIB research. Transition-metal oxides are promising high-energy-density materials with their high theoretical capacity ($\sim 1000 \text{ mAh g}^{-1}$), which considerably exceeds that of commercial graphitic anodes (372 mAh g^{-1}) [4,5]. However, low electrical conductivity and poor durability have impeded their use as LIB electrode materials. During charging and discharging of transition-metal oxide anodes, reversible intercalation of Li ions between the lattices occurs through the so-called conversion reaction mechanism [6]. This process causes considerable volume change and reduced

crystallinity of the anode material with prolonged cycling, degrading the anode performance [7,8]. Consequently, transition-metal oxide anode research has been focused on improving the charge transport and mechanical durability.

Nanostructured electrode materials have attracted great interest as a solution to the above-mentioned problems [9-13]. Their nanostructures can provide short path lengths for the transport of electrons and Li ions, resulting in the good conductivity and fast charge/discharge rates. Furthermore, these nanomaterials can withstand mechanical strain during Li ion insertion/desertion better than that of bulk materials. However, due to the high surface-to-volume ratio and high surface free energy of the nanomaterials, undesirable side reactions can occur easily on their surfaces, including electrolyte degradation. Many kinds of metal-oxide/carbon nanocomposites have been investigated to overcome these problems [14–19]. Coating a carbon layer on the surface of metal oxide nanoparticles can reduce the side reactions at the interface between metal oxide and electrolyte. Moreover, good electrical conductivity of carbon can complement the low conductivity of metal oxides. In recent years, several fabrication methods have been reported for metal-oxide/carbon nanocomposites. Heating mixtures of metal salt and carbon

precursors has led to the formation of metal-oxide/carbon composites [20,21]. However, the products were usually poor quality in both uniformity and homogeneity of the composite structure [20]. Furthermore, the complicated synthetic process [21], comprising multiple reactions using autoclaves, lowers productivity compared to other single-step processes. Consequently, new easy fabrication methods are required for metal-oxide/carbon nanocomposites. Very recently, the Archer group reported an in situ synthesis of nanoparticles embedded in a porous carbon matrix through a miniemulsion polymerization process, which exhibited stable electrochemical cycling performance [22,23]. Piao et al. have developed a thermal treatment method, called as “wrap-bake-peel process,” which can preserve the sizes and shapes of the nanocrystals during thermal treatment [24].

The controlled assembly of uniform-sized nanocrystals has been attracted great attention because well-aligned ensembles of inorganic nanocrystals often exhibit interesting collective properties that are different from those displayed by individual nanocrystals and bulk samples [25-33]. Various Synthetic approaches [34-39] were developed for periodically ordered arrays of the synthesized nanoparticles including “evaporation-driven” methods [36,37] and “destabilization-driven”

approaches [38,39]. However, as far as I know, there are no reports about synthesis and self assembly processes were simultaneously achieved to nanoparticle/carbon hybrid structure with long range ordered arrays. Herein, a single-step method for the direct preparation of self-assembled ferrite/carbon hybrid nanosheets, and their applications to high performance lithium ion battery anodes were presented.

3.2. Experimental Section

3.2.1. Chemicals

Iron(III) chloride hexahydrate ($\text{FeCl}_3 \cdot 6\text{H}_2\text{O}$ 98%), manganese(II) chloride tetrahydrate ($\text{MnCl}_2 \cdot 4\text{H}_2\text{O}$, Aldrich, 98%) and sodium sulfate powder (Na_2SO_4 , 98%). were purchased from Aldrich Chemical Co. Sodium oleate (95%). was purchased from TCI.

3.2.2. Characterization methods

Transmission electron microscopy (TEM) images were obtained using a JEOL EM-2100F microscope, and field-emission scanning electron microscopic (FE-SEM) images were obtained with a Hitachi S-4800 microscope. X-ray diffraction (XRD) analysis was carried out using a Rigaku Dmax 2500 diffractometer. Raman spectrum was obtained by using MonoRa500i. Electrical conductivity measurement was performed by using a CMT 100 MP four-point probe station.

3.2.3. Preparation of 16-nm iron-oxide/carbon hybrid nanosheets

In a typical synthesis, 0.36 g of iron(III) chloride hexahydrate ($\text{FeCl}_3 \cdot 6\text{H}_2\text{O}$, 1.33 mmol) was dissolved in 1.0 mL of DI water and then

mixed with 1.22 g of sodium oleate (4 mmol). The resulting mixture was aged at 85 °C for 3 hr, and then was mixed with 10 g of sodium sulfate powder (Na₂SO₄). The mixture was heated to 600 °C at the heating rate of 10 °C min⁻¹ under N₂ atmosphere and then kept at that temperature for 3 h. After cooling, the product was washed with DI water and dried at 100 °C for 6 h

3.2.4. Preparation of 30-nm iron-oxide/carbon nanosheets

In a typical synthesis, 0.36 g of iron(III) chloride hexahydrate (FeCl₃·6H₂O, 1.33 mmol) was dissolved in 1.0 mL of DI water and then mixed with 1.22 g of sodium oleate (4 mmol). This mixture was aged at 85 °C for 3 hr. The resulting material was mixed with 10 g of sodium sulfate powder (Na₂SO₄). The mixture was heated to 600 °C at the heating rate of 5 °C min⁻¹ under N₂ atmosphere, and then kept at that temperature for 3 h. After cooling, the product was washed with DI water and dried at 100 °C for 6 h.

3.2.5. Preparation of 3-D nanocomposites

The procedure was the same as the preparation of ferrite/carbon hybrid nanosheets described above except that sodium sulfate powder was not

added.

3.2.6. Preparation of 10-nm manganese-ferrite/carbon nanosheets

In a typical synthesis, 0.087 g of manganese(II) chloride tetrahydrate ($\text{MnCl}_2 \cdot 4\text{H}_2\text{O}$, 0.44 mmol) and 0.24 g of iron(III) chloride hexahydrate ($\text{FeCl}_3 \cdot 6\text{H}_2\text{O}$, 0.89 mmol, Aldrich, 98%) were dissolved in 1.0 mL DI water and then mixed with 1.22 g of sodium oleate (4 mmol). This mixture was aged at 85 °C for 3 h. The subsequent heating and post-treatment procedures were the same as for iron-oxide/carbon nanosheets described above, except for the heating rate, which was 5 °C min⁻¹.

3.2.7. Preparation of electrodes for LIBs

A working electrode was prepared by following scheme. A dry powder of the nanocomposite (active material), super P (carbon additive), and poly(vinylidene fluoride) (binder) (85:5:10) were mixed and coated on a piece of copper foil (current collector). After removing the residual moisture by drying in a vacuum oven at 120 °C for 12 h, the electrode plate was pressed to improve the inter-particle contact and to reinforce adhesion between particles and the current collector. The electrochemical tests were performed by using a coin-type

electrochemical cell (2032-type) which was fabricated with lithium foils as the counter and reference electrodes and 1.0 M LiPF₆ dissolved in a mixture of ethylene carbonate (EC) and dimethyl carbonate (DMC) (1:2 in vol. ratio) as the electrolyte. In order to cycle the coin-type electrochemical cells, they were discharged with constant current of 100 mA g⁻¹ to 0.05 V (vs. Li/Li⁺) and constant voltage at 0.05 V (vs. Li/Li⁺) to 50 mA g⁻¹ and charged with constant current of 100 mA g⁻¹ to 3.0 V (vs. Li/Li⁺). In the rate capability test, the lithiation current density was fixed at 100 mA g⁻¹, but the de-lithiation current density was changed every five cycles according to this sequence of values: 100, 200, 500, 1000, 3000, and 5000 mA g⁻¹.

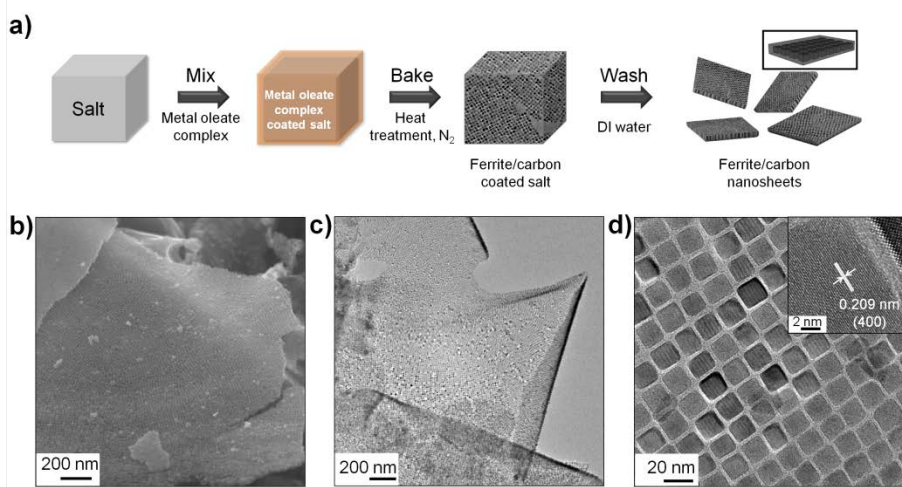


Figure 3.1. (a) Schematic representation of the preparation of ferrite/carbon nanosheets by salt-template process. (b) FESEM image and (c-d) TEM images of the 16-nm iron-oxide/carbon nanosheets. The inset shows a HRTEM image demonstrating the highly crystalline nature of the nanosheets.

3.3. Results and Discussion

The overall synthetic procedure is depicted in Figure 3.1a. In the direct synthesis of the ferrite/carbon hybrid nanosheets, I adopted two strategies. First, the surface of thermally stable salt particles was used as the template for the 2-D nanostructure. Second, metal-oleate complex was used as the precursor of both ferrite [40-43] and carbon. Upon heating under inert atmosphere, the coating layer on the surface of the salt particles was converted to a carbon sheet of uniform thickness. In the synthesis, an aqueous solution of metal chloride and sodium oleate were mixed together, whereupon sodium sulfate was added and then ground mechanically until it became a fine powder. During this process, in situ formed metal-oleate complex was uniformly coated on the surface of sodium sulfate particles. This mixture was heated at $\sim 600\text{ }^{\circ}\text{C}$ under inert atmosphere to form 2-D ferrite/carbon hybrid nanosheet structures. Finally, the hybrid nanosheets were separated by dissolving sodium sulfate particles in deionized (DI) water.

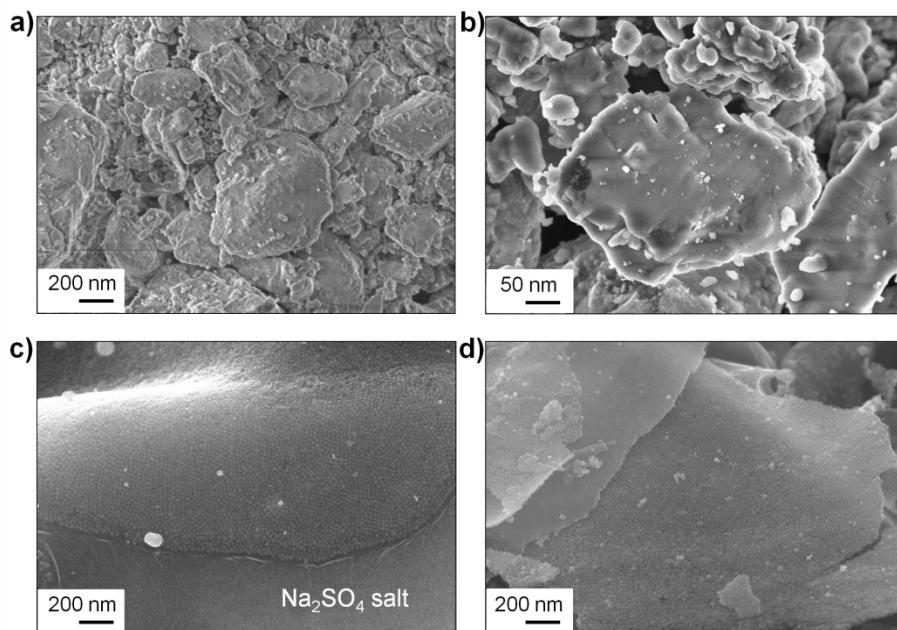


Figure 3.2. SEM images of (a,b) Na_2SO_4 salt, (c) 16-nm iron oxide/carbon nanosheet on Na_2SO_4 salt, and (d) 16-nm iron oxide/carbon nanosheet after removal of sodium sulfate salt powder.

The morphology of the hybrid nanosheets was analysed by scanning electron microscopy (SEM) and transmission electron microscopy (TEM). In Figure 3.1, it is shown that well-ordered uniform iron oxide nanocubes were embedded in a carbon sheet. The mean size and relative standard deviation of the nanocubes were measured to be 16 nm and 5.9%, respectively (16-nm iron-oxide/carbon nanosheets). Due to their size and shape uniformity, they were assembled in a highly ordered 2-D array that was evenly distributed across the carbon matrix, and each nanocrystal was perfectly concealed within a carbon layer which was a few nanometers thick. The carbon sheet itself was very thin, and the surface profile of the carbon sheet reflects roughly the embedded array of nanocubes, as shown in the SEM image (Figure 3.1b). SEM analysis on as-prepared nanosheets before removing the salt powder revealed that they were actually formed on the surface of the salt particles (Figure 3.2), which confirms the role of salt particles as the template for the 2-D structure. Furthermore, the dimensions of the 2-D nanocomposites were on the micrometer scale, which is roughly the same as the size of a flat surface of the salt particles. As shown in the inset of Figure 3.1d, the nanocubes were highly crystalline and *d*-spacings of the lattice fringes indicate that the faces of the nanocubes are {100} planes of ferrite

structure (Figure 3.3). The evolution of the cubic shape is attributed to the relative stabilization of the {100} face compared to the {111} and {110} faces [44].

The size and shape of the iron oxide nanocrystals were controlled by the heating rate and the temperature. When the heating rate was $5\text{ }^{\circ}\text{C min}^{-1}$, the size of the iron oxide nanocrystals was increased to $\sim 30\text{ nm}$ (30-nm iron-oxide/carbon nanosheets), and the shape became more spherical compared to the 16 nm-sized nanocubes (Figure 3.4a,b). In general, when the heating rate was higher or lower than $10\text{ }^{\circ}\text{C min}^{-1}$, the size distribution of the nanocrystals became broadened with the mean size of $> 30\text{ nm}$ (Figure 3.5,3.6). The size of the iron oxide nanocrystals was also affected by the heating temperature (Figure 3.7). According to TEM analysis, the formation of iron oxide nanocrystals was initiated at $\sim 250\text{ }^{\circ}\text{C}$. Considering that carbonization of organic precursors usually takes place at temperatures higher than $400\text{ }^{\circ}\text{C}$, it is likely that iron oxide nanocrystals were formed and assembled into a 2-D array as the temperature was increased from $250\text{ }^{\circ}\text{C}$ to $400\text{ }^{\circ}\text{C}$, which is followed by the conversion of surfactant layer to carbon phase.

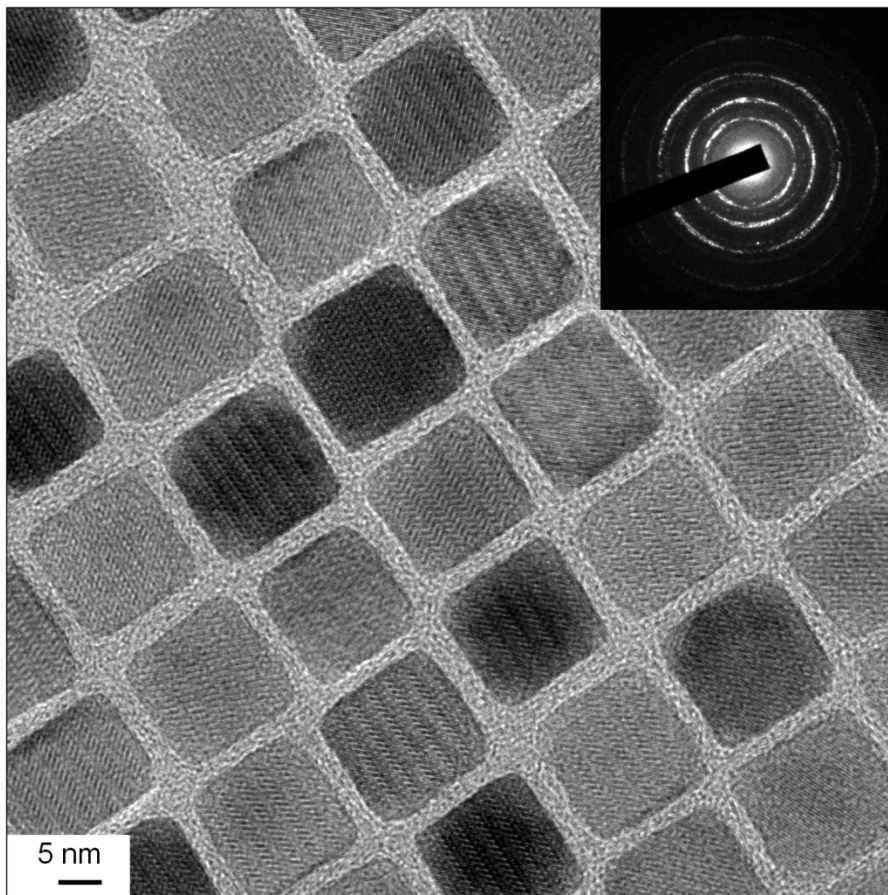


Figure 3.3. High magnification TEM image of the 16-nm iron-oxide/carbon nanosheet. The inset figure represents electron diffraction patterns of the 16 nm iron oxide nanoparticles.

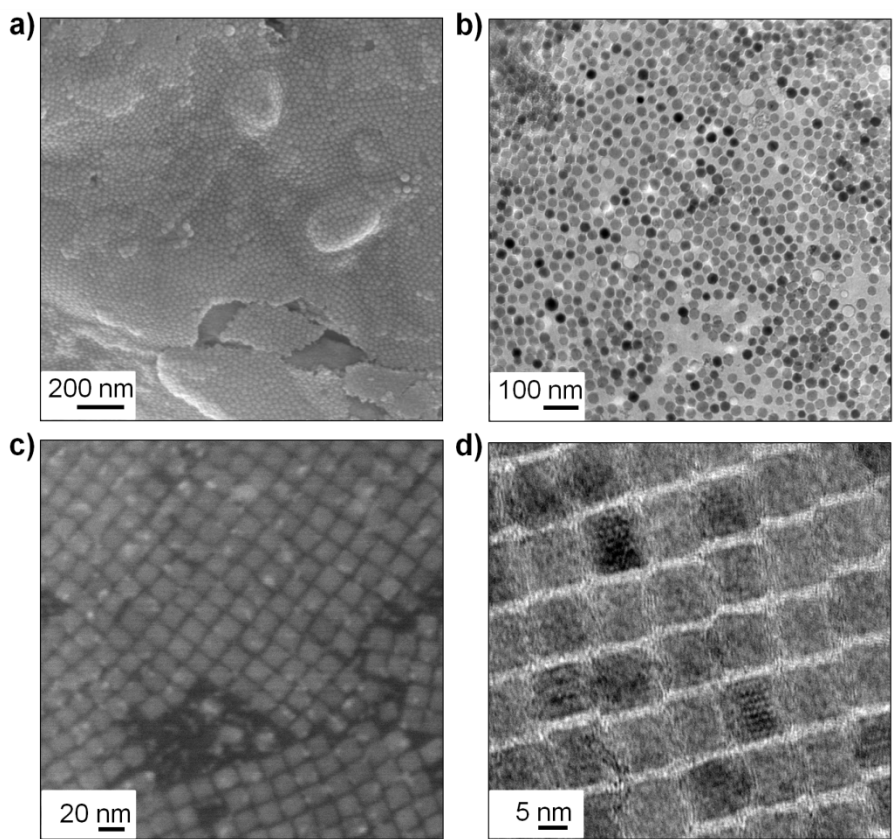


Figure 3.4. (a) FESEM image and (b) TEM image of the 30-nm iron-oxide/carbon nanosheets, (c) FESEM image and (d) TEM image of the 10-nm manganese-ferrite/carbon nanosheets.

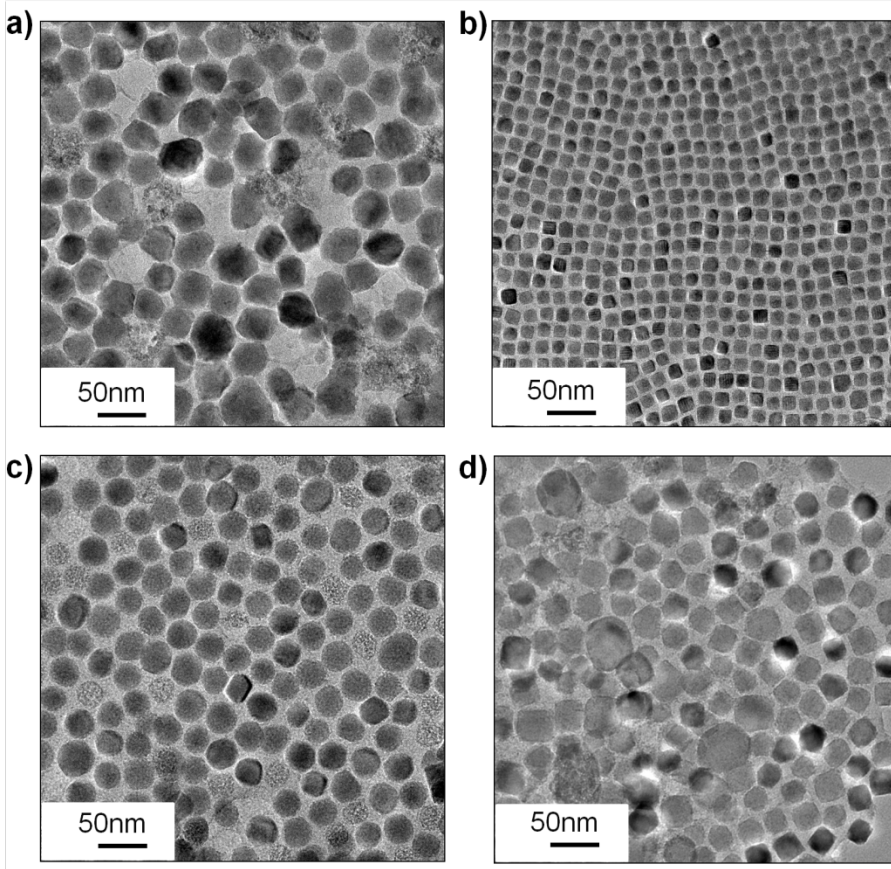


Figure 3.5. TEM images of 30-nm iron-oxide/carbon nanosheet prepared at the heating rates of (a) 20 °C min⁻¹, (b) 10 °C min⁻¹, (c) 5 °C min⁻¹, and (d) 2.5 °C min⁻¹. Annealing temperature was fixed at 600 °C.

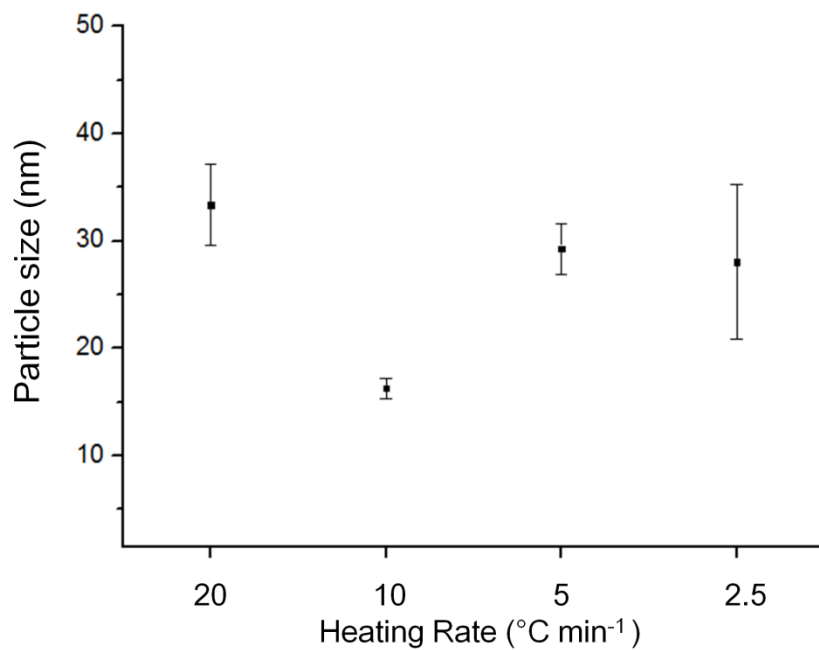


Figure 3.6. Size distributions of the iron oxide nanocrystals measured on TEM images in Figure 3.5.

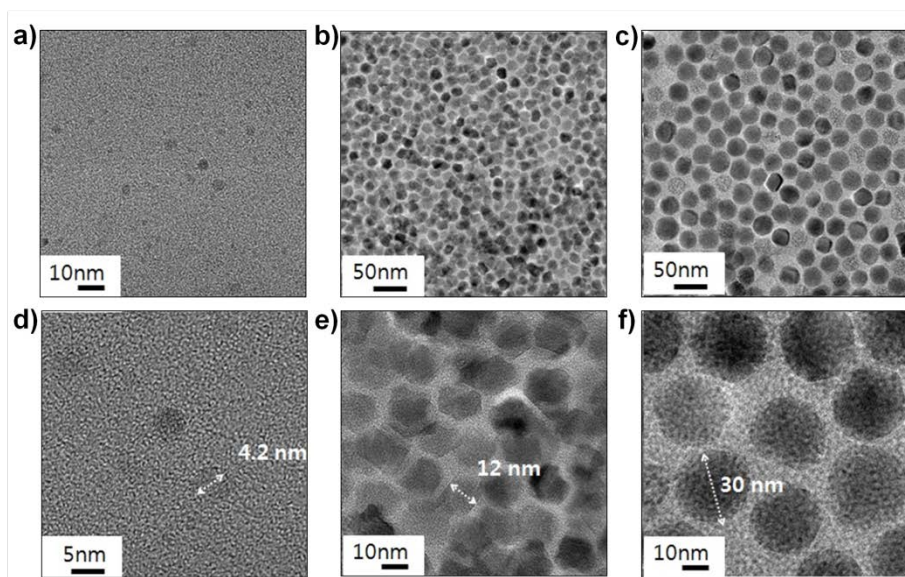


Figure 3.7. TEM images of the iron-oxide/carbon hybrid nanosheets prepared at different annealing temperature of (a), (d) 250 °C, (b), (e) 300 °C, and (c), (f) 600 °C. Heating rate was fixed at 5 °C min⁻¹.

The current synthetic process is easy to scale up, and when I ran the reaction using 13.3 mmol of iron oleate precursor, 1.3 g of the iron-oxide/carbon nanocomposite was obtained (Figure 3.8). The synthetic procedure for iron-oxide/carbon nanocomposite can be easily extended to other ferrites. Using a mixture of manganese(II) and iron(III) chloride, manganese-ferrite/carbon nanosheets were obtained through the optimized heating rate of 5 °C min⁻¹. As shown in Figure 3.4c, the 2-D array of manganese-ferrite/carbon nanosheets was as uniform as the array of 16-nm iron-oxide/carbon nanosheets in Figure 3.1, and the mean size of the manganese-ferrite nanocrystals was 10 nm (10-nm manganese-ferrite/carbon nanosheets). The composition of Mn and Fe in the nanocrystals was controlled by varying the ratio of manganese(II) chloride to iron(III) chloride added during the formation of metal-oleate complexes (Figure 3.9).

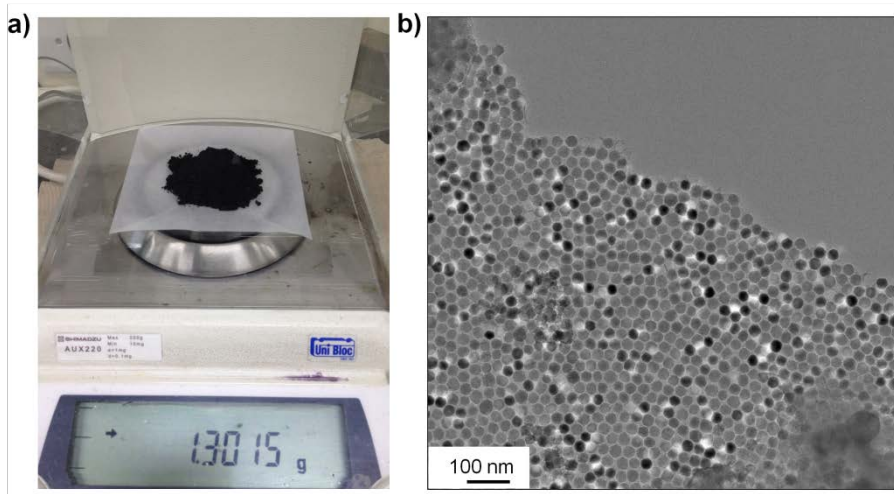


Figure 3.8. Large scale synthesis of 30-nm iron-oxide/carbon nanosheet.

(a) A photograph showing ~1.3 g of the synthesized 30-nm iron-oxide/carbon nanosheet nanosheets. (b) TEM image of 30-nm iron-oxide/carbon nanosheet in large-scale.

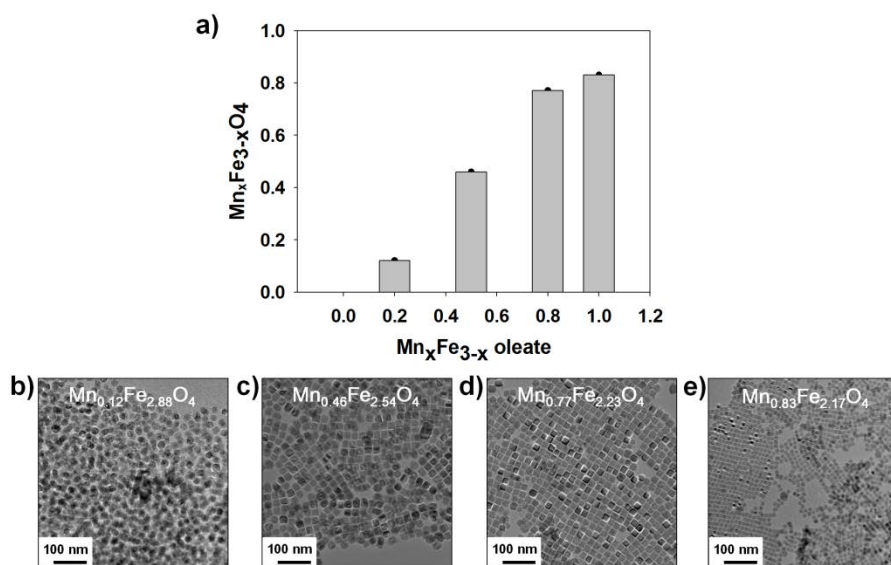


Figure 3.9. (a) Mn to Fe ratio in manganese ferrite from was determined by inductively coupled plasma auger electron spectrometry (ICP-AES). (b-e) TEM images of manganese-ferrite/carbon nanosheets synthesized using various ratios of manganese(II) and iron(III) chlorides in the oleate synthesis step.

The crystal structures of the metal oxide nanocrystals in the nanocomposites were investigated by powder X-ray diffraction (XRD) measurement (Figure 3.10). The XRD patterns of the 16 nm- and 30 nm-sized iron oxide nanocrystals in the composite matched well with the standard pattern of maghemite ($\gamma\text{-Fe}_2\text{O}_3$, JCPDS 39-1346) and magnetite (Fe_3O_4 , JCPDS 85-1436), respectively. The size-dependent transition of iron oxide nanocrystals from $\gamma\text{-Fe}_2\text{O}_3$ to Fe_3O_4 has been reported previously [28]. The XRD pattern of manganese ferrite nanocrystals in the composite could be assigned to the standard of manganese ferrite (MnFe_2O_4 , JCPDS 73-1964).

It is worth emphasizing here that the carbon nanostructure of our composite material is very unique. To observe its morphology in detail, I removed embedded iron oxide nanocubes via acid etching. When the ferrite/carbon nanosheets were refluxed in 2.5 M HNO_3 solution for 1 h, hollow 2-D carbon nanoframes were obtained. The 2-D nanofoam sheets were free-standing and well-dispersible in various solvents including ethanol and water. Interestingly, in the TEM images (Figure 3.11), the carbon nanostructure remained intact after etching, indicating its mechanical rigidity, and regularly-spaced carbon networks extended continuously throughout the whole sheet.

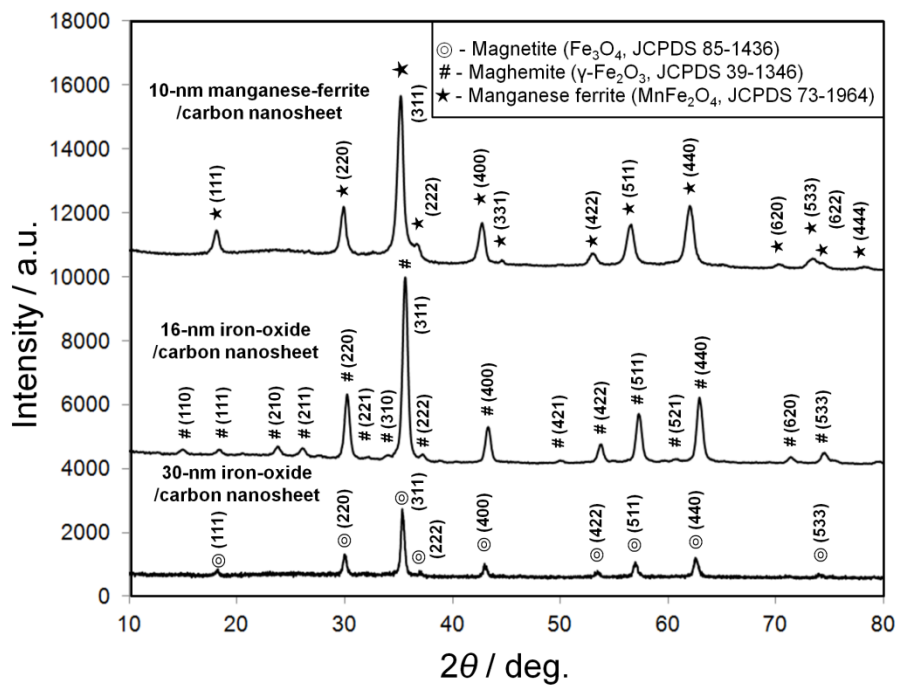


Figure 3.10. XRD patterns of the ferrite/carbon hybrid nanosheets.

Before investigating the electrochemical properties of the nanosheets, I prepared 3-dimensional iron-oxide/carbon nanocomposites (3-D nanocomposites) for comparison with the ferrite/carbon nanosheets (Figure 3.12). The synthetic procedure was the same as that for the 30-nm iron-oxide/carbon nanosheets except that salt powder was not added before the heat treatment. Without the template, carbon agglomerates embedded with spherical iron oxide nanocrystals with a diameter of ~40 nm were generated. The array of nanocrystals in the composite was less ordered than in the ferrite/carbon nanosheets due to the broad size distribution. The carbon contents (Table 3.1) of the 16-nm iron-oxide/carbon nanosheets, 30-nm iron-oxide/carbon nanosheets, and 3-D nanocomposites were 32–35 wt%, 44 wt%, and 25 wt%, respectively. To reduce carbon contents of the hybrid nanocomposites, I changed the precursor from iron(III) oleate to iron(III) carboxylates with shorter hydrocarbon chain length, i.e., iron(III) caprylate and iron(III) laurate. However, these precursors were decomposed before the carbonization process, resulting in the irregular shaped nanoparticles without 2-D assembled structure (Figure 3.13, Table 3.2).

The characteristics of carbon in the nanosheets were characterized by electrical conductivity measurements and Raman spectroscopy.

Electrical conductivity of the ferrite/carbon nanosheets was measured to be $4 \times 10^{-3} \text{ S cm}^{-1}$. The Raman spectrum of the ferrite/carbon nanosheets showed two distinguishable peaks at around 1335 cm^{-1} (D band) and 1605 cm^{-1} (G band) with similar intensity (Figure 3.14), indicating that the obtained carbon materials were disordered nanocrystalline graphite [45,46]

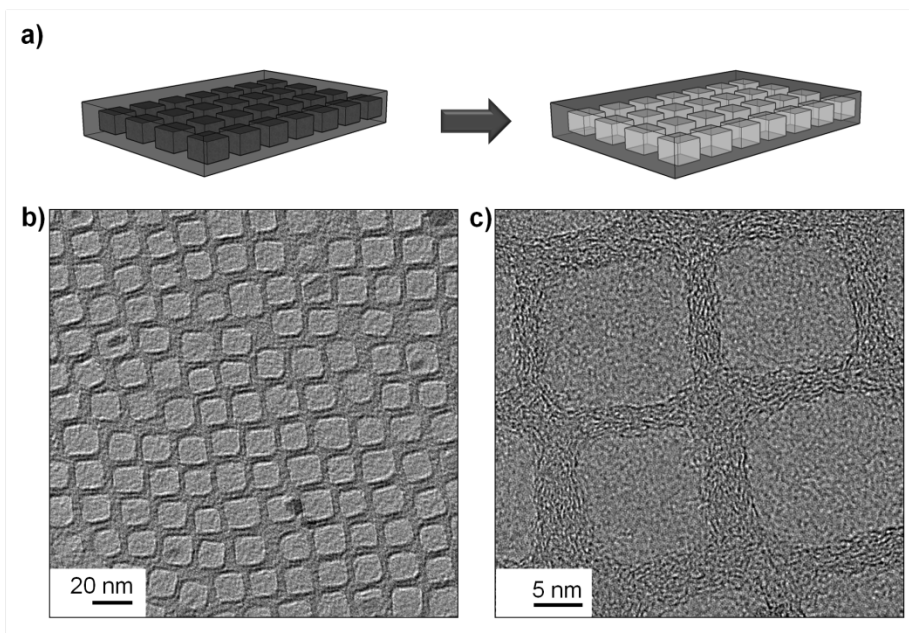


Figure 3.11. (a) Schematic representation of the preparation of the carbon nanofoams. (b-c) TEM images of the carbon nanofoam after removal of the 16 nm iron oxide nanocrystals from the nanosheets.

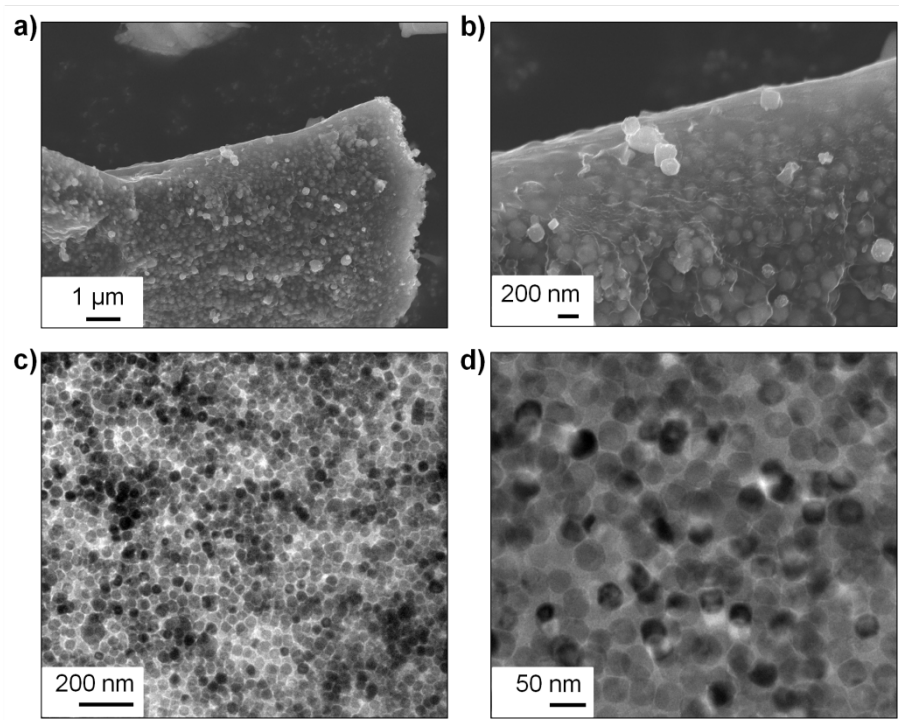


Figure 3.12. (a,b) FESEM and (c,d) TEM images of 3-D nanocomposite.

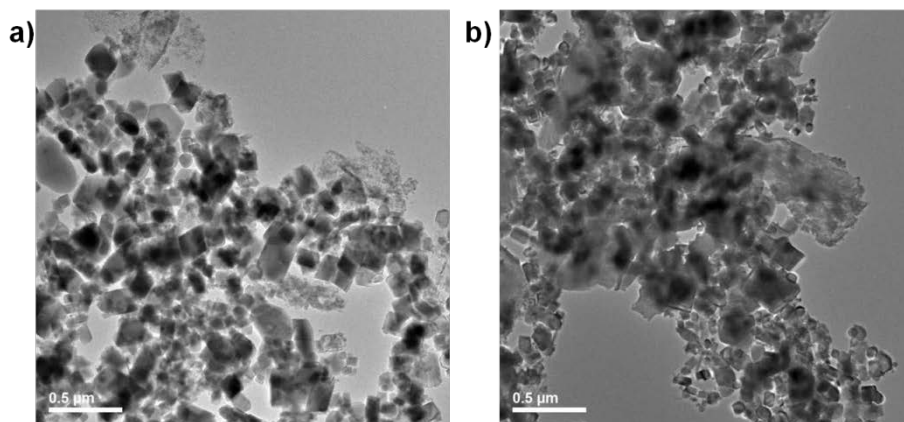


Figure 3.13. TEM images of iron-oxide/carbon composites by using (a) iron caprylate and (b) iron laurate as the precursors.

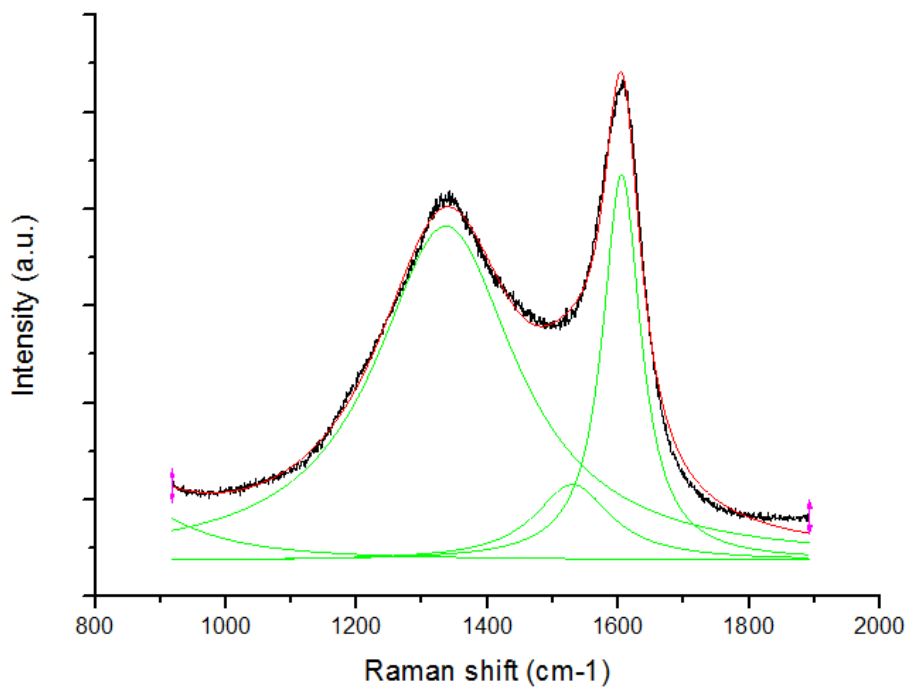


Figure 3.14. Raman spectrum of 30-nm iron-oxide/carbon nanosheets.

Table 3.1. Ferrite and carbon contents of ferrite/carbon hybrid nanosheets based on CHN analysis.

Composites	Carbon Contents (%)	Ferrite Contents (%)
6-nm iron-oxide/carbon nanosheet	32	68
30-nm iron-oxide/carbon nanosheet	44	52
3-D nanocomposite	25	75
10-nm manganese-ferrite/carbon nanosheet	35	65

Table 3.2. Ferrite and carbon contents of ferrite/carbon composites using (a) iron caprylate and (b) ironlaurate as the precursors.

Composites (Precursor)	Carbon Contents (%)	Ferrite Contents (%)
Iron(caprylate) ₃	1	99
Iron(laurate) ₃	1	99

As a demonstration of the ferrite/carbon nanosheets as LIB anode materials, electrochemical tests were carried out in a coin type cell assembly. First, galvanostatic discharge/charge voltage profiles were obtained at a current density of 100 mA g^{-1} (Figure 3.15). In the first cycle, the profiles of the four electrodes, 16-nm iron-oxide/carbon nanosheets, 30-nm iron-oxide/carbon nanosheets, 10-nm manganese-ferrite/carbon nanosheets, and 3-D nanocomposites, appeared similar. Plateaus at about 1.6 and 0.8 V versus Li^+/Li in the lithiation and de-lithiation curves are a well-known signature of the conversion reactions of transition-metal oxides [6]. However, the specific capacity of each electrode evolved quite distinctly from the others in the subsequent 20 cycles. The capacities of all the ferrite/carbon nanosheet electrodes stabilized after 10 cycles, while the capacity of the 3-D nanocomposite electrode faded rapidly. In Figure 3.16a, the de-lithiation capacities of the electrodes were plotted in terms of cycling number. In the plot, the de-lithiation capacities of the ferrite/carbon nanosheet electrodes were kept near or above 600 mAh g^{-1} after 50 cycles. On the other hand, the capacity of the 3-D composite electrode was reduced considerably to 323 mAh g^{-1} . These data clearly show the contribution of 2-D nanosheet morphology to capacity retention during cycling. The rate capability of

the electrodes is also shown in Figure 3.16b. At a very high rate of 5000 mA g⁻¹, 81.5% of original capacity was retained for the manganese-ferrite/carbon nanosheets, whereas 68.7%, 56.8%, and 41.6% were retained for 16-nm iron-oxide/carbon nanosheets, 30-nm iron-oxide/carbon nanosheets, and 3-D nanocomposites, respectively.

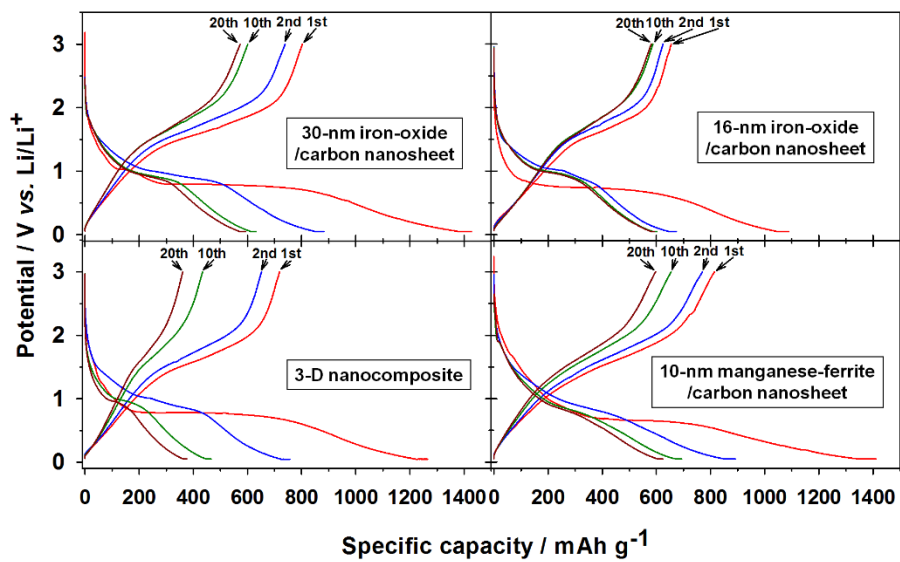


Figure 3.15. Galvanostatic discharge (lithiation, downward) and charge (de-lithiation, upward) voltage profiles.

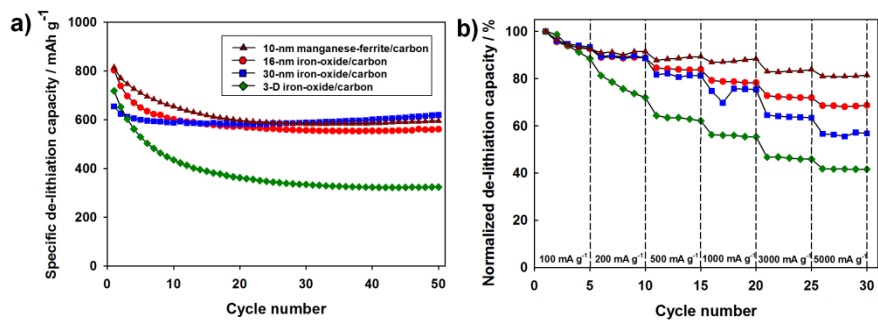


Figure 3.16. (a) Lithiation/de-lithiation capacities, and (b) rate performance according to the cycle number of the ferrite/carbon nanosheet electrodes.

In electrochemical cycling of the ferrite/carbon nanocomposites, considerable change in the volume of metal oxide takes place due to the conversion reactions which lower the integrity of the electrode structure and increase the internal resistance. It has been reported that the presence of carbon coating can reduce mechanical deformation by buffering the volume change of the active materials in the electrode [47,48]. Comparing the ferrite/carbon nanosheets and 3-D nanocomposites, well-ordered ferrite/carbon nanosheets have several advantages in terms of resistance to mechanical deformation. The self-assembled nanocrystal structure seems to induce the regularly-spaced carbon walls between the nanocrystals, providing high tensile strength in the vertical direction of the carbon sheet. In addition, ferrite/carbon nanosheets have more room to expand in this direction than 3-D nanocomposites, which can provide a buffer for the volume change of the nanocrystals. As a result, these structural factors can contribute to good cycle performance of the ferrite/carbon nanosheets, as shown in Figure 3.16a. To investigate the mechanical deformation of the ferrite/carbon nanosheets during the electrochemical cycling, TEM observations were made on the nanosheet electrodes after 10th charge/discharge cycling at a rate of 100 mA g^{-1} (Figure 3.17). The ferrite nanoparticles maintained the shape and size,

and the assembled nanosheet structure was sustained without peeling off. The encapsulating carbon shells seem to help to maintain the structure of ferrite/carbon nanosheet electrodes. The rate capacity of the electrodes is affected by the diffusion of lithium ions from the electrolyte to the active material. In Figure 3.16b, the ferrite/carbon nanosheets show much better performance than the 3-D nanocomposite. This superior electrochemical performance of the ferrite/carbon nanosheets is due to their short diffusion path and large accessible surface for the effective insertion of lithium ions. Moreover, the size of the ferrite nanocrystals strongly affected the electrochemical performance at high charging/discharging rates. Smaller-sized ferrite nanocrystals were more efficient for fast diffusion process, and the coulombic efficiency of the nanosheets seem to be less affected by the decomposition of electrolytes on the surface of electrodes because carbon shell protected the ferrite nanocrystals [49]. Furthermore, the large coulombic capacity at high discharge rates seems to be resulted from the uniform-sized ferrite nanoparticles [50].

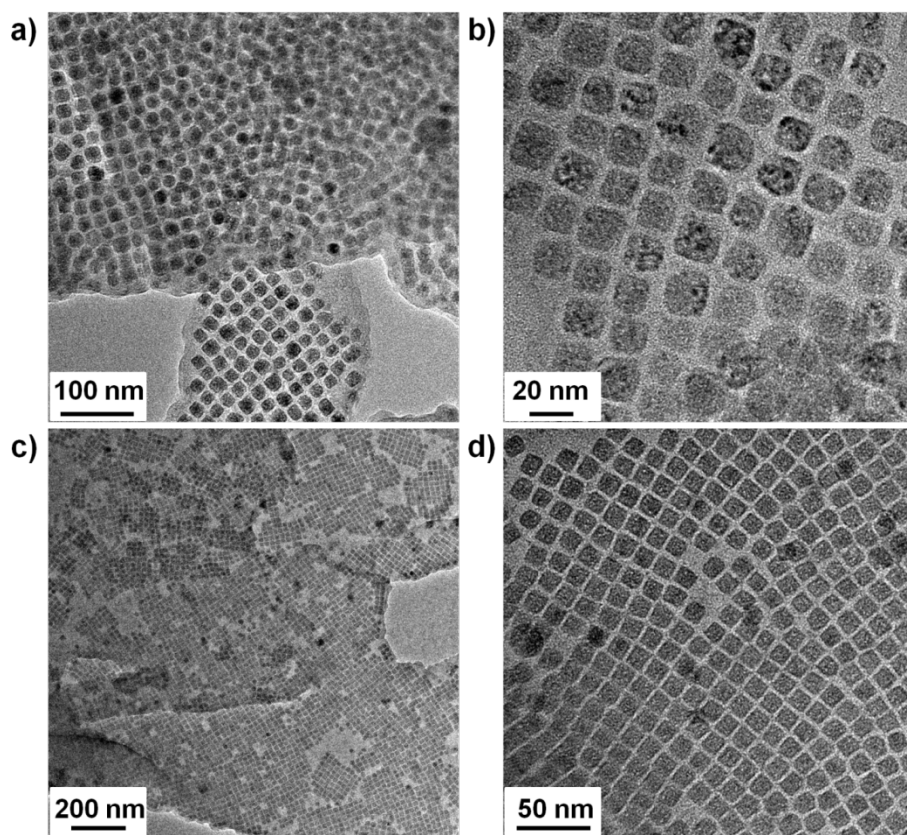


Figure 3.17. TEM images of (a, b) 16-nm iron-oxide/carbon nanosheets, and (c, d) 10-nm manganese-ferrite/carbon nanosheets after 10th charge/discharge cycling at a rate of 100 mA g^{-1} .

3.4. Conclusion

With the ever-increasing energy needs of the world, the development of next-generation technology for energy conversion and storage is one of the most pressing challenges facing our civilization. The potential for lithium-ion batteries to help fill this need could be greatly enhanced by advances in the anode materials.

Consequently, highly monodisperse metal-oxide nanocrystals and carbon materials were synthesized simultaneously through a single heating procedure using metal-oleate complex as the precursors for both the metal oxide and carbon. A 2-D nanostructure was obtained by using sodium sulphate salt powder as a template. In comparison with a 3-D composite, the prepared iron-oxide/carbon and manganese-ferrite/carbon 2-D nanocomposites exhibited good cycling stability and high capacity.

These synthetic procedures are not only easily scalable for mass production but also extensible to various 2-D inorganic-nanocrystal/carbon nanocomposites that can potentially be applied to practical energy storage and conversion devices.

3.5. References

- [1] M. Armand, J.-M. Tarascon, *Nature* **2008**, 451, 652.
- [2] K. Kang, Y. S. Meng, J. Bréger, C. P. Grey, G. Ceder, *Science* **2006**, 311, 977.
- [3] G. Ceder, *MRS Bull.* **2010**, 35, 693.
- [4] S. K. Behera, *J. Power Sources* **2011**, 196, 8669.
- [5] J. Ma, J. Lian, X. Duan, X. Liu, W. Zheng, *J. Phys. Chem. C* **2010**, 114, 10671.
- [6] P. Poizot, S. Laruelle, S. Grugeon, L. Dupont, J.-M. Tarascon, *Nature* **2000**, 407, 496.
- [7] J. Cabana, L. Monconduit, D. Larcher, M.R. Palacín, *Adv. Mater.* **2010**, 22, E170.
- [8] M. G. Kim, J. Cho, *Adv. Funct. Mater.* **2009**, 19, 1497.
- [9] A. S. Aricò, P. G. Bruce, B. Scrosati, J.-M. Tarascon, W. van Schalkwijk, *Nat. Mater.* **2005**, 4, 366.
- [10] P. G. Bruce, B. Scrosati, J.-M. Tarascon, *Angew. Chem. Int. Ed.* **2008**, 47, 2930.
- [11] C. K. Chan, H. Peng, G. Liu, K. McIlwrath, X. F. Zhang, R. A. Huggins, Y. Cui, *Nat. Nanotechnol.* **2008**, 3, 31.

- [12] X. W. Lou, D. Deng, J. Y. Lee, J. Feng, L. A. Archer, *Adv. Mater.* **2008**, 20, 258.
- [13] H. Wang, L.-F. Cui, Y. Yang, H. S. Casalongue, J. T. Robinson, Y. Liang, Y. Cui, H. Dai. *J. Am. Chem. Soc.* **2010**, 132, 13978.
- [14] Y.-S. Hu, R. Demir-Cakan, M.-M. Titirici, J.-O. Müller, R. Schlögl, M. Antonietti, J. Maier, *Angew. Chem. Int. Ed.* **2008**, 47, 1645.
- [15] H. Kim, J. Cho, *Nano Lett.* **2008**, 8, 3688.
- [16] X. W. Lou, C. M. Li, L. A. Archer, *Adv. Mater.* **2009**, 21, 2536.
- [17] X.-L. Wu, L.-Y. Jiang, F.-F. Cao, Y.-G. Guo, L.-J. Wan, *Adv. Mater.* **2009**, 21, 2710.
- [18] Y. Piao, H. S. Kim, Y.-E. Sung, T. Hyeon, *Chem. Commun.* **2010**, 46, 118.
- [19] C. Ban, Z. Wu, D. T. Gillaspie, L. Chen, Y. Yan, J. L. Blackburn, A. C. Dillon, *Adv. Mater.* **2010**, 22, E145.
- [20] B. T. Hang, I. Watanabe, T. Doi, S. Okada, J.-I. Yamaki, *J. Power Sources* **2006**, 161, 1281.
- [21] W.-M. Zhang, X.-L. Wu, J.-S. Hu, Y.-G. Guo, L.-J. Wan, *Adv. Funct. Mater.* **2008**, 18, 3941.
- [22] Z. Yang, J. Shen, N. Jayaprakash, L. A. Archer, *Energy Environ. Sci.* **2012**, 5, 7025.
- [23] Z. Yang, J. Shen, L. A. Archer, *J. Mater. Chem.* **2011**, 21, 11092.

- [24] Y. Piao, J. Kim, H. B. Na, D. Kim, J. S. Baek, M. K. Ko, J. H. Lee, M. Shokouhimehr, T. Hyeon, *Nat. Mater.* **2008**, 7, 242.
- [25] S. Mann, *Nat. Mater.* **2009**, 8, 781.
- [26] P. Podsiadlo, G. Krylova, B. Lee, K. Critchley, D. J. Gosztola, D. V. Talapin, P. D. Ashby, E. V. Shevchenko, *J. Am. Chem. Soc.* **2010**, 132, 8953.
- [27] Z. Nie, A. Petukhova, E. Kumacheva, *Nat. Nanotechnol.* **2010**, 5, 15.
- [28] E. V. Shevchenko, M. Ringler, A. Schwemer, D. V. Talapin, T. A. Klar, A. L. Rogach, J. Feldmann, A. P. Alivisatos, *J. Am. Chem. Soc.* **2008**, 130, 3274.
- [29] S. Sun, C. B. Murray, D. Weller, L. Folks, A. Moser, *Science* **2000**, 287, 1989.
- [30] D. V. Talapin, E. V. Shevchenko, M. I. Bodnarchuk, X. Ye, J. Chen, C. B. Murray, *Nature* **2009**, 461, 964.
- [31] F. Li, D. P. Josephson, A. Stein, *Angew. Chem., Int. Ed.* **2011**, 50, 360.
- [32] Y. Nagaoka, O. Chen, Z. Wang, Y. C. Cao, *J. Am. Chem. Soc.* **2012**, 134, 2868.
- [33] M. I. Bodnarchuk, M. V. Kovalenko, W. Heiss, D. V. Talapin, *J. Am. Chem. Soc.* **2010**, 132, 11967.
- [34] A. Dong, J. Chen, P. M. Vora, J. M. Kikkawa, C. B. Murray, *Nature* **2010**, 466, 474.

- [35] A Dong, X. Ye, J. Chen, C. B. Murray, *Nano Lett.* **2011**, 11, 1804.
- [36] E. V. Shevchenko, D. V. Talapin, N. A. Kotov, S. O'Brien, C. B. Murray, *Nature* **2006**, 439, 55.
- [37] M. I. Bodnarchuk, E. V. Shevchenko, D. V. Talapin, *J. Am. Chem. Soc.* **2011**, 133, 20837.
- [38] S. M. Rupich, E. V. Shevchenko, M. I. Bodnarchuk, B. Lee, D. V. Talapin, *J. Am. Chem. Soc.* **2009**, 132, 289.
- [39] E. V. Shevchenko, D. V. Talapin, A. L. Rogach, A. Kornowski, M. Haase, H. Weller, *J. Am. Chem. Soc.* **2002**, 124, 11480.
- [40] J. Park, K. An, Y. Hwang, J.-G. Park, H.-J. Noh, J.-Y. Kim, J.-H. Park, N.-M. Hwang, T. Hyeon, *Nat. Mater.* **2004**, 3, 891.
- [41] S. G. Kwon, Y. Piao, J. Park, S. Angappane, Y. Jo, N.-M. Hwang., J.-G. Park, T. Hyeon, *J. Am. Chem. Soc.* **2007**, 129, 12571.
- [42] H. Zeng, P. M. Rice, S. X. Wang, S. Sun, *J. Am. Chem. Soc.* **2004**, 126, 11458.
- [43] W. W. Yu, J. C. Falkner, C. T. Yavuz, V. L. Colvin, *Chem. Commun.* **2004**, 2306.
- [44] J. Cheon, N.-J. Kang, S.-M. Lee, J.-H. Lee, J.-H. Yoon, S. J. Oh, *J. Am. Chem. Soc.* **2004**, 126, 1950
- [45] A. C. Ferrari, J. Robertson, *Phys. Rev. B* **2000**, 61, 14095.

- [46] A. Sadezkya, H. Muckenhuberb, H. Grotheb, R. Niessnera, U. Pöschl, *Carbon* **2005**, 43, 1731.
- [47] J. Kim, M. K. Chung, B. H. Ka, J. H. Ku, S. Park, J. Ryu, S. M. Oh, *J. Electrochem. Soc.* **2010**, 157, A412.
- [48] X. Zhu, Y. Zhu, S. Murali, M. D. Stoller, R. S. Ruoff, *ACS Nano* **2011**, 5, 3333.
- [49] K. T. Lee, J. Cho, *Nano Today* **2011**, 6, 28.
- [50] R. Darling, J. J. Newman, *Electrochem. Soc.* **1997**, 144, 4201.

**Chapter 4. γ -Fe₂O₃/Graphene Nanocomposite for Lithium-Ion
Battery Anodes**

4.1. Introduction

Rechargeable Li-ion batteries (LIBs) are the most preferred power source in mobile communication and portable electronic devices owing to the outstanding energy and power density of LIBs. However, the current supply of LIBs is not sufficient to meet the huge demand for advanced long-lifespan batteries. Many critical issues such as the high energy density, high durability, low cost, and light weight of LIBs have been widely discussed [1-3]. Nanostructured materials including nanoparticles, nanofibers, nanotubes, and their composites have been extensively investigated to develop electrode materials with high energy density and improved cycling stability for LIBs [4-8].

Metal oxide nanoparticles are promising candidates for such electrode materials owing to their high theoretical capacity ($\sim 1000 \text{ mAh g}^{-1}$) than commercial graphite anodes (372 mAh g^{-1}) [9-11]. However, the poor electrical conductivity and severe volume change are critical barriers to their applications in commercial Li-ion batteries. The mechanisms of transition-metal-oxide anodes during charging/discharging in LIBs have been explained by conversion reactions [12]. The repeated charge/discharge reactions between the metal oxides and Li ions result

in large variation in volume, which is a major reason for the poor cycling performance of transition-metal-oxide materials [13-15].

Accordingly, many research groups have used metal-oxide/carbon composites as anode materials, which show enhanced cycling stability and electronic conductivity [16-23]. Graphene has recently attracted tremendous interest because of its high surface area (theoretical value: $2630 \text{ m}^2 \text{ g}^{-1}$), good electronic conductivity, mechanical stability, and so on [24,25]. These properties make graphene a very promising electrode material for various electrochemical applications [26,27]. As anode materials for LIBs, graphene-based composite materials exhibit an enhanced cycling stability with high capacity at low charge/discharge rates [28-32].

In the chapter 3, a direct method of synthesizing 2-dimensional metal-oxide/carbon nanocomposites for application as LIB anodes was introduced [33]. The prepared metal-oxide/carbon nanosheets exhibited good cycling stability and high capacity because of their short diffusion path and large accessible surface area for effective insertion of Li ions. Herein, a single-step method of preparing an iron-oxide/graphene nanocomposite and the application of this nanocomposite as anodes to enhance the performance of LIBs is introduced. This nanocomposite

material has the combined advantage of both metal oxides and graphene, exhibiting enhanced high-rate and cycling performance. The outstanding high-rate-performance of iron-oxide/graphene nanocomposite can mainly be attributed to the ability of graphene to maintain intimate close contact with iron oxide nanoparticles during the repeated charge/discharge reactions.

4.2. Experimental Section

4.2.1. Chemicals

Iron(III) acetylacetonate ($\text{Fe}(\text{acac})_3$) and oleic acid was purchased from Aldrich Chemical Co.

4.2.2. Characterization methods

Transmission electron microscopy (TEM) images were obtained using a JEOL EM-2100F microscope, and field-emission scanning electron microscopic (FE-SEM) images were obtained with a Hitachi S-4800 microscope. X-ray diffraction (XRD) analysis was carried out using a Rigaku Dmax 2500 diffractometer. The Brunauer-Emmett-Teller (BET) method was used to confirm the pore structure using a BELSORP-mini II (BEL JAPAN) nitrogen absorption analyzer. X-ray photoelectron energy spectra (XPS) was obtained using AXIS-His spectrometer.

4.2.3. Preparation of graphene

Graphene oxide (GO) was prepared from graphite powder (Aldrich, < 20 micron) by an improved Hummers method [34]. Graphene was obtained by a thermal expansion of the GO under high vacuum. The GO

was put into a two-neck round-bottom flask that was sealed at one end and the other end was connected to the high vacuum pump. The flask was rapidly heated under a high vacuum. At about 200 °C, a dramatic expansion of GO was observed. To remove the remaining functional groups completely, the power was kept at 300 °C for 5h.

4.2.4. Preparation of iron-oxide nanoparticles/graphene composite

In a typical synthesis, 2 mmol Fe(acac)₃ was mixed with 6 mmol oleic acid. These iron-oleate complexes were mixed with 0.2 g as-prepared graphene by using a pestle and mortar. The mixture was heated to 600 °C at the heating rate of 10 °C min⁻¹ under N₂ atmosphere and then kept at that temperature for 3 h.

4.2.5. Preparation of iron-oxide nanoparticles

In a typical synthesis, iron oxide nanoparticles were simply obtained through the heat treatment of as-prepared iron-oxide/graphene nanocomposite at 400 °C under air atmosphere for 6h.

4.2.6. Preparation of electrodes for LIBs

A working electrode was prepared by following scheme. A working

electrode was prepared by following scheme. A dry powder (active material), super P (carbon additive), and poly(vinylidene fluoride) (binder) (85:5:10) were mixed and coated on a piece of copper foil (current collector). In graphene electrode preparation, the ratio was changed to 70:0:30. After removing the residual moisture by drying in a vacuum oven at 120 °C for 12 h, the electrode plate was pressed to enhance the inter-particle contact and to reinforce adhesion between particles and the current collector. The electrochemical tests were performed by using a coin-type electrochemical cell (2032-type) which was fabricated with lithium foils as the counter and reference electrodes and 1.0 M LiPF₆ dissolved in a mixture of ethylene carbonate (EC) and dimethyl carbonate (DMC) (1:2 in vol. ratio) as the electrolyte. In order to cycle the coin-type electrochemical cells, they were discharged with constant current of 100 mA g⁻¹ to 0.05 V (vs. Li/Li⁺) and charged with constant current of 100 mA g⁻¹ to 3.0 V (vs. Li/Li⁺). In the rate capability test, the lithiation current density was fixed at 100 mA g⁻¹, but the delithiation current density was changed every five cycles according to this sequence of values: 100, 200, 500, 1000, 3000, 5000 and 100 mA g⁻¹.

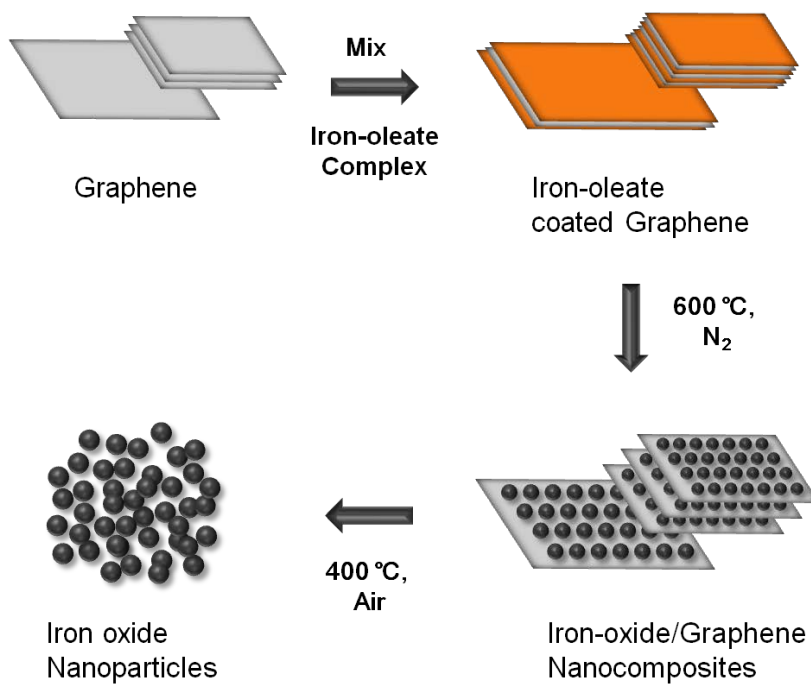


Figure 4.1. Schematic representation of the preparation of iron-oxide/graphene nanocomposites and iron oxide nanoparticles.

4.3. Results and Discussion

The schematics shown in Figure 4.1 illustrate the synthetic route for direct formation of iron-oxide/graphene nanocomposite. Graphene was prepared by thermal expansion of graphene oxide under high vacuum [35]. The specific surface area of graphene was $370 \text{ m}^2 \text{ g}^{-1}$, as determined by the Brunauer-Emmett-Teller (BET) method (Figure 4.2b). The total pore volume and average pore size of the graphene were $0.987 \text{ cm}^3 \text{ g}^{-1}$ and 10 nm. X-ray photoelectron spectroscopy (XPS) revealed that the as-prepared graphene had oxygen-containing functional groups on the graphene surface (Figure 4.2c). For preparing iron oxide nanoparticles, iron-oleate complex was used as the precursor [36]. Iron-oleate complex was homogeneously mixed with the graphene by simple grinding. The mixture was then heated at $\sim 600 \text{ }^\circ\text{C}$ under an inert atmosphere to form an iron-oxide/graphene nanocomposite. The iron-oleate complex was converted into monodisperse iron oxide nanoparticles on the surface of the graphene upon heating under the inert atmosphere. Field-emission scanning electron microscopy (FESEM) and transmission electron microscopy (TEM) were performed to characterize the surface morphology of the iron-oxide/graphene nanocomposite. As

shown in Figure 4.3a, the as-prepared graphene had a thin wrinkled paper-like structure. From Figure 4.3b and c, it is evident that iron oxide nanoparticles were well dispersed throughout the graphene layer (Figure 4.4). Both the iron oxide nanoparticles and graphene were in close contact with each other, and they acted as mutual spacers in the nanocomposite to prevent the aggregation of the nanoparticles and the restacking of the graphene layers. The typical size of the iron oxide nanoparticle was ~30 nm, as determined from the TEM image shown in Figure 4.3c. Further, the nanoparticles were found to be highly crystalline, as seen from the inset in Figure 4.3c, with a *d*-spacing of 0.295 nm. The observed *d*-spacing was consistent with the *d*-spacing of the (220) plane of maghemite ($\gamma\text{-Fe}_2\text{O}_3$). The crystal structure of the iron oxide nanoparticles in the nanocomposite was further characterized by powder X-ray diffraction (XRD) (Figure 4.2a). The carbon contents of the iron-oxide/graphene was 68.1 wt% which was measured by TGA analysis (Fig. 4.5).

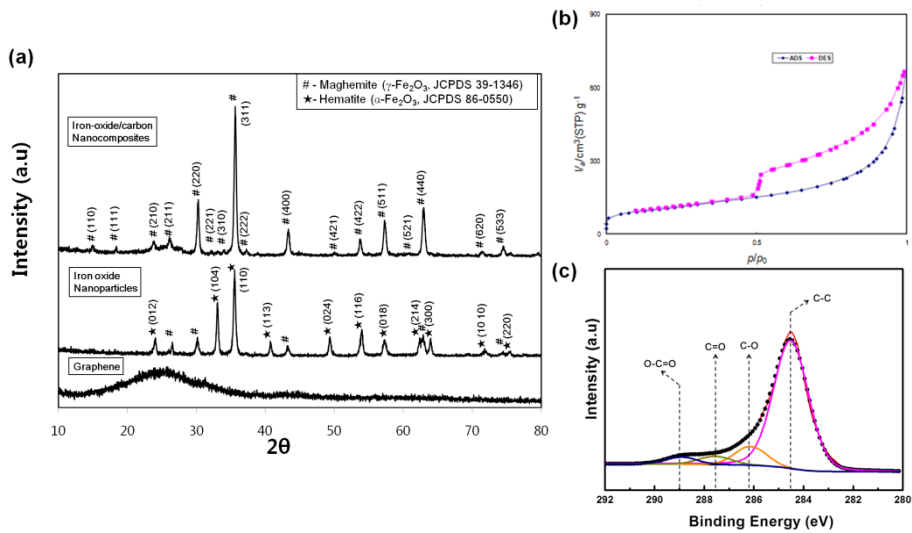


Figure 4.2. (a) XRD patterns of iron-oxide/graphene nanocomposite, iron oxide nanoparticle and graphene. (b) N_2 isotherms at 77 K and (c) XPS spectra of as-prepared graphene.

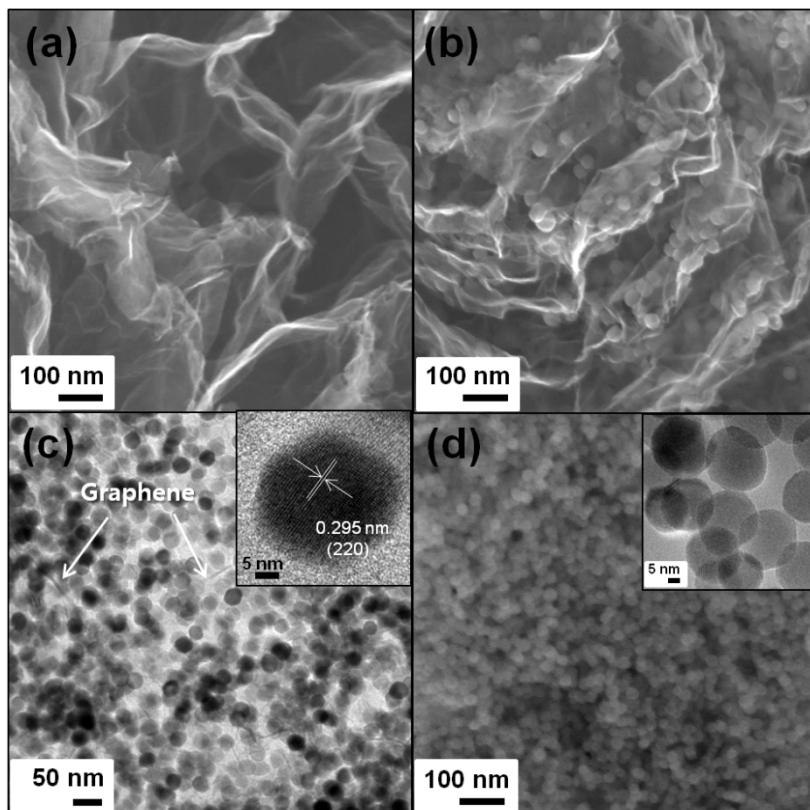


Figure 4.3. (a) FESEM image of as-prepared graphene, (b) FESEM image and (c) TEM image of iron-oxide/graphene nanocomposite and (d) SEM image of iron oxide nanoparticle. The inset figure represents high resolution TEM image of iron oxide nanoparticle.

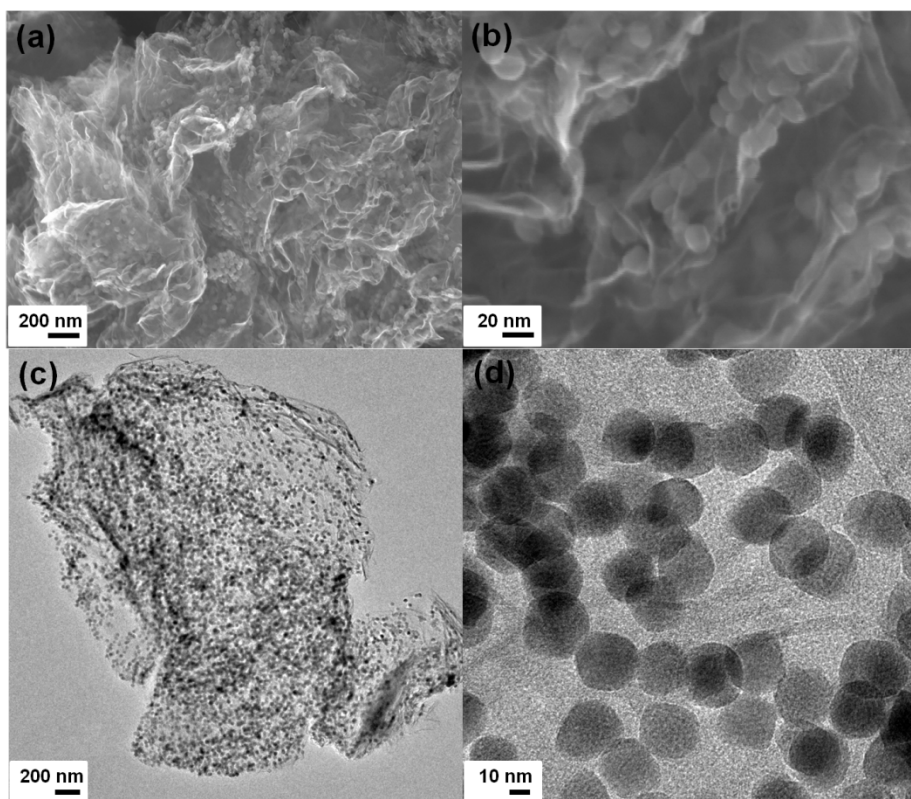


Figure 4.4. (a) Low and (b) high magnification FESEM image and (c) Low and (d) high magnification TEM image of iron-oxide/graphene nanocomposite.

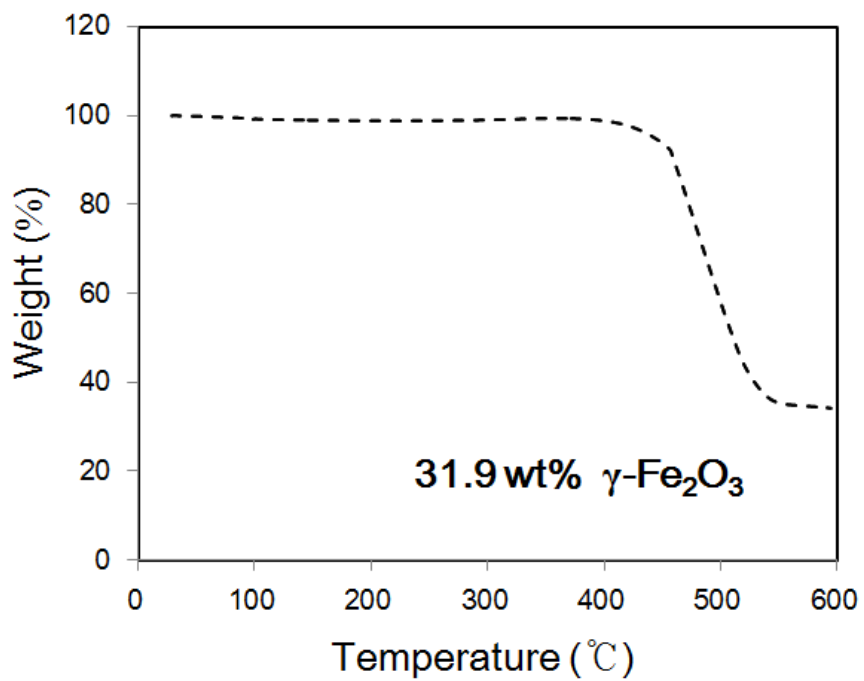


Figure 4.5. TGA result of iron-oxide/graphene nanocomposite.

Three different samples were produced out of the iron-oxide/graphene nanocomposite particles, iron oxide nanoparticles, and graphene sheets (hereafter referred to as iron-oxide/graphene, iron oxide, and graphene electrodes, respectively). The electrochemical performance of the electrodes was examined in a coin-type cell assembly. The galvanostatic charge/discharge voltage profiles were obtained at a current density of 100 mA g^{-1} (Figure 4.6a-c). During the initial cycles, the voltage profiles for the three electrodes showed little difference. The iron oxide electrode was lithiated in the range 0.5–1.0 V and was delithiated in the range 1.5–2.0 V. The charge/discharge voltage profiles obtained for the iron oxide electrode are consistent with those reported for the electrochemical conversion reaction $\text{Fe}_2\text{O}_3 + 6\text{Li}^+ + 6\text{e}^- \leftrightarrow 2\text{Fe} + 3\text{Li}_2\text{O}$ (theoretical capacity = 1007 mAh g^{-1}) [37,38]. However, the lithiation capacity (1538 mAh g^{-1}) of the electrode was larger than the theoretical capacity, probably due to irreversible electrolyte decomposition [39]. The graphene electrode is lithiated/delithiated over wide voltage ranges as a sloping voltage. The discharge (lithiation) voltage profile, however, shows some plateaus which are not distinguishable clearly, consistent with the data reported in literature [40]. In this voltage range, lithium ions are deposited as multi-layer on graphene surface at lithiation. The

high initial irreversible capacity of 74% may be due to the formation of a solid electrolyte interphase on the electrode surface and the reaction between Li ions and the oxygen-containing functional groups on the graphene surface [41]. The voltage profile for iron-oxide/graphene electrode appears to be a superimposition of the profiles for iron oxide and graphene electrodes. The plateaus in the range 0.5–1.0 V measured during lithiation and in the range 1.5–2.0 V measured during delithiation were exhibited as well as a sloping voltage in the wide region. And delithiation capacity of the nanocomposite was 982 mAh g⁻¹. This is similar to calculated value according to the iron-oxide and graphene contents. The initial coulombic efficiency enhancement of graphene nanocomposite can be explained by the heat treatment of high temperature (600 °C) in the synthesis process because some impurity on the graphene surface such as hydroxyl group could be removed.

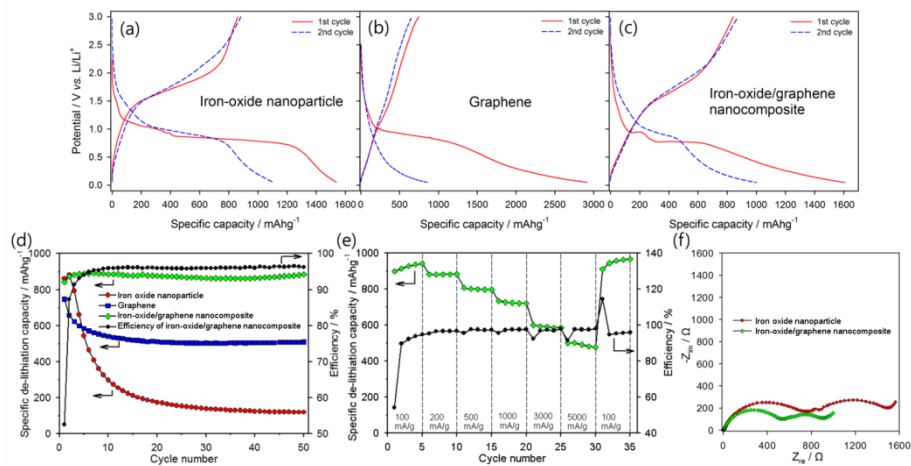


Figure 4.6. Galvanostatic discharge (lithiation, downward) and charge (delithiation, upward) voltage profiles of (a) iron oxide nanoparticle, (b) graphene and (c) iron-oxide/graphene nanocomposite. (d) Lithiation/delithiation capacities according to the cycle number of iron-oxide/graphene nanocomposite, iron oxide nanoparticle and graphene; Efficiency of iron-oxide/graphene nanocomposite. (e) Rate performance and efficiency of iron-oxide/graphene nanocomposite. (f) AC impedance spectra (Nyquist plot) obtained with the iron oxide nanoparticle and iron-oxide/graphene nanocomposite at fully lithiation state.

The cycle performances of the three electrodes measured at a current density of 100 mA g^{-1} are compared in Figure 4.6d. The capacity of the iron-oxide/graphene electrode stabilized rapidly, while those of the iron oxide and graphene electrodes deteriorated within the first few cycles. During the first 10 cycles, the delithiation capacity of graphene electrode decreased slightly from 750 to $\sim 500 \text{ mAh g}^{-1}$. This initial capacity deterioration of the graphene electrode seems to result from lithium trapping by the continuous irreversible reaction of graphene. In contrast, the iron oxide electrode exhibited rapid capacity deterioration within only a few cycles, which seems to result from the considerable change in the volume of the metal oxide due to the electrochemical conversion reactions. Repeated large volume changes lead to the pulverization of the nanoparticles and causes interparticle contact loss [42]. The iron-oxide/graphene electrode, however, does not seem to exhibit such deterioration in cycle performance. The delithiation capacity of the iron-oxide/graphene electrode remained constant at $\sim 900 \text{ mAh g}^{-1}$ for up to 50 cycles without any capacity losses. The efficiency of that is more than 95% during the cycles except first few cycles. The excellent cycle performance can be attributed to the structure of the iron-oxide/graphene nanocomposite: in the iron-oxide/graphene electrode, uniform-sized iron

oxide nanoparticles are well dispersed in graphene and the nanoparticles and graphene are in close contact. With this structure, the surrounding graphene can accommodate the volume expansion of the embedded iron oxide nanoparticles and still maintain a close contact with them. Moreover, the uniform nano size of the iron oxide particles can prevent interparticle aggregation because their volume can uniformly expand or contract as small range during cycling [43].

The iron-oxide/graphene electrode was tested at various current densities from 100 to 5000 mA g⁻¹, and the results are plotted in Figure 4.6e. The electrode exhibited an excellent high-rate capability. At the high current densities of 1000, 3000, and 5000 mA g⁻¹, the electrode exhibited high reversible capacities of almost 730, 600, and 500 mAh g⁻¹, respectively. These values are significantly higher than that of previous reported iron-oxide/graphene composite electrodes [44-47]. The excellent high-rate capability is ascribed to the favorable high conductance of graphene and the shorter diffusion length for the Li ions insertion/deinsertion into the iron oxide particles which is attributed to uniform-nano-sized particles. To investigate the influence of graphene on conductivity, AC impedance measurement was employed on two electrodes (iron oxide nanoparticle and iron-oxide/graphene

nanocomposite) as shown in Fig. 4.6f. In this figure, two distinct semicircles are recognized in each sample. The semicircle at the higher frequency region is associated with the SEI resistance, whereas the one at the lower frequency region is the charge transfer resistance. The total resistance of nanocomposite electrode is smaller than that of iron oxide nanoparticle electrode. This resistance decrease is ascribed to conductivity improvement by graphene and that seems to be the key factor of rate capability enhancement on nanocomposite electrode.

The structural deformation of the iron-oxide/graphene electrode during electrochemical cycling at a rate of 100 mA g^{-1} was investigated using TEM by observing the surface morphology of the electrode after the 50th charge/discharge cycle (Figure 4.7). The TEM image in Figure 4.7a shows that the overall surface morphology was retained and that severe deformation had not occurred during cycling. Although the iron oxide nanoparticles were pulverized into several smaller particles ($<5 \text{ nm}$) because of the close contact between the pulverized nanoparticles and the graphene was still maintained and the pulverized particles did not aggregate, both of which are clearly shown in the high-magnification TEM image (Figure 4.7b). Graphene seems to help maintain the initial structure of the iron-oxide/graphene nanocomposite and the close contact between the pulverized iron oxide particles and graphene.

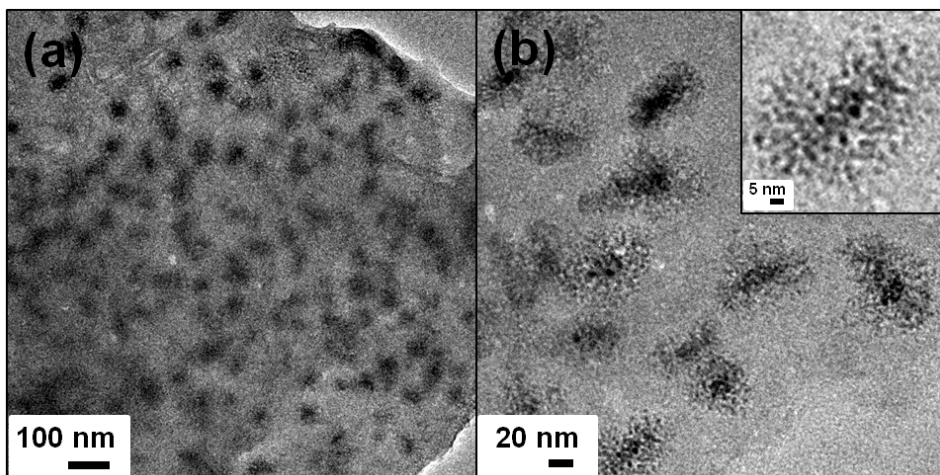


Figure 4.7. TEM images of iron-oxide/graphene nanocomposite after 50th charge/discharge cycling at a rate of 100 mA g^{-1} . The inset figure represents high resolution TEM image of the pulverized iron oxide nanoparticle.

4.4. Conclusion

In this chapter, iron-oxide/graphene nanocomposite was directly synthesized from an iron-oleate precursor and graphene. The electrochemical performance of the iron-oxide/graphene nanocomposite anode was excellent and was significantly better than those of the anodes prepared with only iron oxide nanoparticles or graphene. In particular, the nanocomposite electrode exhibited rapid initial stabilization and enhanced cycling stability and rate performance. Such outstanding electrochemical properties prove the huge potential for application of the nanocomposite as an anode material in LIBs. Furthermore, the method of synthesizing the nanocomposite can be easily extended to synthesizing nanocomposites of other metal oxides and graphene and producing advanced materials for use as anodes in LIBs.

4.5. References

- [1] G. Ceder, *MRS Bull.* **2010**, 35, 693.
- [2] K. Kang, Y. S. Meng, J. Bréger, C. P. Grey, G. Ceder, *Science* **2006**, 311, 977.
- [3] M. Armand, J.-M. Tarascon, *Nature* **2008**, 451, 652.
- [4] P. G. Bruce, B. Scrosati, J.-M. Tarascon, *Angew. Chem. Int. Ed.* **2008**, 47, 2930.
- [5] S. Zeng, K. Tang, T. Li, Z. Liang, D. Wang, Y. Wang, Y. Qi, W. Zhou, *J. Phys. Chem. C* **2008**, 112, 4836.
- [6] M. V. Reddy, Ting Yu, Chorng-Haur Sow, Ze Xiang Shen, Chwee Teck Lim, G. V. Subba Rao, B. V. R. Chowdari, *Adv. Funct. Mater.* **2007**, 17, 2792.
- [7] P. L. Taberna, S. Mitra, P. Poizot, P. Simon, J. -M. Tarascon, *Nat. Mater.* **2006**, 5, 567.
- [8] X. W. Lou, D. Deng, J. Y. Lee, J. Feng, L. A. Archer, *Adv. Mater.* **2008**, 20, 258.
- [9] S. K. Behera, *J. Power Sources* **2011**, 196, 8669.
- [10] Z.-M. Cui, L.-Y. Jiang, W.-G. Song, Y.-G. Guo, *Chem. Mater.* **2009**, 21, 1162.
- [11] X.-L. Wu, Y.-G. Guo, L.-J. Wan, C.-W. Hu, *J. Phys. Chem. C* **2008**, 112,

16824.

- [12] P. Poizot, S. Laruelle, S. Grugeon, L. Dupont, J.-M. Tarascon, *Nature* **2000**, 407, 496.
- [13] M. G. Kim, J. Cho, *Adv. Funct. Mater.* **2009**, 19, 1497.
- [14] J. Cabana, L. Monconduit, D. Larcher, M. R. Palacín, *Adv. Mater.* **2010**, 22, E170.
- [15] A. S. Arico, P. Bruce, B. Scrosati, J. M. Tarascon, W. Van Schalkwijk, *Nat. Mater.* **2005**, 4, 366.
- [16] L. J. Fu, H. Liu, H. P. Zhang, C. Li, T. Zhang, Y. P. Wu, R. Holze, H. Q. Wu, *Electrochem. Commun.* **2006**, 8, 1.
- [17] G. Cui, Y.-S. Hu, L. Zhi, D. Wu, I. Lieberwirth, J. Maier, K. Müllen, *Small* **2007**, 3, 2066.
- [18] Y.-S. Hu, R. Demir-Cakan, M.-M. Titirici, J.-O. Müller, R. Schlögl, M. Antonietti, J. Maier, *Angew. Chem. Int. Ed.* **2008**, 47, 1645.
- [19] C. Lei, F. Han, D. Li, W.-C. Li, Q. Sun, X.-Q. Zhang, A.-H. Lu, *Nanoscale* **2009**, 21, 2710.
- [20] H. Kim, J. Cho, *Nano Lett.* **2008**, 8, 3688.
- [21] X. W. Lou, C. M. Li, L. A. Archer, *Adv. Mater.* **2009**, 21, 2536.
- [22] Y. Piao, H. S. Kim, Y.-E. Sung, T. Hyeon, *Chem. Commun.* **2010**, 46, 118.
- [23] C. Ban, Z. Wu, D. T. Gillaspie, L. Chen, Y. Yan, J. L. Blackburn, A. C.

- Dillon, *Adv. Mater.* **2010**, 22, E145.
- [24] A. K. Geim, *Science* **2009**, 324, 1530.
- [25] S. Stankovich, D. A. Dikin, G. H. B. Dommett, K. M. Kohlhaas, E. J. Zimney, E. A. Stach, R. D. Piner, S. T. Nguyen, R. S. Ruoff, *Nature* **2006**, 442, 282.
- [26] C. N. R. Rao, A. K. Sood, K. S. Subrahmanyam, A. Govindaraj, *Angew. Chem. Int. Ed.* **2009**, 48, 7752.
- [27] J. R. Miller, R. A. Outlaw, B. C. Holloway, *Science* **2010**, 329, 1637.
- [28] P. Lian, X. Zhu, S. Liang, Z. Li, W. Yang, H. Wang, *Electrochim. Acta* **2010**, 55, 3909.
- [29] M. A. Worsley, P. J. Pauzauskie, T. Y. Olson, J. Biener, J. H. Satcher, T. F. Baumann, *J. Am. Chem. Soc.* **2010**, 132, 14067.
- [30] W. Chen, S. Li, C. Chen, L. Yan, *Adv. Mater.* **2011**, 23, 5679.
- [31] X. Zhu, Y. Zhu, S. Murali, M. D. Stoller, R. S. Ruoff, *ACS Nano* **2011**, 5, 3333.
- [32] Z. Zhu, T. Zhu, X. Zhou, Y. Zhang, X. W. Lou, X. Chen, H. Zhang, H. H. Hng, Q. Yan, *Nanoscale* **2011**, 3, 1084.
- [33] B. Jang, M. Park, O. B. Chae, S. Park, Y. Kim, S. M. Oh, Y. Piao, T. Hyeon, *J. Am. Chem. Soc.* **2012**, 134, 15010.
- [34] D. C. Marcano, D. V. Kosynkin, J. M. Berlin, A. Sinitskii, Z. Sun, A.

- Slesarev, L. B. Alemany, W. Lu, J. M. Tour, *ACS Nano* **2010**, 4, 4806.
- [35] W. Lv, D.-M. Tang, Y.-B. He, C.-H. You, Z.-Q. Shi, X.-C. Chen, C.-M. Chen, P.-X. Hou, C. Liu, Q.-H. Yang, *ACS Nano* **2009**, 3, 3730.
- [36] J. Park, K. An, Y. Hwang, J.-G. Park, H.-J. Noh, J.-Y. Kim, J.-H. Park, N.-M. Hwang, T. Hyeon, *Nat. Mater.* **2004**, 3, 891.
- [37] Larcher, C. Masquelier, D. Bonnin, Y. Chabre, V. Masson, J.-B. Leriche, J.-M. Tarascon, *J. Electrochem. Soc.* **2003**, 150, A133.
- [38] J. Morales, L. Sánchez, F. Martín, F. Berry, X. Ren, *J. Electrochem. Soc.* **2005**, 152, A1748.
- [39] R. Fong, U. von Sacken, J. R. Dahn, *J. Electrochem. Soc.* **1990**, 137, 2009.
- [40] P. Lian, X. Zhu, S. Liang, Z. Li, W. Yang, H. Wang, *Electrochim. Acta* **2010**, 55, 3909.
- [41] P. Guo, H. Song, X. Chen, *Electrochem. Commun.* **2009**, 11, 1320.
- [42] O. B. Chae, S. Park, J. H. Ku, J. H. Ryu, S. M. Oh, *Electrochim. Acta* **2010**, 55, 2894.
- [43] C. Kim, M. Noh, M. Shoi, J. Cho, B. Park, *Chem. Mater.* **2005**, 17, 3297.
- [44] M. Zhang, B. Qu, D. Lei, Y. Chen, X. Yu, L. Chen, Q. Li, Y. Wang, T. Wang, *J. Mater. Chem.* **2012**, 22, 3868.
- [45] X.-Y. Xue, C.-H. Ma, C.-X. Cui, L.-L. Xing, *Solid State Sci.* **2011**, 13, 1526.

- [46] G. Wang, T. Liu, Y. Luo, Y. Zhao, Z. Ren, J. Bai, H. Wang, *J. Alloys Compd.* **2011**, 509, L216.
- [47] L. Tian, Q. Zhuang, J. Li, C. Wu, Y. Shi, S. Sun, *Electrochim. Acta* **2012**, 65, 153.

Chapter 5. Conclusion and Future works

5.1. Conclusion

Nowadays, it is essential to develop new electrode materials with a high charge/discharge rate and a high reversible capacity to meet the increasing demand for higher energy density batteries. Nano-sized metal or metal oxides particles such as Sn, SnO₂, Si, MnO₂, Co₃O₄, MoO₃, and Fe₂O₃ are very promising electrode materials due to their significantly larger reversible capacity than that of commercial graphite. Their nanostructures could improve the reversible capacity and rate capacity, which can be attributed to shortened Li ion insertion/extraction pathways. However, transition metal oxides typically break into small metal clusters because they react with Li to form Li_xM_y alloy or M⁰, leading to a large volume expansion and a destruction of the structure upon electrochemical cycling, especially at high rates, thus resulting in severe loss of capacity with cycling and a poor electrical conductivity. Consequentially, the metal or metal oxide nanoparticle should be used with carbonaceous materials such as graphene, CNT, and porous carbon as anode for LIBs to improve the electrical conductivity and prevent the degradation from the volume exchange during the charge/discharge cycling.

In this thesis, various designed synthetic methods of carbon-based nanomaterials have been investigated for using as LIBs anode. Initially, using various synthetic methods, different kinds of carbon-based

materials have been obtained from the organic precursors such as surfactants and fatty acid. Monodispersed silica nanoparticles were used as templates and various metallic surfactants were used as carbon sources. Different shaped carbonaceous nanomaterials including hollow carbon nanostructures and 3-dimensional ordered mesoporous structures were obtained through the carbonization of metallic surfactant precursors. Next, two dimensional (2-D) nanomaterials composed of highly monodisperse metal oxide nanoparticles and carbon were synthesized via simple heat treatment process using salt powder as template. The iron oleate complex was prepared by “Heating-up” method. 2-D nanostructure of the nanocomposite was created by using sodium sulfate salt powder as template. Finally, the iron-oxide/graphene nanocomposite was directly obtained by heat treatment of a mixture of iron-oleate and graphene. The experimental results showed that uniform sized γ -Fe₂O₃ nanoparticles were homogeneously embedded in the graphene layers, and they acted as mutual spacers in the nanocomposite to prevent the restacking of the graphene layers and the nanoparticle’s aggregation.

These carbon-based nanocomposites were shown to be excellent anode materials for Li-ion batteries with high capacity, good rate performance and stable durability.

5.2. Future works

The use of high capacity materials including nano-sized metal or metal oxides particles such as Sn, SnO₂, Si, MnO₂, Co₃O₄, MoO₃, and Fe₂O₃ as LIBs anode, stability of solid electrolyte interface (SEI) layer at the interface between the active materials and the electrolyte is another critical factor in achieving a long cycle life. As shown in Figure 5.1, the SEI layer is formed on the electrode surface by electrolyte decomposition due to the low potential of the anode during battery charging. This SEI layer is a lithium-ion conductor, but an electronic insulator. The solid electrode nanoparticles expand out towards the electrolyte during the lithiation, then the SEI layer is formed on the surface of expanded electrode nanoparticles. The SEI on the lithiated expanded electrode nanoparticles is broken as the nanostructure shrinks during delithiation. The SEI layer is formed again on the fresh electrode surface to the electrolyte during the re-lithiation. Consequently, the SEI layer is becoming thicker by repeated charge/discharge cycles. This thicker SEI layer results in a degradation in LIBs performance. The longer lithium diffusion pathway through the thick SEI layer and the thicker electrically insulating layer acts as resistance in battery system. The formation of a stable SEI layer is critical factor for a long cycle life in large volume change anodes [1-7].

Considering a stable SEI layer is essential to develop new electrode materials with higher energy density and improved cycling stability for

LIBs. As further study, designed nanostructured anode materials such as mesoporous, hollow, and anisotropic nanostructures should be investigated for generating an effective and stable SEI layer.

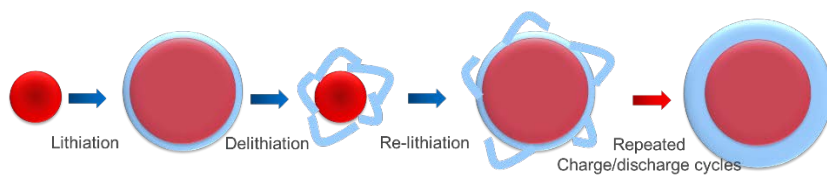


Figure 5.1. Schematic image of SEI formation on the surface of high capacity materials including nano-sized metal or metal oxides particles.

5.3. References

- [1] L. Y. Beaulieu, K. W. Eberman, R. L. Turner, L. J. Krause, J. R. Dahn, *Electrochem. Solid State Lett.* **2001**, 4, A137.
- [2] T. D. Hatchard, J. R. Dahn, *J. Electrochem. Soc.* **2004**, 151, A838.
- [3] L. Y. Beaulieu, T. D. Hatchard, A. Bonakdarpour, M. D. Fleischauer, J. R. Dahn, *J. Electrochem. Soc.* **2003**, 150, A1457.
- [4] T. Song, J. Xia, J.-H. Lee, D. H. Lee, M.-S. Kwon, J.-M. Choi, J. Wu, S. K. Doo, H. Chang, W. I. Park, D. S. Zang, H. Kim, Y. Huang, K.-C. Hwang, J.A. Rogers, U. Paik, *Nano Lett.* **2010**, 10, 1710.
- [5] D. Aurbach, *J. Power Sources* **2000**, 89, 206.
- [6] P. Verma, P. Maire, P. Novak, *Electrochem. Acta* **2010**, 55, 6332.
- [7] H. Wu¹, G. Chan, J. W. Choi, I. Ryu, Y. Yao, M. T. McDowell, S. W. Lee, A. Jackson, Y. Yang, L. Hu, Y. Cui, *Nat. Nanotechnol.* **2012**, 7, 310.

Bibliography

1. International Publications

- 1) **Byungchul Jang**, Mihyun Park, Oh B. Chae, Sangjin Park, Youngjin Kim, Seung M. Oh, Yuanzhe Piao, Taeghwan Hyeon, “Direct Synthesis of Self-Assembled Ferrite/Carbon Hybrid Nanosheets for High Performance Lithium-Ion Battery Anodes”, *Journal of American Chemical Society*, **2012**, *134*, 15010-15015.

- 2) **Byungchul Jang**, Kyungmo Yang, Bo Quan, Yuanzhe Piao, “Simple synthesis of thin-layered hollow carbon nanostructures by the direct pyrolysis of surfactants”, *Materials Letters*, **2013**, *104*, 68-71.

- 3) **Byungchul Jang**, Eunjin Choi, Yuanzhe Piao,
“Preparation of well-dispersed Pt nanoparticles on solvothermal
graphene and their enhanced electrochemical properties”,
Materials Research Bulletin, **2013**, 48, 834-839.
- 4) **Byungchul Jang**, Oh B Chae, Seung-Keun Park, Jeonghyun Ha,
Seung Mo Oh, Hyon Bin Na, Yuanzhe Piao,
“Solventless synthesis of iron-oxide/graphene nanocomposite and
its application as anode in high-rate Li-ion batteries”,
Journal of Materials Chemistry A, **2013**, 1, 15442-15446.
- 5) **Byungchul Jang**, Sungyool Bong, Seunghee Woo, Seung-Keun
Park, Jeonghyun Ha, Eunjin Choi, Yuanzhe Piao,
“Facile Synthesis of One-dimensional Iron-oxide/Carbon Hybrid
Nanostructures as Electrocatalysts for Oxygen Reduction Reaction
in Alkaline Media”,
Journal of Nanoscience and Nanotechnology, **2014**, Accepted.
- 6) Seung-Keun Park, Seung-Ho Yu, Nicola Pinna, Seunghee Woo,
Byungchul Jang, Young-Hoon Chung, Yong-Hun Cho, Yung-Eun

Sung, Yuanzhe Piao,

“A facile hydrazine-assisted hydrothermal method for the deposition of monodisperse SnO₂ nanoparticles onto graphene for lithium ion batteries”,

Journal of Materials Chemistry, **2012**, 22, 2520-2525.

7) Eunjin Choi, Minjeong Kwak, **Byungchul Jang**, Yuanzhe Piao,

“Highly Monodisperse Rattle-Structured Nanomaterials with Gold Nanorod Core/Mesoporous Silica Shell as Drug Delivery Vehicles and Nanoreactors”,

Nanoscale, **2013**, 5, 151-154.

8) Sungyool Bong, **Byungchul Jang**, Seunghee Woo, Yuanzhe Piao,

"Enhanced Electrocatalytic Activity of Solvothermal Graphene Supported PtRu Catalyst toward Methanol Oxidation",

International Journal of Electrochemical Science, **2013**, 8, 7510-7517.

9) Jeonghyun Ha, Seung-Keun Park, Seung-Ho Yu, Aihua Jin,

Byungchul Jang, Sungyool Bong, In Kim, Yung-Eun Sung,

Yuanzhe Piao,

“Chemically activated graphene-encapsulated LiFePO₄ composite for high-performance lithium ion batteries”,

Nanoscale, **2013**, 5, 8647-8655.

10) Seung-Keun Park, Aihua Jin, Seung-Ho Yu, Jeonghyun Ha, **Byungchul Jang**, Sungyool Bong, Seunghee Woo, Yung-Eun Sung, Yuanzhe Piao,

“In Situ Hydrothermal Synthesis of Mn₃O₄ Nanoparticles on Nitrogen-doped Graphene as High-Performance Anode materials for Lithium Ion Batteries”,

Electrochimica Acta, **2014**, 120, 452-459.

11) Sangjin Han, **Byungchul Jang**, Taeahn Kim, Seung M. Oh, Taeghwan Hyeon,

“Simple Synthesis of Hollow Tin Dioxide Microspheres and Their Application to Lithium-Ion Battery Anodes”,

Advanced Functional Materials, **2005**, 15, 1845-1850.

12) Sangjin Han, Sang-Hyun Choi, Seok-Soon Kim, Min Cho,

Byungchul Jang, Dong-Yu Kim, Jeyong Yoon, Taeghwan Hyeon,
“Low-Temperature Synthesis of Highly Crystalline TiO₂
Nanocrystals and their Application to Photocatalysis”,
Small, **2005**, 1, 812-816.

2. International Conferences

1) **Byungchul Jang**, Seung-Keun Park, Jeonghyun Ha, Yuanzhe Piao,
“Solventless synthesis of iron-oxide/graphene nanocomposite as
anode materials in Li-ion secondary batteries”,
225th ECS Meeting, Orlando, FL, USA, May 11-15, 2014.

2) **Byungchul Jang**, Yuanzhe Piao,
“Simple synthesis of 2-dimensional iron-oxide/carbon
nanocomposites as Li-ion secondary battery anodes”
Research Society 2013 Spring Meeting, MRS, San Francisco, San
Francisco, CA, USA, April 1-5, 2013.

3) **Byungchul Jang**, Yuanzhe Piao,

“Silica Based Nanoparticle Systems for Multifunctional Biomedical Applications”

International Conference on Nanoscience & Technology, China
2011, Beijing, September 7-9, 2011.

4) Kyungmo Yang, **Byungchul Jang**, Yuanzhe Piao,

“Synthesis of Water dispersible Iron oxide using a ligand exchange method”

The 9th International Nanotech Symposium & Nano-Convergence Expo, Conference on Pioneering Convergence Technologies, NANO KOREA 2011, Kintex, Koera, August 24-26, 2011.

5) **Byungchul Jang**, Sungyool Bong, Yuanzhe Piao,

“Facile Synthesis of One-dimensional Iron-oxide/Carbon Hybrid Nanostructures as Electrocatalysts for the Oxygen Reduction Reaction in Alkaline Media”,

NANO KOREA 2013, COEX, Seoul, Korea, July 10-12, 2013.

6) Sungyool Bong, **Byungchul Jang**, Seunghee Woo, Yuanzhe Piao,

“Improved Electrocatalytic Activity of PtRu/solvothermal

Graphene Electrocatalyst for Methanol Oxidation”,

NANO KOREA 2013, COEX, Seoul, Korea, July 10-12, 2013.

- 7) **Byungchul Jang**, Seung-Keun Park, Jeonghyun Ha, Yuanzhe Piao,
“Simple synthesis of iron-oxide/graphene nanocomposite and its
application as anode in Li-ion batteries”,
SNU-HU 2013 International Workshop on New Frontiers in
Convergence Science and Technology, GSCST, Suwon, Korea,
December 13, 2013.

3. Domestic Conferences

- 1) **Byungchul Jang**, Eunjin Choi, Yuanzhe Piao,
“Synthesis of Pt/Graphene composite materials via solvothermal and polyol process”
The 1st Conference on Pioneering Convergence Technologies,
RAMADA Hotel, Jeju, Koera, February 14-16, 2011.

- 2) **Byungchul Jang**, Yuanzhe Piao,
“Synthesis of high loading Pt/solvothermal graphene using a seed mediated growth process”,
2011 The Korean Chemical Society Spring Meeting (107th National Meeting), ICC, Jeju, Koera, April 28-29, 2011.

- 3) **Byungchul Jang**, Yuanzhe Piao,
“Synthesis of Thin Layered Carbon Nanomaterials Using Surfactants via Salt Template method”,
The 2nd Conference on Pioneering Convergence Technologies,
Hanwha resort, Busan, Koera, February 4, 2012.

- 4) **Byungchul Jang**, Yuanzhe Piao,
“Simple synthesis of 2-dimensional iron-oxide/carbon
nanocomposites as Li-ion secondary battery anodes”,
The 3rd Conference on Pioneering Convergence Technologies,
AICT, Suwon, Koera, January 25, 2013.
- 5) **Byungchul Jang**, Kyungmo Yang, Bo Quan, Yuanzhe Piao,
“Synthesis of Hollow Carbon Nanospheres by the direct pyrolysis of
Surfactants”,
2013 Spring meeting of Korean Carbon Society, SNU, Seoul, Korea,
May 9-10, 2013.
- 6) **Byungchul Jang**, Yuanzhe Piao,
“2-Dimensional Ferrite/Carbon Nanocomposites as Li-Ion
Secondary Battery Anodes”,
2013 The Korean Chemical Society Spring Meeting (111th National
Meeting), Kintex, Koera, April 17-19, 2013.
- 7) **Byungchul Jang**, Yuanzhe Piao,
“Iron oxide nanoparticles embedded carbon nanosheets as anode

materials in Li-ion secondary battery”,

2013 Fall meeting of The Korean Electrochemical Society, Daejeon, Korea, November 7-9, 2013.

8) **Byungchul Jang**, Yuanzhe Piao,

“Iron Oxide Nanoparticles Embedded Graphene Nanocomposite as Anode Material in Li-Ion Secondary Batteries”,

2014 Spring meeting of The Korean Society of Industrial and Engineering Chemistry, ICC, Jeju, Koera, April 30 - May 2, 2014.

4. Patents

- 1) 현택환, 박원철, **장병철**, 균일한 크기의 금속산화물 나노입자 및 금속산화물-탄소 나노복합체의 제조 방법, 출원번호: 10-2011-0074034.
- 2) 박원철, **장병철**, 봉성율, 나노 촉매 입자의 제조방법 및 나노 담지 복합촉매의 제조방법, 출원번호: 10-2013-0022770.

국 문 초 록

지난 반세기 동안 나노재료의 조성, 크기 등을 포함하는 구조 및 물성 제어에 관한 많은 연구가 진행되고 있다. 특히, 탄소재료는 우수한 전기화학적 특성과 안정성 때문에 에너지 저장 및 변환 장치에 적용이 가능하여 전극재료로 많은 연구가 진행되었다. 실제로 탄소재료는 연료전지용 촉매 담체, 이차전지용 전극재료, 슈퍼캐패시터용 전극재료 등으로 널리 사용 및 연구되고 있다. 또한 탄소재료는 나노기술을 접목함으로써 다양한 구조 제어가 가능하고 그에 따른 다양한 물성 제어가 가능하기 때문에 에너지 응용분야의 성능 및 효율향상이 기대가 된다.

일반적으로 탄소나노재료는 유기물 전구체를 고온에서 열처리하여 제조가 가능하며 다양한 합성법을 통해 구조 및 물성 제어가 가능하다. 특히, 전구체 종류와 제조 조건에 따라 물리화학적, 전기적 특성과 같은 다양한 탄소재료의 물성을 제어할 수 있다. 또한 주형합성법과 같은 합성법을 통해 다양한 형상, 구조 및 물성을 갖는 탄소나노재료의 합성 또한 가능하다.

최근에는 탄소나노재료를 기반으로 하여 그래핀, 금속, 금속산화물 등과 같은 재료를 복합화함으로써 탄소재료 본연의 특성을 향상시키려는 연구가 활발히 진행되고 있다.

본 학위 논문에서는 탄소나노재료를 기반으로 한 복합재료의 합성 및 리튬이차전지 전극재료의 응용에 대한 내용을 기술하고자 하였다. 구체적으로는, 계면활성제 및 지방산을 탄소 전구체로한 탄소 나노재료의 합성, 이차원 판상 구조를 갖는 금속산화물과 탄소 복합재료의 합성 및 리튬 이차전지 음극재료의 응용, 그래핀과 금속산화물의 복합화를 통한 그래핀/금속산화물 나노 복합재료 합성 및 리튬 이차 전지 음극재 응용에 관한 내용이다.

다양한 방법을 통해 탄소나노재료 및 복합재료의 구조 및 형상을 제어하여 리튬 이차전지 전극재료 적용하였을 때, 기존 소재 대비 월등한 성능 향상 및 내구성 향상을 확인할 수 있었다.

주요어: 탄소재료, 금속산화물 나노입자, 그래핀, 나노 복합재, 리튬이온 이차전지

학 번: 2010-31263